APPLICATIONS OF BOGOMOLNY'S SEMICLASSICAL QUANTIZATION TO INTEGRABLE AND NONINTEGRABLE SYSTEMS

MARIE HÉLÈNE JULIE LEFEBVRE, B.SC.

A Thesis

Submitted to the School of Graduate Studies

in Partial Fulfilment of the Requirements for the Degree

Doctor of Philosophy

McMaster University

August 1995

DOCTOR OF PHILOSOPHY (1995)
(THEORETICAL PHYSICS)

MCMASTER UNIVERSITY
Department of Physics and Astronomy
Hamilton, Ontario

TITLE: Applications of Bogomolny's Semiclassical Quantization to Integrable and Nonintegrable Systems

AUTHOR: Julie H. Lefebvre
B.Sc. (University of Waterloo)

ADVISOR: Professor David A. Goodings

PAGES: ix, 171

APPLICATIONS OF BOGOMOLNY'S SEMICLASSICAL QUANTIZATION

Acknowledgements

I have been very fortunate for the opportunity to work with David Goodings and Tom Szeredi. Their friendship, guidance and support, have meant a great deal to me. I would like to thank Rajat Bhaduri for many enjoyable discussions and for giving me the opportunity to develop my teaching skills. The above people have contributed to this work over the years with their suggestions and critical comments. I would like to thank Daniel Provost, Randy Dumont, Kaori Tanaka, Micheal Haggerty and Nina Snaith for their interest in my work and helpful comments. Thanks are extended to Peter Sutherland for generously giving me an account on snowdrop, where the majority of these computations were done. I am grateful to the Department of Physics and Astronomy at McMaster University and the Natural Sciences and Engineering Research Council of Canada for their finacial support. My colleagues, in the Department of Physics and Astronomy, have made it a pleasure to work at McMaster University. Jackie, a special thanks to you for always making me feel welcomed in your office and for making my days at work fun. Both of my families and friends have played a vital role in this achievement with their continuing encouragement and understanding. Mom and Arnold, with your constant support, and Marie, with your sense of humour, you have kept my spirits alive. Most of all, thank you Jeff for your love and for believing in me.

Contents

List of Figures

List of Tables

Abstract

Bogomolny's transfer operator (T-operator) method is used to calculate semi-classical energy eigenvalues and eigenfunctions for the quantum analogues of several Hamiltonian systems. The calculations are performed with a finite approximation to the T-operator in coordinate space. We demonstrate the success of this technique for the integrable systems, the circle and the 45° wedge billiards, as well as for nonintegrable systems, the 41° and 30° wedge billiards (both displaying mixed behaviour) and the 49° and 60° wedge billiards (both showing hard chaos). For the 49° wedge, an alternate partition involving the symbolic sequences is studied. We also focus on properties of the eigenvalues of the T-operator with the objective of finding a reliable characteristic to describe the manifestation of chaos in quantum systems. In particular, we discuss the special connection between the T-operator eigenvalues and quantum numbers of integrable system. In addition, we investigate the distributions of phase separations of the T-operator eigenvalues and show that they may reflect the dynamical properties of Hamiltonian systems.

Chapter 1

Introduction

The primary objective of semiclassical physics is to elucidate the correspondence between classical and quantum mechanics. One of the more recent challenges in this research area is to understand how chaos, a purely classical concept, manifests itself in quantum systems. A classical system can either be regular or chaotic depending on its dynamics, the behaviour of which is portrayed by trajectories in phase space. A Hamiltonian system is chaotic if two trajectories, initially close together in phase space, move apart at an exponential rate in any direction. This definition of chaos based on the exponential divergence of nearby trajectories does not apply to quantum systems: in quantum mechanics, the resolution of phase space is limited by Planck's constant h and consequently, trajectories are not well defined. Thus for quantum systems whose classical analogues are chaotic, one can ask if there are any characteristics that define *quantum chaos*.

The connections between classical and quantum mechanics are most often established by semiclassical quantization schemes. For regular (or integrable) Hamil-

tonian systems, the relationship between classical and quantum mechanics has been known since the development of quantum mechanics. If a Hamiltonian system with N freedoms is integrable, there exist N isolated constants of motion I_i (action variables). In this case, the motion of the system can be described by the N action variables $I_1, ..., I_N$ and N angle variables $\theta_1, ..., \theta_N$ [18]. The resulting trajectory is a curve on an N-torus in the $2N$-dimensional phase space. A very useful tool for studying the integrability of Hamiltonian systems is the Poincaré surface of section (PSS), a $(2N-2)$-dimensional submanifold of the phase space. In particular, for a two-dimensional Hamiltonian system, the PSS is a two-dimensional surface represented by coordinates in two-dimensional plane. A point is drawn on this plane whenever a trajectory crosses the PSS. If the system is integrable, a trajectory will create a series of points which lie on a one-dimensional curve.

In the "Old Quantum Theory", classical and quantum mechanics are related by the Bohr-Sommerfeld quantization condition which quantizes the action variables I_i according to the rule,

$$I_i = \int_{C_i} p\, dq = 2\pi\hbar n_i. \tag{1.1}$$

Here, C_i is a closed trajectory on the torus corresponding to the angle variable θ_i changing by 2π. The $n_i \geq 0$ are the quantum numbers which have integer values. Equation (1.1) can be used to quantize any integrable system. However, it is not possible, in general, to solve for the energy of the system in terms of the quantum

numbers n_i [16]. Over the years, this quantization condition developed into what is now referred to as Einstein-Brillouin-Keller (EBK) quantization:

$$I_i = \int_{C_i} p\, dq = 2\pi\hbar\,(n_i + \nu_i/4)\,, \tag{1.2}$$

where the integer $\nu_i \geq 0$ is called the Maslov index which counts the number of conjugate points (where the semiclassical approximation is not valid) for the trajectory.

For classically nonintegrable (or chaotic) systems, a comparable quantization scheme to that of Eq. (1.2) was not available until the early 1970s when Gutzwiller derived the trace formula [20]. Nonintegrable N-dimensional Hamiltonian systems have less than N isolated constants of motion I_i. Consequently, the motion of the system is no longer restricted to an N-dimensional torus and the EBK quantization scheme, based on action variables, no longer applies. On the two- dimensional PSS, certain trajectories, if not all, will appear as a scatter of points limited by the classically allowed region of motion. There are two types of chaotic systems: those which are composed of a mixture of dynamical behaviours, regular or chaotic, depending on the initial conditions, and those which are always chaotic. In the first case, the two-dimensional PSS displays both one-dimensional curves and scattered points. These systems display *mixed behaviour* or *soft chaos*. In the latter case, the entire PSS is filled with points and this condition is referred to as *hard chaos*.

Gutzwiller [20] showed that, in the semiclassical limit, the exact quantum density of states $d(E) = \sum_n \delta(E - E_n)$ could be approximated by two terms:

$$d(E) \approx d_{TF}(E) + d_{osc}(E), \tag{1.3}$$

where $d_{TF}(E)$ is the Thomas Fermi term, which provides a smooth approximation to the density of states, and $d_{osc}(E)$ is an oscillatory refinement to $d_{TF}(E)$. The oscillatory term $d_{osc}(E)$ is an infinite sum over all the periodic orbits of the classical system. More precisely,

$$d_{osc}(E) = \sum_{\gamma} \sum_{k=1}^{\infty} \frac{T_\gamma(E)}{\pi\hbar} \frac{\cos\left(k\frac{S_\gamma(E)}{\hbar} - k\frac{\nu_\gamma \pi}{2}\right)}{\left(e^{k\nu_\gamma} - \sigma_\gamma^k e^{-k\nu_\gamma \pi/2}\right)}, \tag{1.4}$$

where γ labels a primitive periodic orbit, k accounts for the multiple traversals of these primitive orbits, $S_\gamma(E) = \int \vec{p}(E)\, d\vec{q}$ is the action along the periodic orbit γ, $T_\gamma(E)$ is the period, $\sigma_\gamma^k = \pm 1$ if the orbit is hyperbolic or inverse hyperbolic, and ν_γ is the Maslov index. The sum over periodic orbits in Eq. (1.4) creates peaks in the density of states at (or near) the quantum energy eigenvalues E_n. Thus, the periodic orbits are the essence of Gutzwiller's semiclassical quantization for chaotic systems. However, the Gutzwiller trace formula and reformulations of it as the zeta product, are restricted to systems with isolated periodic orbits, and in most cases, this implies systems with hard chaos. In addition, the trace formula is an infinite sum which is at best conditionally convergent due to the exponential proliferation of periodic orbits in chaotic systems. Hence, there was a need for an efficient quantization method for generic Hamiltonian systems.

In 1992, Bogomolny developed the T-operator method [11] [10] which pro-

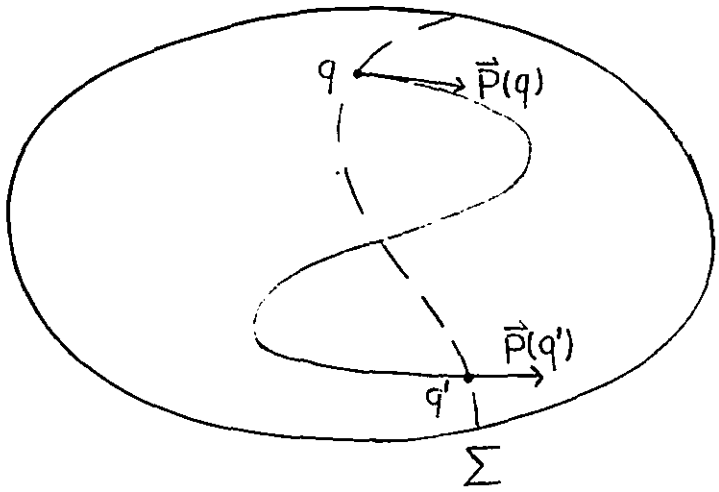

Figure 1.1: The transfer operator in coordinate space involves classical trajectories connecting the points q and q' such that the component of the momentum normal to the PSS (Σ) at these points is in the same direction.

vides a new quantization condition applicable to any N-dimensional bound Hamiltonian systems. Bogomolny's T-operator method reduces an N dimensional Schrödinger equation to an $(N-1)$-dimensional integral equation defined on a chosen Poincaré surface of section (PSS). The essence of the T-operator method is the transfer operator $T(E)$. For simplicity, consider a two-dimensional system whose boundary in configuration space delimits the classically accessible region (drawn in Fig. 1.1). Choose an arbitrary PSS in configuration space (Σ—represented by the dotted line in Fig. 1.1). The transfer operator $T(q, q'; E)$ is a semiclassical propagator which maps a point q' to a point q on the PSS. It is formally defined by the integral equation,

$$\psi(q) = \int_{\Sigma} T(q, q'; E)\psi(q')\, dq'. \tag{1.5}$$

where $\psi(q)$ is a wavefunction defined on the PSS. The transfer operator $T(q, q'; E)$ is constructed from properties of the classical trajectories connecting the points q and q' such that the component of the momentum normal to the PSS at these points is in the same direction. An example of such a trajectory is drawn in Fig. 1.1. The T-operator is given by the relation

$$T(q, q'; E) = \sum_{cl.tr.} \frac{1}{(2\pi i\hbar)^{1/2}} \left| \frac{\partial^2 S(q, q'; E)}{\partial q \partial q'} \right|^{\frac{1}{2}} \exp\left[iS(q, q'; E)/\hbar - i\nu\pi/2 \right]. \tag{1.6}$$

Here, $S(q, q'; E) = \int_{q'}^{q} \vec{p} d\vec{q}$ is the action at energy E for the classical trajectory connecting the points q and q' and crossing the PSS only once in between. The phase index ν is incremented for every point along the trajectory at which the semiclassical approximation is not valid. The reader is referred to Bogomolny's original paper [10] for details of the derivation of Eq. (1.6). The T-operator has properties similar to the time dependent Green's function: the most important ones being (i) the convolution of two T-operators given by

$$T(q, q'; E) = \int T(q, q''; E) T(q'', q'; E)\, dq'' \tag{1.7}$$

and (ii) the unitarity (i.e. $T^{\dagger}T = 1$) of the T-operator in the semiclassical limit.

The quantization condition is obtained in the process of solving for the wavefunctions $\psi(q)$ that satisfy the definition in Eq. (1.5). If one writes the wavefunctions $\psi(q)$ as a sum of functions constituting an orthogonal basis $\{\phi_a(q)\}$ defined on the

PSS,

$$\psi(q) = \sum_a c_a \phi_a(q), \tag{1.8}$$

and if one then substitutes this sum into Eq. (1.5), one obtains the relations

$$\sum_a c_a \left[\delta_{a,a'} - T_{a,a'}(E)\right] = 0, \tag{1.9}$$

where $T_{a,a'}(E) = \int \phi_a^*(q) T(q, q'; E) \phi_{a'}(q')\, dq\, dq'$. The homogeneous equations (1.9) have a nontrivial solution if and only if,

$$\det[\delta_{a,a'} - T_{a,a'}(E)] = 0. \tag{1.10}$$

Equation (1.10) is Bogomolny's semiclassical quantization condition. The semiclassical energy eigenvalues are the energies E_n which satisfy Eq. (1.10). For the T-matrix $T_{a,a'}(E)$ to be unitary, its dimensionality is given by the number of Planck cells of volume $(2\pi\hbar)^{N-1}$ that fit in the volume of the allowed region on the PSS. In this way, the uncertainty principle is incorporated into the formalism. The minimum dimension for the T-matrix required to obtain all of the semiclassical energy eigenvalues up to the energy E is,

$$N_p(E) = \frac{\text{volume of allowed region on the PSS}}{(2\pi\hbar)^{N-1}}. \tag{1.11}$$

The advantages of Bogomolny's T-operator method are that, compared to quantization schemes involving periodic orbits, it is easier to use for computing ap-

proximate energy eigenvalues, and it provides a new perspective on the connections between classical and quantum mechanics. The T-operator method only requires information about classical paths making one crossing with the PSS, and these, along with their properties, are much easier to find than periodic orbits. In addition, it is free of the convergence problems that trouble the Gutzwiller trace formula. The uncertainty principle is explicitly built into Bogomolny's quantization scheme unlike the Gutzwiller trace formula. The T-operator is also referred to as a semiclassical Poincaré mapping, analogous to the classical Poincaré map. In the same way that the PSS and the classical Poincaré map are invaluable tools in classical mechanics to describe the nature of Hamiltonian systems, the T-operator and its properties may illuminate the meaning of chaos in quantum systems.

Bogomolny's T-operator method is a generalization of the boundary integral method which is a technique for obtaining exact quantum solutions for two dimensional billiards by reducing the two dimensional Schrodinger equation to a one dimensional integral equation. In a similar way, Bogomolny's T-operator method reduces an N dimensional Schrödinger equation to an $(N-1)$-dimensional integral equation. However, it applies to any Hamiltonian system (i.e. it is not restricted to billiard systems). In addition, the integral equation in Bogomolny's technique is defined on any chosen PSS, whereas in the boundary integral method, the integral equation is restricted to the billiard boundary. Finally, the T-operator method involves a *semiclassical* propagator, the transfer operator (or T-operator), constructed

from classical trajectories. For this reason, the energy eigenvalues are semiclassical approximations to the exact quantum solutions. Hence, for force-free two-dimensional billiard systems in which the billiard boundary is chosen as the PSS, Bogomolny's T-operator method reduces to the boundary integral method. However, in this case, the T-operator involves only the first order approximation in $\hbar$ to the exact propagator.

At approximately the same time that Bogomolny's T-operator method appeared in print, Doron and Smilansky [15] published their work on the scattering approach to the quantization of billiards. Their method is closely related to Bogomolny's T-operator method since it involves constructing a propagator (S-matrix) along an arbitrary PSS, and the resulting quantization condition has the same form as Bogomolny's. However, the S-matrix is different from the T-operator since it consists of a product of two scattering matrices of two opened billiards (i.e. is based on scattering waves instead of classical paths). Also, the S-matrix is an exact quantum propagator (or an exact quantum Poincaré mapping) when it includes evanescent modes (genuinely quantum mechanical). Recently, Prosen [34] generalized the scattering approach to N-dimensional systems and arbitrary bound Hamiltonians (not restricted to billiards). He showed that the scattering matrix is equivalent to the T-operator in the semiclassical limit. An advantage of the scattering approach is its versatility. It can provide exact quantum or semiclassical solutions. However, Bogomolny's form explicitly shows the connection between classical and quantum mechanics since it is constructed entirely from information related to classical trajec-

tories, yet it only yields approximate quantum energy eigenvalues. Depending upon the nature of the system, one approach may offer a distinct advantage over the other.

The focus of this thesis is on applications of Bogomolny's T-operator method to integrable and nonintegrable Hamiltonian systems. Since the T-operator method is relatively new, there have only been a handful of studies exploring this technique. Shortly after the appearance of Bogomolny's epic paper [10], Lauritzen published a paper in which he presented a general form for the T-operator of integrable systems [28]. Soon after, Boasman submitted his thesis [6] concerning the energy shifts from the exact spectra of billiards caused by the leading-order semiclassical approximation. As part of his study, he discussed the T-operator method and applied it to the circle, the stadium and the Africa billiards. Haggerty [21] was the first to apply Bogomolny's transfer operator to a Hamiltonian system with a smooth potential. Bogomolny and Caroli [9] have recently studied the T-operator applied to a system consisting of a particle confined to a surface of constant negative curvature. Finally, Biechele, Goodings and the author have applied it to simple integrable systems that are not billiards, namely, the hydrogen atom in one or two dimensions and the two-dimensional harmonic oscillator.

In the fall of 1992, Tom Szeredi, David Goodings and I began to study Bogomolny's T-operator method. We applied a finite approximation to Bogomolny's quantization scheme to the circle billiard, consisting of a free particle confined inside a circle, and to the wedge billiard, consisting of a particle confined in a wedge of

half angle ϕ and subject to a constant force parallel to one side of the wedge. The circle billiard is an integrable system, whereas the wedge billiard can display all types of dynamical behaviour depending on the wedge angle ϕ. The wedge billiard is integrable for $\phi = 45°$, exhibits hard chaos for angles $\phi > 45°$ and soft chaos (or mixed behaviour) for angles $\phi < 45°$. The results of this study led to two publications, of which I am a co-author. Chapter 2 is our first paper, published in Physical Review Letters:

Szeredi T., Lefebvre J.H. and Goodings D.A., "Application of Bogomolny's Transfer Operator to Semiclassical Quantization of a Chaotic System", *Phys Rev Lett*, **71**, 2891 (1993).

It describes how to apply the T-operator method to the wedge billiard and reports on the results obtained for the first 20 energy eigenvalues for the wedge angle $\phi = 49°$ (a classically chaotic case). It also explains how to recover the actions of the periodic orbits for this system. Chapter 3 consists of our second paper, a more detailed version of the study reported in our first paper. It was published in Nonlinearity:

Szeredi T., Lefebvre J.H. and Goodings D.A., "Studies of Bogomolny's semiclassical quantization of integrable and nonintegrable systems", *Nonlinearity*, **7**, 1463 (1994).

Here, we report on the results for the circle billiard and five wedge billiards displaying different dynamical behaviour. In addition, a variant of Bogomolny's method based on symbolic dynamics is applied to the 49° wedge billiard.

My contributions to these papers are summarized as follows. I have been involved in all aspects of the study reported in these papers including the understanding and interpretation of Bogomolny's T-operator method, the development of analytic and numerical methods, and the analysis and interpretation of the results. In many cases, Tom Szeredi and I independently developed programs for the same tasks, to ensure the reliability of the results. In the remaining cases, the numerical work was shared between the two of us. The only part of the work for which I was not involved is Sec. 2.5 of the second paper concerning the finite approximations to the transfer operator and the dynamical zeta function. In preparing the manuscripts, Tom and I generated the figures and, while we both provided drafts for parts of the manuscripts, David Goodings was mainly responsible for writing both papers.

The specific sections of these papers for which I am primarily responsible are Sec. 2.3.1 (finding the source of the problem causing the spikes and providing a solution for eliminating them) and Sec. 3 of the second paper (the work relating to the T-operator and symbolic dynamics). Some of the interesting aspects of the latter work are the programs that I developed: (i) to find the irreducible orbits for the wedge billiard (based on the list of primitive periodic orbits that Tom Szeredi generated), (ii) to systematically decipher the pruning rules for the wedge billiard, (iii) to draw the symbolic partition in phase space, and (iv) to generate the approximate energy eigenvalues based on the periodic orbits.

Chapter 4 is a study of the eigenvalues of the T-operator for the circle and

wedge billiards. The objective of this study is to determine if the T-operator eigenvalues can provide a reliable characteristic to describe the manifestation of chaos in quantum systems. This idea originates from observations reported in Haggerty's thesis [21]. He noticed that, depending on the dynamics of the system, the T-operator eigenvalues behaved differently as a function of energy. In addition he observed that for the integrable case, the T-operator eigenvalues were related in a special way to the quantum numbers of the system. Based on the work of Lauritzen [28], I discuss the connection between T-operator eigenvalues and quantum numbers for the circle and 45° wedge billiards. In the last section of this chapter, I study the distribution of the phase separations of the T-operator eigenvalues for a regular system and a system displaying hard chaos. I show that the difference between these distributions is statistically significant and therefore may reflect the dynamical properties of the system. This finding is supported by the recent study of Rouvinez [37] on the phase separations of S-matrix eigenvalues.

One of the attractive features of Bogomolny's T-operator method is that, in addition to semiclassical energy eigenvalues, it is possible to calculate the semiclassical energy eigenfunctions in a relatively simple manner. In Chap. 5, I numerically construct the energy eigenfunctions for the circle and wedge billiards and demonstrate the success of this technique by comparing the results with the exact quantum solutions. Also, for the circle billiard, I show analytically how one may obtain the semiclassical WKB wavefunctions, by starting from Bogomolny's expression for the

wavefunctions and making use of the stationary phase approximation.

The concluding chapter, Chap. 6, provides an overview of the main results of this thesis and outlines projects, based on the T-operator method, which are currently in progress and recommended for future work. Finally, there are four appendices. Since the exact quantum solutions and the WKB solutions for the circle and 45° wedge billiards are often referred to throughout this thesis, they are provided in appendices A and B. The classical actions for the circle and 45° wedge billiards are given in Appendix C. The solutions for the wedge billiard are derived in more detail in Szeredi [39] and Rouvinez [37]. Appendix D is a derivation for the normal derivative in the plane perpendicular to an arbitrary trajectory, which is required to compute the wavefunctions.

Chapter 2

Application of Bogomolny's Transfer Operator to Semiclassical Quantization of a Chaotic System

The following is a reprint of our paper that appeared in Physical Review Letters:

Szeredi T., Lefebvre J.H. and Goodings D.A., "Application of Bogomolny's Transfer Operator to Semiclassical Quantization of a Chaotic System", *Phys Rev Lett*, **71**, 2891 (1993).

VOLUME 71, NUMBER 18 PHYSICAL REVIEW LETTERS 1 NOVEMBER 1993

Application of Bogomolny's Transfer Operator to Semiclassical Quantization of a Chaotic System

T. Szeredi, J. H. Lefebvre, and D. A. Goodings
Department of Physics and Astronomy, McMaster University, Hamilton, Ontario, Canada L8S 4M1
(Received 16 July 1993)

The transfer operator developed recently by Bogomolny is used to calculate approximate semiclassical energy eigenvalues for a chaotic system, the wedge billiard. Only four classical trajectories, starting and ending on the Poincaré surface of section and crossing it once in between, are required to calculate an element of the T matrix. A 100×100 T matrix is shown to give excellent results for the first 20 energy eigenvalues. It is also shown how the actions of the shortest periodic orbits of the 49° wedge can be obtained by calculating the Fourier transforms of $\mathrm{Tr}(T^m)$.

PACS numbers: 05.45.+b, 03.20.+i, 03.65.-w

Studies of the correspondence between classical mechanics and quantum mechanics have been mainly concerned with the following problem: given a classical system described by a time independent Hamiltonian and a detailed knowledge of the classical motion, what is the best method of estimating, in a semiclassical approximation, the energy eigenvalues and eigenfunctions of the analogous quantum system? If the classical system is integrable, one can employ the Einstein-Brillouin-Keller (EBK) quantization rules [1], which generally give excellent results for all but a few of the lowest energy eigenvalues. However, if the classical system is not integrable, as is the case for systems showing chaotic behavior, almost all approaches to the quantization problem make use of the Gutzwiller trace formula [1, 2] or its reformulation as a zeta product [3, 4]. The main difficulty with these methods is that the infinite sum or infinite product over the periodic orbits of the classical system is not, in general, absolutely convergent for real values of the energy E [5–7], although it may be conditionally convergent in some cases [8]. Furthermore, one is struck by the fact that it is necessary to know the intricacies of the classical dynamics on progressively smaller scales as one proceeds to longer periodic orbits in the infinite sum or infinite product of the Gutzwiller theory. This is disturbing because the uncertainty principle implies that, at a given energy E, there is a point beyond which the quantum system cannot "know" about the finer details of the classical motion.

Recently, Bogomolny [9,10] has developed an approach to the semiclassical quantization problem which is free of convergence difficulties and, in addition, allows the uncertainty principle to be built into the theory in a natural way. His approach is based on introducing a Poincaré surface of section (PSOS) which is crossed by many trajectories of the classical system. Employing a Green's function theory closely related to Gutzwiller's original formulation [2], he developed a transfer operator $T(q'', q')$ which takes one from an initial point q' on the PSOS to a final point q'' on the PSOS. The transfer operator involves a sum over all possible classical trajectories which cross the PSOS only once in going from q' to q'' and have the normal component of the momentum in the same direction at q' and q''. For a system with 2 degrees of freedom it has the form [see Bogomolny [9], Eq.(4.18)]

$$T(q'', q') = \sum_{\mathrm{cl\,tr}} \frac{1}{(2\pi i\hbar)^{1/2}} \left| \frac{\partial^2 S(q'', q'; E)}{\partial q'' \partial q'} \right|^{\frac{1}{2}} \times \exp[iS(q'', q'; E)/\hbar - i\nu\pi/2]. \quad (1)$$

Here $S(q'', q'; E)$ is the action at energy E calculated along a classical trajectory connecting the points q' and q'' and crossing the PSOS only once in between. The phase index ν is related to the number of points on the trajectory at which the semiclassical approximation is not valid. For the rectangular billiard, which is integrable, Lauritzen [11] has shown how Eq. (1) and a suitable PSOS lead to the exact energy eigenvalues.

Suppose one wishes to calculate the quantum energy eigenvalues E_j of a given system up to a certain energy E. Associated with the coordinate q on the PSOS and its conjugate momentum p is a certain area $A(E)$ of phase space accessible to the system at energy E. The number of "Planck cells" corresponding to this area is

$$N(E) = \frac{A(E)}{2\pi\hbar}. \quad (2)$$

One then divides the PSOS into $N(E)$ segments or "cells" labeled by n, the width of the nth cell being Δ_n. A simple finite approximation to the T operator is obtained by taking matrix elements of $T(q'', q')$ in the orthonormal basis $\{\psi_n\}$ in which $\psi_n(q) = \Delta_n^{-1/2}$ if q is in cell n, and otherwise is zero. In this basis, the T operator is represented by an $N(E) \times N(E)$ matrix, and the condition for an energy eigenvalue is that

$$\det(\delta_{mn} - T_{mn}) = 0, \quad (3)$$

where $T_{mn} = T(q_m, q_n)(\Delta_m \Delta_n)^{1/2}$ (see Bogomolny [9], Sec. 8).

In this paper we describe how a finite approximation to the T operator yields approximate semiclassical energy eigenvalues for the wedge billiard, a chaotic system with a nonconstant potential. This system is different from the force-free billiards recently studied by Bohsman

0031-9007/93/71(18)/2891(4)$06.00

VOLUME 71, NUMBER 18 PHYSICAL REVIEW LETTERS 1 NOVEMBER 1993

[12], who used a perturbation approach to investigate the differences between the semiclassical and exact energy eigenvalues.

The wedge billiard has been studied both classically and quantum mechanically by a number of people [7,13–19]. It consists of a particle confined to the region between the y axis and the line $y = x\cot\phi$, where ϕ is the wedge angle. The particle makes elastic collisions with the boundaries and is acted upon by a constant force in the negative y direction. If the mass of the billiard and the strength of the constant force are chosen to be unity, the Hamiltonian is

$$H = \frac{1}{2}(p_x^2 + p_y^2) + y, \qquad x \geq 0, \qquad y \geq x\cot\phi. \tag{4}$$

For wedge angles between 45° and 90° this system exhibits hard chaos [17–19], that is, there are no Kolmogorov-Arnol'd-Moser (KAM) tori in the phase space and all periodic orbits are unstable.

To apply Bogomolny's theory, we choose the PSOS to be a straight line running along the tilted wall of the wedge. For a given energy E, the maximum distance from the vertex that the classical billiard can reach along the tilted wall is $d = E/\cos\phi$. Also, it is not hard to show from Eq. (2) that for this choice of the PSOS,

$$N(E) = \frac{2\sqrt{2}}{3\pi\hbar\cos\phi}E^{3/2}. \tag{5}$$

Thus, if one wishes to calculate the energy eigenvalues E_j up to some energy E, the number of cells along the PSOS should be at least as large as $N(E)$ given by this equation, and the width Δ, assumed to be constant, should be chosen to be $d/N(E)$.

To construct a finite approximation to the transfer operator, we require the action at energy E for a classical trajectory connecting points q_m and q_n in the centers of cells m and n. This is given by

$$S(q'', q'; E) = W(q'', q'; T) + ET, \tag{6}$$

with [20]

$$W(q'', q'; T) = \frac{1}{2T}[(x''-x')^2+(y''-y')^2] - \frac{T}{2}(y'+y'') - \frac{T^3}{24} \tag{7}$$

and

$$T = \frac{\partial S}{\partial E}, \quad E = -\frac{\partial W}{\partial T}. \tag{8}$$

Here (x', y') and (x'', y'') are the coordinates of the points q' and q'' on the PSOS. Differentiating Eq. (7) with respect to T and setting the result equal to $-E$, one obtains a quadratic equation in T. The two solutions correspond to the two classical paths connecting q' and q'', one a "low path," the other a "high path." Substituting the two solutions for T in (6) yields $S(q'', q'; E)$ for these two paths. With the help of a computer algebra program, we can also calculate the second derivatives of $S(q'', q'; E)$ appearing in Eq. (1).

In addition to the two direct trajectories, which were denoted as T mappings in previous work [7,16], there are two trajectories which make a reflection from the vertical wall in going from q' to q''. These will be denoted as V mappings. The corresponding functions $S(q'', q'; E)$ are readily calculated by the device shown in Fig. 1 where the reflection at the vertical wall is ignored and the particle ends up on the mirror image of the tilted wall.

Finally, the phase index ν must be calculated for each of the classical trajectories from q' to q''. For our system with 2 degrees of freedom, ν is equal to the number of caustics on the trajectory, plus 2 for each reflection from the boundary, plus 1 for each time the total momentum becomes zero (at the top of a vertical rise and fall). For each of the four trajectories of Fig. 1 it happens that there is at most one caustic. When a caustic occurs, it can be detected through a change in sign of the second derivative $\partial^2 S(q, q'; E)/\partial q \partial q'$, evaluated first at $q = q'$ and then at $q = q''$.

The results of a calculation of the transfer operator for the 49° wedge are shown in Fig. 2. Because the matrix elements T_{mn} are complex, what is plotted is the modulus of $\det|1 - T(\tilde{E})|$ as a function of the scaled energy $\tilde{E}$. [$\tilde{E} = Ed_{TF}(E)/3$, where $d_{TF}(E)$ is the Thomas-Fermi density of states. As a function of $\tilde{E}$ the mean spacing between the energy eigenvalues is close to unity [7].] The T matrix in this calculation was 100 × 100, corresponding to 100 cells of equal width Δ along the tilted wall, extending from the wedge vertex out to a distance of $d_{max} = 15.25$ (in units in which $\hbar = 1$). This maximum distance corresponds to a maximum energy of $E_{max} = y_{max} = d_{max}\cos\phi = 10.0$. The dashed lines in Fig. 2 correspond to the exact energy eigenvalues E_n obtained from an accurate solution of the Schrödinger equation [7]. It may be seen from the figure that there is excellent agreement between the positions of the minima of $|\det|1 - T(\tilde{E})||$ and the exact energy eigenvalues. Taken over the lowest 20 eigenvalues (which lie below $E_{max} = 10.0$), the mean deviation of the minima from the exact $\tilde{E}_n$ is $\langle \tilde{E}_{min} - \tilde{E}_n \rangle = 0.024$, and the rms deviation is $\langle (\tilde{E}_{min} - \tilde{E}_n)^2 \rangle^{1/2} = 0.065$. The latter value is smaller than the rms deviation of any of our earlier re-

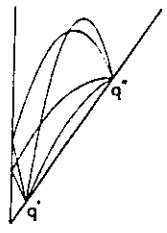

FIG. 1. Diagram showing the four classical trajectories used to calculate the transfer operator for the wedge billiard.

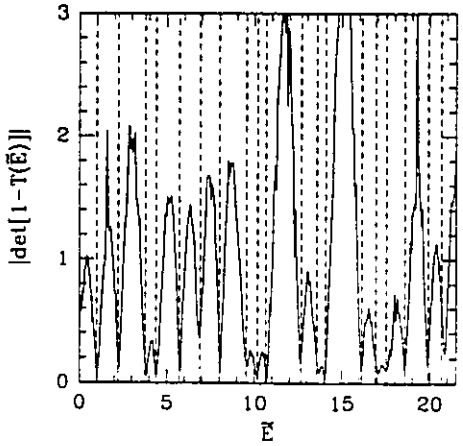

FIG. 2. Plot of $|\det[1 - T(\tilde{E})]|$ as a function of the scaled energy $\tilde{E}$ for the wedge billiard with $\phi = 49°$. The T matrix used was 100×100. The dashed lines indicate the positions of the exact energy eigenvalues $\tilde{E}_n$.

sults obtained using quantization schemes based on the dynamical zeta function [7]. To obtain this degree of accuracy we found it necessary to choose the number of cells on the PSOS to be about 6 times the number of Planck cells defined by Eq. (2). [With $E_{max} = 10.0$, Eq. (5) gives $\mathcal{N}(E_{max}) = 15$.] Increasing the number of cells beyond 100, however, made very little difference in the results over this energy range.

It is interesting to see how the periodic orbits of the system can be obtained from the transfer operator formalism. The key to doing this is the relation (see Bogomolny [9], Sec. 6)

$$\ln \zeta_S(E) = -\sum_{\gamma}\sum_{n=1}^{\infty} \frac{\exp[i n(S_\gamma/\hbar - \nu_\gamma \pi/2)]}{n|\det(M_\gamma^n - 1)|^{1/2}} = -\sum_{m=1}^{\infty} \frac{1}{m} \mathrm{Tr}(T^m). \quad (9)$$

Here $\zeta_S(E)$ is the Selberg zeta function or dynamical zeta function, which can be expressed as an infinite product over the periodic orbits of the system. The sum over γ is over the primitive periodic orbits of the system, with S_γ the action, M_γ the monodromy matrix, and ν_γ the Maslov index of a primitive periodic orbit. The sum over n counts the number of traversals of a given primitive periodic orbit. In the sum over m, the trace of T^m is nonzero only when there is a sequence of m mappings which starts and ends in the same cell of the PSOS. In order that these m segments make up a periodic orbit, the trajectories must join smoothly at each crossing and the initial momentum must be equal to the final momentum. How this is achieved has been described by Bogomolny[9] and by Boasman [12].

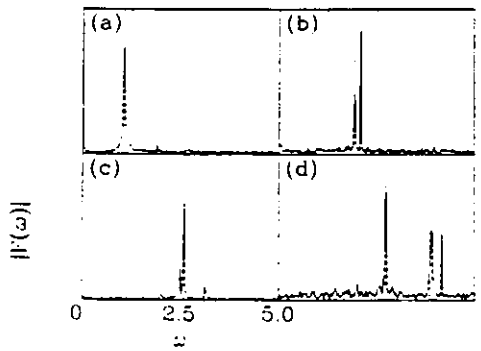

FIG. 3. Results for the 49° wedge of the Fourier transforms of $\mathrm{Tr}(T^m)$ calculated from Eq. (10): (a) $|F_1(\omega)|$; (b) $|F_2(\omega)|$; (c) $|F_3(\omega)|$; (d) $|F_4(\omega)|$. The T matrix used was 200×200. The dashed lines occur at the actions $S_\gamma(1)$ of the shortest periodic orbits.

The periodic orbits are obtained by calculating the Fourier transform of Eq. (9). Since the actions of the wedge billiard scale with energy according to [7,16] $S_\gamma(E) = S_\gamma(1)E^{3/2}$, we put $u = E^{3/2}$ and define the Fourier transform of $\mathrm{Tr}(T^m)$ as

$$F_m(\omega) = \int_0^{u_{max}} \mathrm{Tr}(T^m) \exp(-i\omega u) du. \quad (10)$$

The results for the first four traces for the 49° wedge are shown in Fig. 3. In order to get good accuracy, the T matrix used in the calculations was constructed using 200 cells extending from the vertex out to $d_{max} = 62$ along the tilted wall, and the integrand in Eq. (10) was computed at 512 points extending out to $u_{max} = (40.5)^{3/2} = 258$. The vertical dashed lines in Fig. 3 lie at the positions $S_\gamma(1)$ of the shortest periodic orbits of the 49° wedge. (See Szeredi and Goodings [7], Table I, for the actions of these orbits and their labels.) It is satisfying to see that $F_1(\omega)$ has a single peak at the action of the V orbit, while $F_2(\omega)$ has peaks at the actions of TV and V^2. Furthermore, $F_3(\omega)$ has peaks at the actions of TVV and V^3, and $F_4(\omega)$ has peaks at the actions of $TTVV$, $(TV)^2$, $TVVV$, and V^4 (in order of increasing actions).

In our previous work we found that the Gutzwiller periodic orbit theory gave much better results for the 60° wedge than for the 49° wedge, a feature we attributed to the greater "pruning" of periodic orbits in the case of the 49° wedge. In contrast, the results reported here for the 49° wedge are of comparable accuracy to similar calculations performed for the 60° wedge. Moreover, Bogomolny's method gives excellent results for the 45° wedge, an integrable case. Thus, the transfer operator appears to work very well for all wedge angles $\phi \geq 45°$.

In conclusion, we note that finite approximations to

Bogomolny's transfer operator have several noteworthy features. First, one needs to take into account only a small number of different types of trajectories from one point to another on the PSOS, in contrast to the infinite number of periodic orbits in the Gutzwiller trace formula and the dynamical zeta function. Although we have found that good numerical accuracy requires about 6 times more cells on the PSOS than the number of Planck cells given by Eq. (2), there are no formal convergence problems. Finally, we have shown how taking the Fourier transforms of $\mathrm{Tr}(T^m)$ allows one to recover the periodic orbits. The problem of obtaining the correct phases for the periodic orbits is more complicated and will be described in a subsequent paper.

We would like to thank E. Bogomolny for encouraging us to try this approach and for drawing our attention to Boasman's Ph.D. thesis. This work was supported by the Natural Sciences and Engineering Research Council of Canada.

[1] M.C. Gutzwiller, *Chaos in Classical and Quantum Mechanics* (Springer-Verlag, New York, 1990).
[2] M.C. Gutzwiller, J. Math. Phys. **12**, 343 (1971).
[3] M.V. Berry, in *Quantum Chaos and Statistical Nuclear Physics*, edited by T.H. Seligman and H. Nishioka, Lecture Notes in Physics Vol. 263 (Springer, Berlin, 1986), p. 1.
[4] A. Voros, J. Phys. A **21**, 685 (1988).
[5] B. Eckhardt and E. Aurell, Europhys. Lett. **9**, 509 (1989).
[6] M. Sieber and F. Steiner, Phys. Lett. A **144**, 159 (1990).
[7] T. Szeredi and D.A. Goodings, Phys. Rev. E (to be published).
[8] M. Sieber and F. Steiner, Phys. Rev. Lett. **67**, 1941 (1991).
[9] E. Bogomolny, Nonlinearity **5**, 805 (1992).
[10] E. Bogomolny, Chaos **2**, 5 (1992).
[11] B. Lauritzen, Chaos **2**, 409 (1992).
[12] P.A. Boasman, Ph.D. thesis, University of Bristol, 1992.
[13] H.E. Lehtihet and B.N. Miller, Physica (Amsterdam) **21D**, 93 (1986).
[14] P.H. Richter, H.-J. Scholz, and A. Wittek, Nonlinearity **3**, 45 (1990).
[15] A. Wittek, doctoral thesis, University of Bremen, 1991.
[16] T. Szeredi and D.A. Goodings, Phys. Rev. Lett. **69**, 1640 (1992).
[17] M.P. Wojtkowski, Commun. Math. Phys. **126**, 507 (1990).
[18] N.D. Whelan, D.A. Goodings, and J.K. Cannizzo, Phys. Rev. A **42**, 742 (1990).
[19] N.i. Chernov, Physica (Amsterdam) **53D**, 233 (1991).
[20] L.S. Schulman, *Techniques and Applications of Path Integration* (Wiley, New York, 1981), p. 38.

Chapter 3

Studies of Bogomolny's semiclassical quantization of integrable and nonintegrable systems

The following is a reprint of our paper that appeared in Nonlinearity:

Szeredi T., Lefebvre J.H. and Goodings D.A., "Studies of Bogomolny's semiclassical quantization of integrable and nonintegrable systems", *Nonlinearity*, **7**, 1463 (1994).

Nonlinearity 7 (1994) 1463–1493. Printed in the UK

Studies of Bogomolny's semiclassical quantization of integrable and nonintegrable systems

T Szeredi†, J H Lefebvre and D A Goodings

Department of Physics and Astronomy, McMaster University, Hamilton, Ontario, Canada L8S 4M1

Abstract. The semiclassical quantization scheme formulated by Bogomolny, employing a suitably chosen Poincaré surface of section (PSS), has been used to calculate approximate energy eigenvalues for the quantum analogues of several Hamiltonian systems. Using a finite approximation to the transfer operator in coordinate space, we have carried out calculations of the energy eigenvalues for the circle billiard and the 45° wedge billiard, both of which are integrable systems. Calculations have also been performed for the 49° and 60° wedges, which classically exhibit hard chaos, and for the 41° and 30° wedges which classically exhibit soft chaos or mixed behaviour. In all cases, the low-lying energy eigenvalues are in excellent agreement with the exact quantum energy eigenvalues and, in the case of the 49° wedge, are better than the results obtained using any other semiclassical quantization scheme. We have also studied a variant of Bogomolny's approach which employs the symbolic dynamics to construct a representation of the transfer operator. We show explicitly for the 49° wedge billiard how the accessible part of the PSS in phase space is divided into cells labelled by sequences of n symbols. This leads to a systematic way of finding the pruning rules for this system. Results are presented for the 49° wedge based on schemes employing 2-, 3- and 4-symbol cells. Because of the extensive pruning in this system, this approach cannot be easily implemented for the general case of n-symbol cells. Furthermore, the numerical results are not as good as those obtained from finite approximations to the transfer operator in coordinate space.

PACS numbers: 0545, 0320, 0365

1. Introduction

This paper reports the results of studies of Bogomolny's semiclassical quantization scheme [1, 2] for both integrable and nonintegrable systems. Central to Bogomolny's formalism is a suitably chosen Poincaré surface of section (PSS) which is crossed many times by a general trajectory of the system. The PSS is divided into a number of cells having approximately the same phase-space volume, and a semiclassical transfer operator is constructed which describes a mapping from one cell to another. Depending on how the cells are chosen, the transfer operator takes different forms. A semiclassical quantization condition follows from making a finite approximation to the transfer operator.

Bogomolny's formalism has the appealing features that there are no formal convergence problems, and the Heisenberg uncertainty principle can be built into the theory in a natural way. It has been applied successfully to an integrable system, the rectangular billiard [3], and to systems exhibiting hard chaos, namely the geodesic flow on surfaces of constant negative curvature [4] and the 49° wedge billiard [5]. An interesting study [6] has also been carried out applying Bogomolny's transfer operator to a smooth nonscalable potential

† Present address: Department of Applied Mathematics, The Open University, Milton Keynes MK7 6AA, UK.

0951-7715/94/051463+31$19.50

(the Nelson potential) at two fixed energies, corresponding to classical motion being mostly regular in one case and mostly chaotic in the other. However, there are interesting questions that arise in applying this formalism to any given system. First, what is the best choice for the Poincaré surface of section? Second, given a PSS, what is the best way to choose the cells? For example, does a representation of the transfer operator in terms of the symbolic dynamics, when known, offer any advantages over a coordinate space representation? Thirdly, how many cells are required to give good accuracy for the energy eigenvalues E_j below some energy E? It would also be interesting to know if there are any significant differences in applying Bogomolny's quantization scheme to integrable and nonintegrable systems. Finally, can the transfer operator approach be applied in a straightforward way to a system which classically exhibits soft chaos or mixed behaviour? There is special interest in this question since quantization schemes based on the Gutzwiller trace formula [7, 8], including the dynamical zeta function [9–14], cannot be readily applied when there is a close intermingling of stable and unstable periodic orbits in the classical phase space.

In this paper we attempt to shed some light on these questions. As examples of integrable systems we study the circle billiard and the 45° wedge billiard. Examples of nonintegrable systems are provided by the 60°, 49°, 41° and 30° wedge billiards, for all of which accurate values of the quantum energy eigenvalues are known. In the next section, we describe studies of the transfer operator in coordinate space. Section 3 describes how the symbolic dynamics can be used to construct a representation of the transfer operator. The final section summarizes and discusses what we have learned.

It should be mentioned that there are interesting similarities between Bogomolny's formalism, based on a suitable PSS, and the scattering theory approach to the semiclassical quantization problem for compact billiards developed by Doron and Smilansky [15, 16], based on removing an interval of the billiard's boundary and treating the scattering of de Broglie waves incident on the opening via a long waveguide. Their formulation leads to an equation similar to (2) below for the energy eigenvalues of the (closed) billiard system, in which the transfer matrix $T(E)$ is replaced by the scattering matrix $S(E)$. Further discussion of the relationship between the two theories may be found in [15, 16].

2. The transfer operator in coordinate space

2.1. Methods for calculating the semiclassical energy eigenvalues

In Bogomolny's theory, the transfer operator is defined with respect to a given Poincaré surface of section (PSS). Although the PSS can be chosen in many different ways, the calculations are conceptually simple if one picks a 'surface' in the coordinate space that is frequently crossed by the classical paths. For a system with two freedoms, the PSS is simply a one-dimensional curve. If q' and q'' are points on this curve, one obtains the transfer operator by summing over all possible classical trajectories which cross the PSS only once in going from q' to q'' and have the normal component of the momentum in the same direction at q' and q''. The result is (see [1, equation (4.18)]),

$$T(q'',q') = \sum_{\text{cl.tr.}} \frac{1}{(2\pi \mathrm{i}\hbar)^{1/2}} \left| \frac{\partial^2 S(q'',q';E)}{\partial q'' \partial q'} \right|^{\frac{1}{2}} \exp[\mathrm{i}S(q'',q';E)/\hbar - \mathrm{i}\nu\pi/2]. \qquad (1)$$

Here $S(q'',q';E)$ is the action at energy E calculated along a classical trajectory connecting the points q' and q'' and crossing the PSS only once in between. The phase index ν is related to the number of points on the trajectory at which the semiclassical approximation is not valid.

Bogomolny's semiclassical quantization scheme

One possible way of constructing a finite approximation to the T-operator in coordinate space is to divide the accessible part of the PSS into N cells, the nth cell centred on q_n having width Δ_n. In terms of the transfer operator $T(q_m, q_n)$ from q_m in cell m to q_n in cell n, the matrix element T_{mn} is defined to be,

$$T_{mn} = T(q_m, q_n)(\Delta_m \Delta_n)^{1/2}. \tag{2}$$

Then the condition for an energy eigenvalue is that (see [1, section 8]),

$$\det[\delta_{mn} - T_{mn}(E)] = 0. \tag{3}$$

The dimension of the T-matrix is, of course, equal to the number of cells N on the PSS.

Bogomolny writes down a prescription for the minimum number of cells required for a reasonably good numerical calculation. Suppose one wishes to calculate semiclassical energy eigenvalues E_j up to some given energy E. The coordinate q along the PSS and its conjugate momentum p lie within an area $A(E)$ of phase space accessible to the system at energy E. We shall use the term *Planck cell* to denote a region of the PSS with phase-space area equal to Planck's constant h. Then the number of Planck cells on the PSS accessible to the system at energy E is,

$$N_P(E) = A(E)/h = A(E)/(2\pi\hbar). \tag{4}$$

Bogomolny argues that the T-matrix of dimension $N_P(E)$ constructed in this way will be approximately unitary. He also emphasizes that in performing numerical calculations one must choose N greater than $N_P(E)$ to obtain good numerical accuracy. For force-free billiards, Boasman [17] has pointed out that Bogomolny's criterion for the minimum number of cells, equation (4), corresponds to taking 2 cells on the PSS in coordinate space per de Broglie wave length at energy E.

The finite approximation leading to (3) has the effect of making the solutions for the energy eigenvalues E_j complex, though usually with small imaginary parts. The real parts can be determined by locating the minima of $|\det[1 - T(E)]|$ plotted as a function of E. An example will be shown later in this section (figure 1). However, there is an alternative method which we have found gives better results.

It has been shown by Artuso, Aurell and Cvitanović [18] and by Bogomolny [1] that there is a formal relationship between the dynamical zeta function $\zeta_S(E)$ and the transfer operator $T(E)$:

$$\zeta_S(E) = \det[1 - T(E)]. \tag{5}$$

For a system with two freedoms displaying hard chaos (all periodic orbits unstable) the dynamical zeta function can be written as [10],

$$\zeta_S(E) = \prod_{\gamma} \prod_{m=0}^{\infty} \{1 - \exp[i(S_\gamma/\hbar - \nu_\gamma \pi/2) - (m + 1/2)u_\gamma]\}, \tag{6}$$

where S_γ is the action, ν_γ is the Maslov index and u_γ is the stability exponent of the primitive periodic orbit γ. Provided the infinite product in this expression for $\zeta_S(E)$ is not truncated, its zeros are the (real) semiclassical energy eigenvalues.

Bogomolny has shown [1] that when E is real, the dynamical zeta function satisfies the following relation, known as the *functional equation*:

$$\exp[-i\pi \bar{N}(E)]\zeta_S(E) = \exp[i\pi \bar{N}(E)]\zeta_S^*(E). \tag{7}$$

Here the asterisk denotes the complex conjugate and $\bar{N}(E)$ is the mean number of energy eigenstates with energy less than or equal to E. From (5) this implies that $\exp[-i\pi \bar{N}(E)]\det[1 - T(E)]$ is a real function. When a finite approximation is made

to $T(E)$, as described above, this function is no longer guaranteed to be real. Nevertheless, guided by these considerations we assume that with a finite approximation to the transfer operator, as in (2), the semiclassical energy eigenvalues can be calculated to good accuracy by finding the (real) solutions of,

$$D(E) = \mathrm{Re}\{\exp[-\mathrm{i}\pi \bar{N}_{TF}(E)]\det[\delta_{mn} - T_{mn}(E)]\} = 0. \tag{8}$$

This will be referred to as the *functional determinant*. It is the basis for most of the calculations of energy eigenvalues described in the rest of the paper. Note that we have replaced $\bar{N}(E)$ by the Thomas–Fermi approximation to the number of energy eigenstates having energy equal to or less than E.

In the rest of this section we describe how these methods can be used to calculate approximate semiclassical energy eigenvalues for several different systems, both integrable and nonintegrable.

2.2. *The circle billiard*

The circle billiard, in which a free particle is confined inside a circle of radius R, is an example of an integrable system with two freedoms. Some aspects of the classical motion have been described by Berry [19]. Recently, Boasman [17] has used the circle billiard as a test case to study the difference between the energy eigenvalues calculated using the exact and the semiclassical propagators in the 'boundary integral method'. Here we focus on the semiclassical energy eigenvalues calculated by the methods outlined above and compare them with the exact energy eigenvalues.

A natural choice for the PSS is the circular boundary itself, with the transfer operator taking the particle from just after a collision with the boundary to just after the next collision. The coordinate q is simply the distance around the circumference from a chosen reference point. The PSS is divided into N cells of equal width $\Delta = 2\pi R/N$. Between the central points q_m and q_n of cells m and n there is only one classical trajectory, a straight line which crosses the PSS just once before being reflected from the boundary and returning to the PSS. For such a trajectory it is easy to calculate the action $S(q_m, q_n; E)$ and the second derivative appearing in (1):

$$S(q_m, q_n; E) = 2R(2mE)^{1/2} \sin\left(\frac{|q_m - q_n|}{2R}\right) \tag{9}$$

$$\left|\frac{\partial^2 S}{\partial q_m \partial q_n}\right| = \frac{(2mE)^{\frac{1}{2}}}{2R} \sin\left(\frac{|q_m - q_n|}{2R}\right). \tag{10}$$

Since there are no caustics along the straight line from q_m to q_n, the phase index ν_{mn} is always 2 as a result of the phase change from the single reflection at the circle boundary.

Suppose that we wish to calculate the energy eigenvalues E_j up to some value E. It is easy to see that the corresponding phase-space area associated with the circular PSS is $4\pi R(2mE)^{1/2}$, and thus $N_{\mathrm{P}}(E) = 2R(2mE)^{1/2}/\hbar$. To obtain estimates of the low-lying energy eigenvalues of a billiard in a circle of radius $R = 2$, we choose $E = 20$, in units in which $m = \hbar = 1$. This gives $N_{\mathrm{P}}(E) = 25$. Because the matrix elements T_{mn} are complex, we show in figure 1 the result of calculating $|\det[\delta_{mn} - T_{mn}(E)]|$ as a function of E over the energy range spanned by the lowest 19 energy eigenvalues. The dashed lines in the figure indicate the positions of the exact energy eigenvalues of the Schrödinger equation of a free particle inside a circle of radius R=2. These are given by,

$$E_{kn} = \frac{\hbar^2}{2m}\left(\frac{\alpha_k^{(n)}}{R}\right)^2 \tag{11}$$

Bogomolny's semiclassical quantization scheme

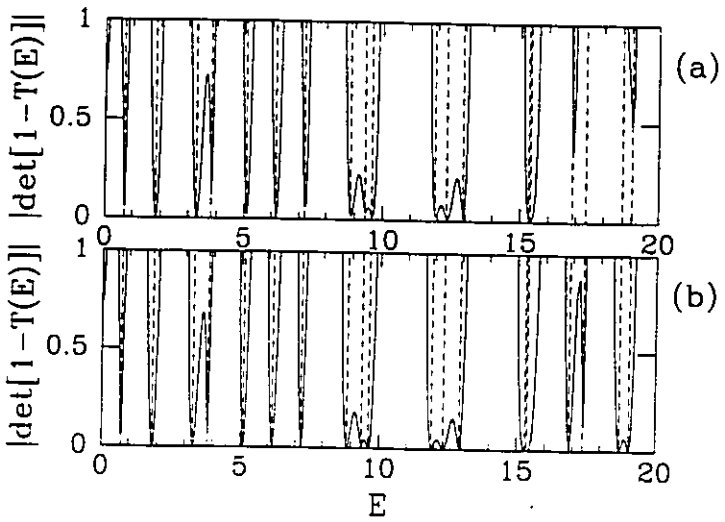

Figure 1. Plots of $|\det[1 - T(E)]|$ as a function of E for the circle billiard with $R = 2$. The dashed lines indicate the positions of the exact energy eigenvalues given by (11). (*a*) calculated with a 25×25 T-matrix; (*b*) calculated with a 100×100 T-matrix.

where $\alpha_k^{(n)}$ is the kth zero of the Bessel function $J_n(x)$. figures 1(*a*) and 1(*b*) show the results for T-matrices of dimensions 25 and 100 respectively. We see that there is excellent agreement between the positions of the minima of $|\det[1 - T(E)]|$ and the positions of the exact energy eigenvalues. In fact, even the 14th and 15th eigenvalues, which are very close together, are found to be resolved when the calculated curve of figure 1(*b*) is enlarged in this region. However, it is interesting to note that the 25×25 T-matrix fails to produce minima (lying below 1.0) at the 17th and 18th energy eigenvalues, whereas the 100×100 T-matrix gives deep minima at these positions.

2.3. The wedge billiard

The wedge billiard has been studied both classically and quantum mechanically by a number of people [20–28]. It consists of a particle confined to the region between the y-axis and the line $y = x \cot\phi$, where ϕ is the wedge angle. The particle makes elastic collisions with the boundaries and is acted upon by a constant force in the negative y-direction. If the mass of the billiard and the strength of the constant force are chosen to be unity, the Hamiltonian is,

$$H = \tfrac{1}{2}(p_x^2 + p_y^2) + y \qquad x \geqslant 0 \qquad y \geqslant x \cot\phi. \tag{12}$$

For wedge angles between 45° and 90° this system exhibits hard chaos [26–28], that is, there are no KAM tori in the phase space and all periodic orbits are unstable. For wedge angles less than 45° the system exhibits soft chaos or mixed behaviour characterized by the existence of both stable and unstable periodic orbits. Separating these two different regimes is the integrable case of $\phi = 45°$.

Of central importance in Bogomolny's formalism is the PSS, which can be chosen in many different ways. For the wedge billiard a natural choice is a straight line along the tilted wall of the wedge, since the billiard bounces repeatedly against this wall and the classical mappings of this wall into itself are easily written down. For a given energy E, the maximum distance from the vertex that the classical particle can reach along this wall

is $r_{max} = E/\cos\phi$. In previous work [5] we divided r_{max} into N cells of equal width Δ. Let us denote the position coordinate along the PSS as r and its conjugate momentum as p_r. Since at position r and energy E we must have $|p_r| \leqslant [2(E - r\cos\phi)]^{1/2}$, it follows that cells of equal width Δ give unequal phase-space areas on the full PSS in phase space. Although this did not seem to cause difficulties in our earlier work, in the present paper we shall always choose the cell widths Δ_n to make the phase-space areas equal, as illustrated in figure 2. This has the satisfying feature that the smaller cell widths near the vertex are

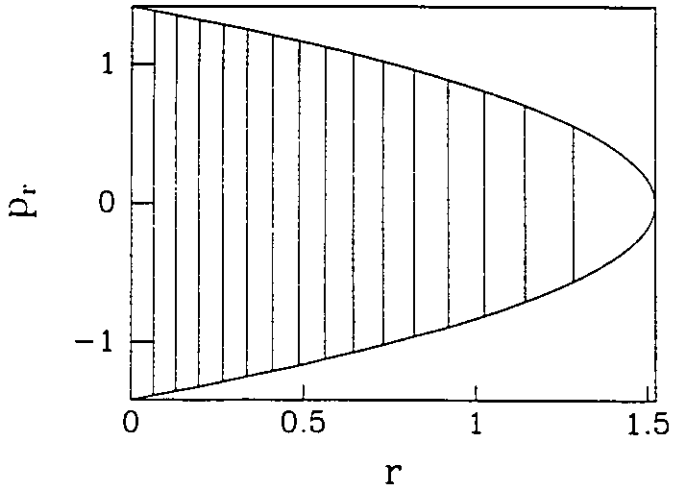

Figure 2. The full Poincaré surface of section in the phase space (r, p_r), corresponding to the tilted wall of the wedge. The areas of the slices are equal, and this determines the cell widths Δ_n.

consistent with the de Broglie wave length being shorter in this region. From the definition in (4) it is easy to show that for the PSS chosen along the tilted wall of the wedge, the number of Planck cells accessible at energy E is,

$$N_P(E) = \frac{2\sqrt{2}}{3\pi\hbar\cos\phi}E^{3/2}. \tag{13}$$

This corresponds to each vertical slice in figure 2 having a phase-space area of exactly $2\pi\hbar$, which in turn implies that there are two cells per de Broglie wave length at each position along the PSS in coordinate space.

To construct a finite approximation to the transfer operator, we require the action at energy E for a classical trajectory connecting points q_m and q_n at the centres of cell m and n. This can be obtained from the exact time-dependent function [29],

$$W(q'', q'; T) = \frac{1}{2T}[(x'' - x')^2 + (y'' - y')^2] - \frac{T}{2}(y' + y'') - \frac{T^3}{24} \tag{14}$$

where, (x', y') and (x'', y'') are the coordinates of the points q' and q'' on the PSS. For a given classical trajectory from q' to q'', the quantity we require in (1) is related to $W(q', q''; T)$ by a Legendre transformation,

$$S(q'', q'; E) = W(q'', q'; T) + ET \tag{15}$$

with,

$$T = \frac{\partial S}{\partial E} \qquad \text{and} \qquad E = -\frac{\partial W}{\partial T}. \tag{16}$$

Bogomolny's semiclassical quantization scheme

Differentiating (14) with respect to T and setting the result equal to $-E$, one obtains a quadratic equation in T. The two solutions correspond to the two classical paths connecting q' and q'', one a 'low path', the other a 'high path'. Substituting the two solutions for T in (15) yields $S(q'', q'; E)$ for these two paths. With the help of a computer algebra program, we can also calculate the second derivatives of $S(q'', q'; E)$ appearing in (1).

In addition to the two direct trajectories, which were denoted as T-mappings in previous work [23–25], there are two trajectories which make a reflection from the vertical wall in going from q' to q''. These will be denoted as V-mappings. The corresponding actions $S(q'', q'; E)$ and their second derivatives are readily calculated by the device shown in figure 3 where the reflection at the vertical wall is ignored and the particle ends up on the mirror image of the tilted wall.

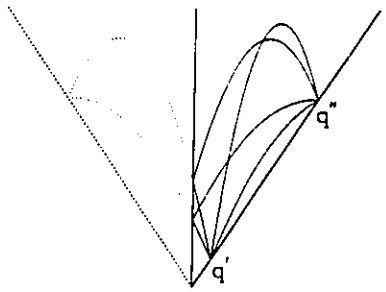

Figure 3. Diagram showing the four classical trajectories used to calculate the transfer operator for the wedge billiard.

Finally, the phase index ν must be calculated for each of the classical trajectories from q' to q''. For our system with two freedoms, ν is equal to the number of caustics on the trajectory, plus 2 for each reflection from the boundary, plus 1 for each time the total momentum becomes zero (at the top of a vertical rise and fall). For each of the four trajectories of figure 3 it happens that there is at most one caustic. When a caustic occurs, the second derivative $\partial^2 S(q'', q'; E)/\partial q'' \partial q'$ changes sign. A caustic can therefore be detected by examining the sign of this second derivative and comparing it with the known sign when no caustic occurs (positive for a T-bounce, negative for a V-bounce).

To review briefly, we first choose E_{max} and r_{max}, and divide the PSS into N cells of equal phase-space area, as in figure 2, the nth cell centred on q_n having width Δ_n. The corresponding $N \times N$ T-matrix is then constructed from (1) and (2) using the method just described. Finally, the approximate semiclassical energy eigenvalues of the quantum system are to be determined from either the minima of $|\det[\delta_{mn} - T_{mn}(E)]|$ or from the zeros of the functional determinant, equation (8).

In presenting the results of our calculations and comparing them with the exact energy eigenvalues, it is helpful to introduce a scaled energy $\tilde{E}$ defined so as to make the eigenvalues evenly spaced on the average, with the mean spacing equal to unity. This can be achieved in the following way. First we introduce the function $N_{TF}(E)$, which is the Thomas–Fermi approximation to the number of energy eigenstates of the quantum system with eigenvalues less than or equal to E. For the wedge of angle ϕ this is given by [25],

$$N_{TF}(E) = \frac{\tan\phi}{12\pi\hbar^2}E^3 - \frac{(1+\sec\phi)}{3\sqrt{2\pi}\hbar}E^{3/2} + \frac{1}{6}. \tag{17}$$

By differentiating with respect to E one obtains the Thomas–Fermi density of states, $d_{TF}(E)$, which is the mean number of energy eigenstates per unit energy at energy E. The scaled

energy $\tilde{E}$ is then defined to be,

$$\tilde{E} = Ed_{\mathrm{TF}}(E)/3 = \frac{\tan\phi}{12\pi\hbar^2}E^3 - \frac{(1+\sec\phi)}{6\sqrt{2\pi\hbar}}E^{3/2}. \tag{18}$$

With this definition the scaled energy eigenvalues $\tilde{E}_n$ have a mean spacing close to unity.

If we keep only the first term on the right-hand side of (18), we can recast (13) for $N_{\mathrm{P}}(E)$ in a simple form involving $\tilde{E}$. This gives the following useful approximate result for the number of Planck cells accessible to the wedge billiard at the scaled energy $\tilde{E}$:

$$N_{\mathrm{P}}(\tilde{E}) \approx \left(\frac{32}{3\pi\sin\phi\cos\phi}\right)^{\frac{1}{2}}\tilde{E}^{\frac{1}{2}}. \tag{19}$$

We shall see that the accuracy of our numerical results at the scaled energy $\tilde{E}$ depends on the ratio $N/N_{\mathrm{P}}(\tilde{E})$, where N is the number of cells on the PSS (or the dimension of the T-matrix) used in the calculation.

2.3.1. The problem of caustics close to the PSS. In the wedge billiard system a computational problem arises whenever a classical trajectory has a caustic close to the final point of the trajectory on the PSS. (This problem does not occur in force-free billiard systems like the circle billiard or the stadium billiard, since there are no caustics in such systems when the PSS is chosen to be the entire billiard boundary.) Consider a trajectory from q' to q'' on the PSS as in figure 3. If a caustic happens to occur precisely at q'', the second derivative of the action, $\partial^2 S(q'', q'; E)/\partial q''\partial q'$, will be infinite at that point. When this occurs, the two T-trajectories in figure 3 coalesce, reaching their highest point precisely at q''. A similar merging occurs for the V-trajectories at a higher energy. From (1) and (2), a matrix element of the transfer operator connecting q' to q'' will be infinite in this situation.

Now consider what happens if we calculate $|\det[1-T(\tilde{E})]|$ or the functional determinant $D(\tilde{E})$ as the energy is gradually increased. When E is small, the classical trajectories are confined to a few cells on the PSS near the wedge vertex. However, as E is increased in small increments, the billiard is able to go higher in the wedge and, as a result, more cells on the PSS gradually come into play. A matrix element $T_{mn}(E)$, involving classical trajectories from the cell centred on r_m to the cell centred on r_n along the tilted wall of the wedge, will first become nonzero when the energy E exceeds $r_n\cos\phi$ and, for the first time, is sufficient to make possible a classical trajectory from r_m to r_n. In this case, one or more caustics will lie close to the final point r_n of the two merged trajectories, and the resulting matrix element $T_{mn}(E)$ will be abnormally large. It is inevitable that this situation will occur many times as E is gradually increased from zero up to $E_{\max}$.

The effect of caustics may be clearly seen in figure 4(a) which shows the functional determinant $D(\tilde{E})$ as a function of $\tilde{E}$ calculated for the 49° wedge using a 25×25 T-matrix. ($E_{\max}$ was chosen to be 14.4 in units in which $m=\hbar=1$. This gives $N_{\mathrm{P}}(E_{\max})=25$ from (13).) A spiky appearance similar to figure 4(a) was found in many plots corresponding to different wedge angles and different dimensions of the T-matrix. In general, the relative size of the spikes was found to decrease as the dimension of the T-matrix was increased, leading one to surmise that the spikes might disappear completely in the limit of an infinitely large T-matrix.

We have found a method of calculating the T-matrix as a function of E which avoids the problem of caustics close to the PSS. The method makes use of the following scaling

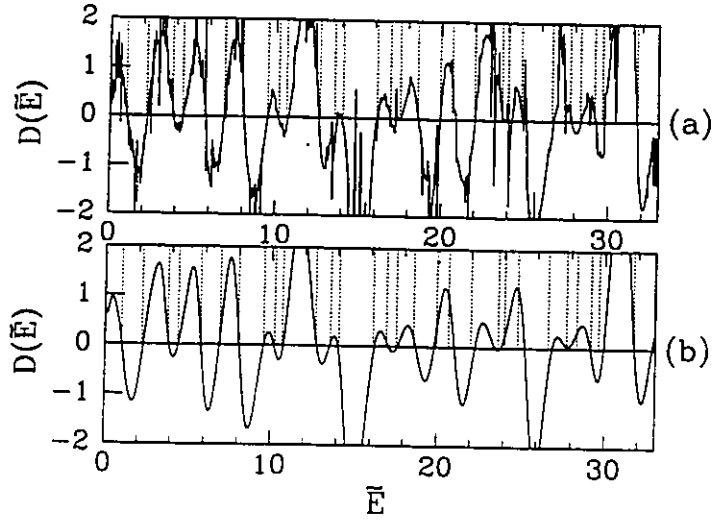

Figure 4. Plot of $D(\tilde{E})$ as a function of the scaled energy $\tilde{E}$ for the wedge billiard with $\phi = 49°$, calculated using a T-matrix of dimension 25. (*a*) calculated using cells with unchanging widths Δ_n; (*b*) calculated using the scaling method described in the text.

relations for the quantities entering the transfer operator, the powers being specific to the wedge billiard [24, 25]:

$$S(q_n, q_m; E) = E^{\frac{1}{2}} S(q_n, q_m; 1) \tag{20}$$

$$\frac{\partial^2 S(q_n, q_m; E)}{\partial q_n \partial q_m} = \frac{1}{E^{\frac{1}{2}}} \frac{\partial^2 S(q_n, q_m; 1)}{\partial q_n \partial q_m} \tag{21}$$

$$\nu(q_n, q_m; E) = \nu(q_n, q_m; 1) \tag{22}$$

Here the quantities on the right-hand side are calculated for $E = 1$. To begin with we set $E = 1$ and calculate the maximum distance along the tilted wall that can be reached by the billiard, namely, $r_{max} = 1/\cos\phi$. Having chosen the dimension N of the T-matrix, we then divide the interval from 0 to r_{max} into N cells having equal areas in phase space, as in figure 2. The classical trajectories joining the centres of any two given cells will not have caustics close to the PSS, except perhaps for trajectories reaching the highest cell on the PSS. (Even for this cell there does not seem to be a problem in the numerical calculations. This may be because this cell has the widest width Δ of all the cells and its centre is slightly displaced from r_{max}.) Thus, we calculate the elements of the T-matrix at $E = 1$ by the method described above, based on (1) and (2) and the Legendre transformation of (14) to (16). Our numerical calculations confirm that there are no unusually large matrix elements in the T-matrix. We can now obtain the T-matrix at any other energy E by scaling the widths of the cells according to $\Delta_n(E) = E\Delta_n(1)$ and making use of (2) and (20)–(22) to calculate $T_{mn}(E)$. A plot of the functional determinant $D(\tilde{E})$ against $\tilde{E}$ calculated in this way is shown in figure 4(*b*). The curve, which was calculated for the 49° wedge using a 25×25 T-matrix, is similar to that in figure 4(*a*) but is free of the irregularities due to caustics near the PSS.

In the following subsections we report the results of calculations of the semiclassical energy eigenvalues performed by scaling the T-matrix and the cells on the PSS in the manner just described, which we shall refer to as the *scaling method*. It should be pointed out that it represents a slight departure from Bogomolny's original conception in that the

scaling method alters the cell size each time the energy is changed. This results in there being many cells per de Broglie wave length (along the PSS in coordinate space) at the lowest energies and a lot fewer at the highest energies. Unfortunately, this means that one cannot characterize a given calculation by a parameter giving 'the number of cells along the PSS in coordinate space per de Broglie wave length'—the parameter b in the work of Boasman [17]. This seems to be the price that must be paid to circumvent the problem arising from caustics close to the PSS.

In assessing the numerical accuracy of the results presented below, we shall often quote values of the ratio $N/N_P(\tilde{E})$ instead of Boasman's b. ($N/N_P(\tilde{E}) = 1$ corresponds to $b = 2$.) The importance of this ratio in determining the accuracy of the semiclassical energy eigenvalues obtained by Bogomolny's method may be seen from figure 5. Using the

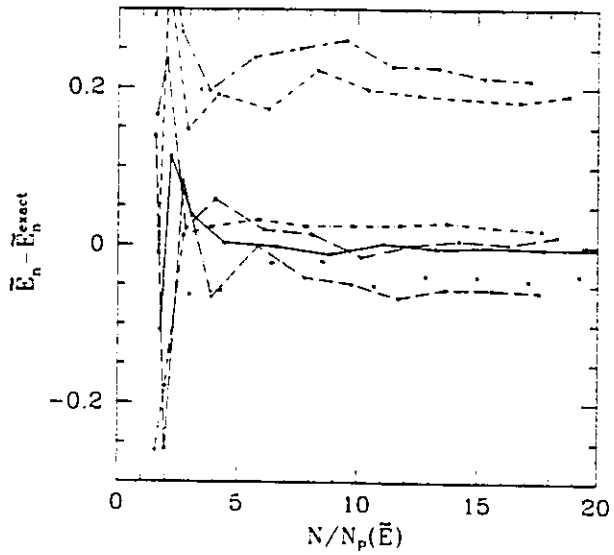

Figure 5. The differences $\tilde{E}_n - \tilde{E}_n^{\text{exact}}$ as a function of $N/N_P(\tilde{E})$ for the 49° wedge billiard. Solid curve, $\tilde{E}_{17}$; dotted curve, $\tilde{E}_{18}$; short-dash curve, $\tilde{E}_{19}$; long-dash curve, $\tilde{E}_{20}$; dot–short-dash curve, $\tilde{E}_{21}$; dot–long-dash curve, $\tilde{E}_{22}$; short-dash–long-dash curve, $\tilde{E}_{23}$.

49° wedge billiard as an example, we have plotted the differences $\tilde{E}_n - \tilde{E}_n^{\text{exact}}$ for the 17th to 23rd energy eigenvalues as a function of the ratio $N/N_P(\tilde{E})$. Here, the $\tilde{E}_n^{\text{exact}}$ are the exact scaled energy eigenvalues of the Schrödinger equation for the 49° wedge, and the $\tilde{E}_n$ are the scaled energy eigenvalues found from the zeros of the functional determinant $D(\tilde{E})$ using the scaling method described above. The calculations yielding these $\tilde{E}_n$ were performed using T-matrices ranging in dimension from 25 to 225. If, for example, a T-matrix of dimension N gave a particular value for, say, $\tilde{E}_{20}$, the corresponding value of $N/N_P(\tilde{E}_{20})$ was calculated using (19). It is clear from these plots that when $N/N_P(\tilde{E})$ is greater than about 10, the values of the $\tilde{E}_n$ have settled down to within about 4% of the mean spacing between the levels, in all the cases shown. This is a useful number to remember in looking at the results which follow. Similar results have been found by Boasman [17] for the Africa billiard ([17], figure 4.2; $b = 20$ corresponds to $N/N_P = 10$.) Boasman has also carried out calculations for the stadium billiard with $b = 10$ (equivalent to $N/N_P = 5$). Over the first 138 energy eigenvalues, the numerical uncertainty appears to fluctuate by about 10% of the mean level spacing ([17], figure 7.2). Our results for the relatively low-lying energy

eigenvalues shown in figure 5 are somewhat better than this at $N/N_P(\tilde{E}) = 5$.

We shall now present results for five different wedge angles, chosen to illustrate the cases of hard chaos, integrable behaviour and soft chaos in the classical dynamics.

2.3.2. Results for wedge angles giving hard chaos. We begin with the 49° wedge, which exemplifies the generic situation in the régime of hard chaos (a positive Lyapunov exponent for all initial conditions). Figure 6 shows the results for the functional determinant $D(\tilde{E})$ as a function of $\tilde{E}$ calculated by the scaling method for T-matrices of dimension 25 and 150. The dashed lines in the figure correspond to the positions of the exact energy eigenvalues of the 49° wedge obtained by solving the Schrödinger equation by matrix diagonalization [25]. It may be seen that the zeros of $D(\tilde{E})$ are close to the exact $\tilde{E}_n$ in both cases,

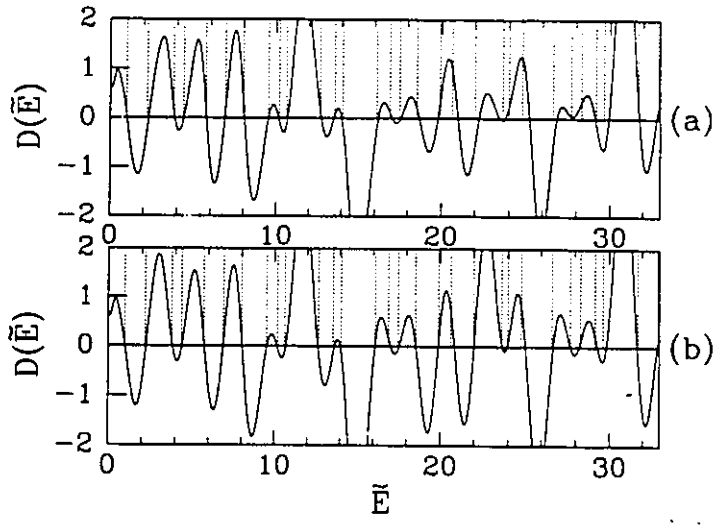

Figure 6. Plot of $D(\tilde{E})$ as a function of the scaled energy $\tilde{E}$ for the wedge billiard with $\phi = 49°$. (*a*) T-matrix of dimension 25; (*b*) T-matrix of dimension 150.

but the 150 × 150 T-matrix gives much better results at the higher energies shown in the figure. Note, for example, that the 25 × 25 T-matrix fails to give the zeros for the 25th and 26th eigenvalues, whereas the 150 × 150 T-matrix gives good numerical results for these energy eigenvalues. This improvement in accuracy is a consequence of the much larger number of cells on the PSS in the latter calculation, and the fact that the ratio N/N_P at this energy changes from about 2 to 11 as N goes from 25 to 150. (More precisely, for $\tilde{E} = 28$, equation (19) yields $N_P(\tilde{E}) \approx 13.9$, which gives $N/N_P \approx 1.8$ for $N = 25$ and $N/N_P \approx 10.8$ for $N = 150$. For the sake of comparison, at a lower scaled energy such as $\tilde{E} = 6$, the number of Planck cells is $N_P(\tilde{E}) \approx 6.4$, and thus the ratio N/N_P changes from about 4 to 24 as N goes from 25 to 150.)

Figure 7 shows plots for the 60° wedge billiard similar to those in figure 6. Here too the greatest improvement in numerical accuracy in going from $N = 25$ to $N = 150$ occurs at the highest energies shown in the figure. From (19), the number of Planck cells accessible to the system at scaled energy $\tilde{E} = 30$ is $N_P(\tilde{E}) \approx 15.3$. Thus, in going from $N = 25$ to $N = 150$, the ratio N/N_P changes from about 1.6 to 9.8.

How good are these numerical results compared with results from other semiclassical quantization schemes? To answer this question, a quantitative comparison of several

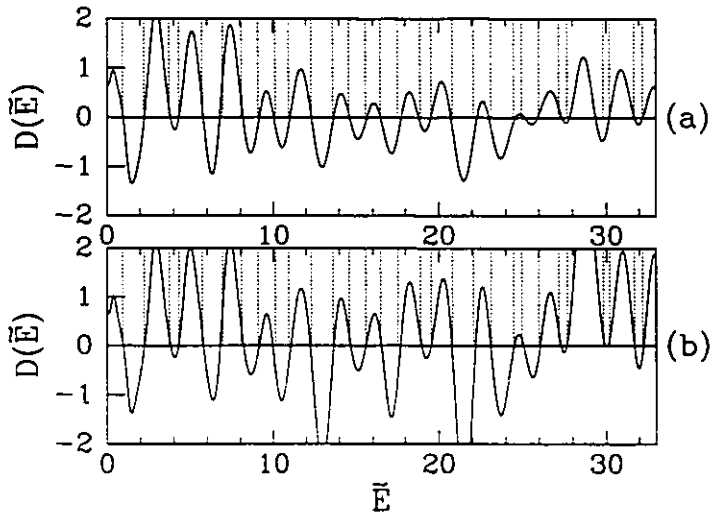

Figure 7. Plot of $D(\tilde{E})$ as a function of the scaled energy $\tilde{E}$ for the wedge billiard with $\phi = 60°$. (*a*) T-matrix of dimension 25; (*b*) T-matrix of dimension 150.

Table 1. Comparison of the mean deviation and the root-mean-square deviation of the calculated semiclassical energy eigenvalues E_n from the exact energy eigenvalues of the Schrödinger equation E_n^{exact}, for several different semiclassical quantization schemes. Results are given for the 49° and 60° wedge billiard systems. In each case, the averages were calculated over the lowest 30 energy eigenvalues. The values in parentheses give the number of primitive periodic orbits or pseudo orbits used in the calculations. Note that $\tilde{E} = Ed_{\text{TF}}(E)/3$.

wedge angle	quantization scheme	$< \tilde{E}_n - \tilde{E}_n^{\text{exact}} >$	$< (\tilde{E}_n - \tilde{E}_n^{\text{exact}})^2 >^{1/2}$
49°	staircase quantization (1048)	−0.284	0.215
49°	zeta product and func. rel. (1048)	0.029	0.113
49°	pseudo-orbit expansion and func. rel. (26706*)	0.046	0.126
49°	Berry-Keating erfc, K=50 (26706*)	0.028	0.142
49°	zeta product (16 irred. orbits) and func. rel.[a]	0.017	0.100
49°	$D(\tilde{E})$ from 150 × 150 T-matrix	0.027	0.081
60°	staircase quantization (1621)	−0.108	0.058
60°	zeta product and func. rel. (1621)	−0.031	0.040
60°	$D(\tilde{E})$ from 150 × 150 T-matrix	0.030	0.088

* All pseudo-orbits with word length ⩽ 19.
[a] There are 16 irreducible orbits with word length ⩽ 16.

different calculations is shown in table 1. In each case we have calculated the mean deviation $< (\tilde{E}_n - \tilde{E}_n^{\text{exact}}) >$ and the root-mean-square deviation $< (\tilde{E}_n - \tilde{E}_n^{\text{exact}})^2 >^{1/2}$, calculated over the lowest 30 eigenvalues. Results are given for the 49° and 60° wedges. The results of the present work are listed as '$D(\tilde{E})$ from 150 × 150 T-matrix'. All the other results are taken from tables I and II of [25] where the various calculations are described in detail. The calculations listed as 'zeta product and func. rel.' and 'pseudo-orbit expansion and func. rel.' determined the semiclassical energy eigenvalues from

$$\text{Re}\{\exp[-i\pi N_{\text{TF}}(E)]\zeta_S(E)\} = 0, \tag{23}$$

Bogomolny's semiclassical quantization scheme

with the zeta function calculated in various ways. The calculation listed as 'Berry–Keating erfc, $K = 50$' was performed using the Berry–Keating smoothed version of the Riemann–Siegel lookalike equation [13], which gave good results for the positions of the first hundred energy eigenvalues of the 49° wedge. The staircase quantization scheme, proposed by Aurich and Steiner [30], determines the jth energy eigenvalue E_j from,

$$N_{\rm TF}(E_j) + N_{\rm osc}(E_j) = j - \tfrac{1}{2} \tag{24}$$

where $N_{\rm osc}(E)$ is calculated from the Gutzwiller periodic orbit sum. It gave good results for the 60° wedge, but failed to give unambiguous eigenvalues for the 49° wedge.

On the basis of the rms deviations in table 1, we see that for the 49° wedge, the present calculation employing a 150×150 T-matrix gives better results than the other quantization schemes. Almost as good are the results obtained with a zeta product over only 16 irreducible orbits (to be defined in section 3). For the 60° wedge, however, the present calculation does not give as good results as either the zeta product over 1621 primitive periodic orbits or the staircase quantization scheme.

2.3.3. The 45° wedge billiard. The 45° wedge billiard is an integrable system. This is easily seen by considering a billiard confined in a 90° wedge with a constant force acting along the bisector of the wedge. In this symmetric wedge, the motion of the billiard can be decomposed into two independent motions perpendicular to the walls of the wedge. Let us use X and Y to denote these two components of the motion. On putting $y = \frac{1}{\sqrt{2}}X + \frac{1}{\sqrt{2}}Y$ in the Hamiltonian, equation (12), the Schrödinger equation separates into two one-dimensional equations,

$$-\frac{1}{2}\frac{{\rm d}^2\psi(X)}{{\rm d}X^2} + \frac{X}{\sqrt{2}}\psi(X) = E_X\psi(X) \tag{25}$$

$$-\frac{1}{2}\frac{{\rm d}^2\psi(Y)}{{\rm d}Y^2} + \frac{Y}{\sqrt{2}}\psi(Y) = E_Y\psi(Y). \tag{26}$$

With the boundary conditions that $\psi(X)$ and $\psi(Y)$ are zero along the appropriate walls of the wedge and that they also go to zero as X and Y approach infinity, these equations are those of the 'quantum bouncer', whose solutions are well known [31]. While the exact energy eigenvalues are given by the zeros of the Airy function ${\rm Ai}(-z)$, an excellent approximation to the eigenvalues, for all but the lowest two or three eigenvalues, is

$$E_n = \left[\frac{3\pi\hbar F}{2(2m)^{1/2}}\right]^{\frac{2}{3}}(n + \tfrac{3}{4})^{2/3} \tag{27}$$

where F is the strength of the constant force in the one-dimensional problem. The corresponding eigenfunctions ψ_n can also be written down [31]. Then the antisymmetric wavefunctions for the 90° wedge have the form,

$$\frac{1}{\sqrt{2}}[\psi_{n_1}(X)\psi_{n_2}(Y) - \psi_{n_2}(X)\psi_{n_1}(Y)], \tag{28}$$

which clearly vanishes along the bisector of the wedge (where $X = Y$). It follows that these antisymmetric combinations, with $n_1 \neq n_2$, are eigenfunctions of the desymmetrized 45° wedge, subject to the boundary condition that the wavefunction vanish along both walls of the wedge. The corresponding approximate energy eigenvalues are given by (putting $F = \frac{1}{\sqrt{2}}$ and $m = \hbar = 1$),

$$E_{n_1 n_2} = \left(\frac{3\pi}{4}\right)^{2/3}[(n_1 + \tfrac{3}{4})^{2/3} + (n_2 + \tfrac{3}{4})^{2/3}] \qquad n_1 > n_2. \tag{29}$$

T Szeredi et al

This expression allows us to locate, with sufficient accuracy, the positions of the exact energy eigenvalues of the Schrödinger equation of the 45° wedge.

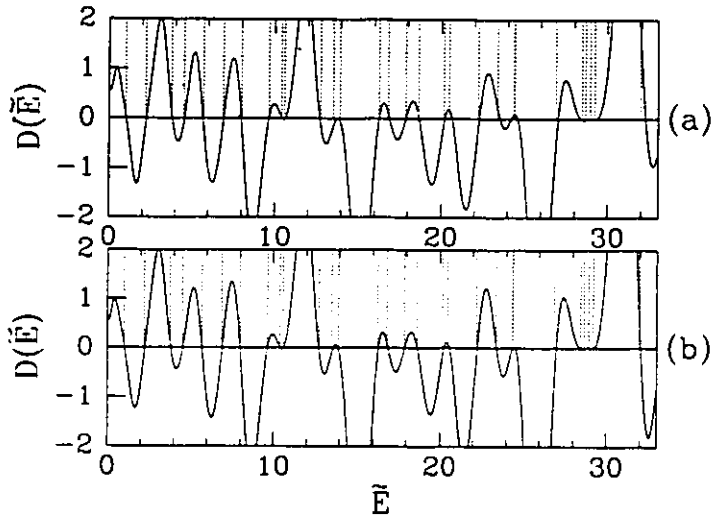

Figure 8. Plot of $D(\tilde{E})$ as a function of the scaled energy $\tilde{E}$ for the wedge billiard with $\phi = 45°$. (*a*) T-matrix of dimension 25; (*b*) T-matrix of dimension 150.

Figure 8 shows plots of the functional determinant $D(\tilde{E})$ against $\tilde{E}$ for the 45° wedge, the upper plot being for a 25×25 T-matrix, the lower for a 150×150 T-matrix. The dashed lines indicate the positions of the exact scaled energy eigenvalues calculated from (29) and (18). Just as for the 49° and 60° wedges, the lower energy eigenvalues are accurately determined by both calculations, but there is a noticeable improvement in the results at higher energies in going from $N = 25$ to $N = 150$. For example, the nearly degenerate pair of eigenvalues $\tilde{E}_{22}$ and $\tilde{E}_{23}$ are too widely separated in figure 8(*a*), but are much closer together in figure 8(*b*). There is also a slight improvement in the cluster of eigenvalues $\tilde{E}_{25}$ to $\tilde{E}_{28}$. (For $\tilde{E} = 30$, $N_P(\tilde{E}) \approx 14.3$ from (19), giving $N/N_P \approx 2$ for $N = 25$ and $N/N_P \approx 11$ for $N = 150$.)

It is interesting to note that Bogomolny's method for calculating semiclassical energy eigenvalues seems to be blissfully unaware of the profound formal differences between integrable and nonintegrable systems. The calculations just described for the 45° wedge proceeded in exactly the same way as those described earlier for the 49° and 60° wedges. This observation led us to try doing similar calculations for wedge angles corresponding to soft chaos or mixed behaviour in the classical system.

2.3.4. Results for wedge angles giving soft chaos. When the wedge angle ϕ is less than 45° the system exhibits both regular and chaotic motion [20–22, 27]. For angles close to 45° some of the invariant tori of the integrable case survive and show themselves as 'islands' or 'invariant curves' in a suitably chosen Poincaré surface of section. In other parts of the phase space, where invariant tori have been destroyed, the motion of the billiard is chaotic. For a sufficiently small departure from 45° this mixed behaviour can be understood on the basis of the well-known theorem due to Kolmogorov, Arnold and Moser (see, for example, the article by Berry [32]). However, at the wedge angles we have chosen to study, the KAM theorem almost certainly does not apply. Therefore, rather than use the term 'KAM

Bogomolny's semiclassical quantization scheme

régime', we shall refer to systems with $\phi \leqslant 45°$ as belonging to the régime of soft chaos or mixed behaviour.

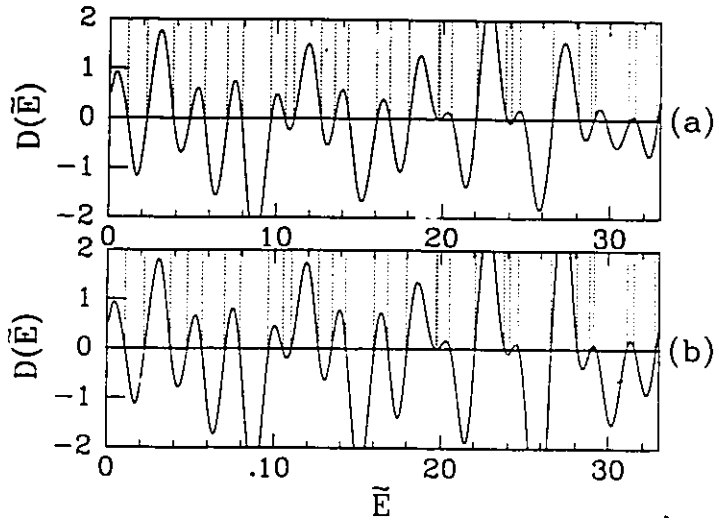

Figure 9. Plot of $D(\tilde{E})$ as a function of the scaled energy $\tilde{E}$ for the wedge billiard with $\phi = 41°$. (*a*) T-matrix of dimension 25; (*b*) T-matrix of dimension 150.

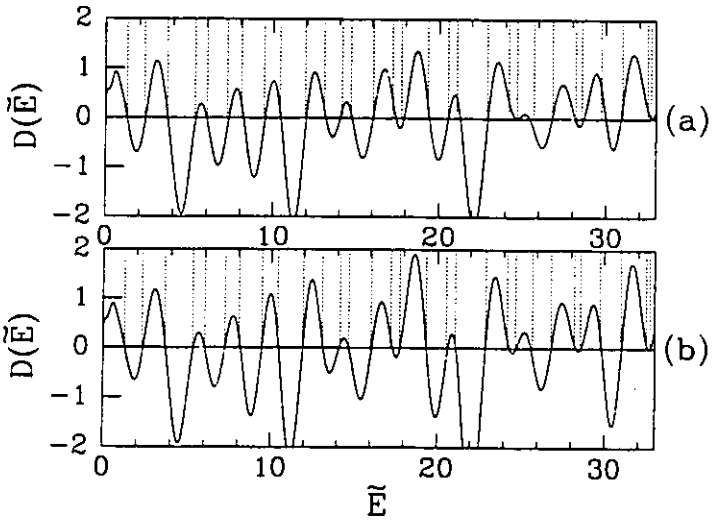

Figure 10. Plot of $D(\tilde{E})$ as a function of the scaled energy $\tilde{E}$ for the wedge billiard with $\phi = 30°$. (*a*) T-matrix of dimension 25; (*b*) T-matrix of dimension 150.

It is interesting to see whether Bogomolny's theory yields good results for the energy eigenvalues of the wedge billiard in the mixed régime. Figures 9 and 10 show results for the functional determinant $D(\tilde{E})$ as a function of $\tilde{E}$ for the 41° and 30° wedges, respectively. In both figures the dashed lines correspond to the exact energy eigenvalues obtained by solving the Schrödinger equation by matrix diagonalization. The pattern of the results is similar to that already described in figures 6 –8: at the higher energies shown, there is considerable improvement in the agreement between the zeros of $D(\tilde{E})$ and the exact quantum energy

eigenvalues in going from $N = 25$ to $N = 150$. For example, in the case of the 30° wedge, the 25×25 T-matrix fails to obtain the 21st and 22nd energy eigenvalues, but these are accurately determined by the 150×150 T-matrix. (For this case, when $\tilde{E} = 24$, $N_P(\tilde{E}) \approx 13.7$ from (19), giving $N/N_P \approx 2$ for $N = 25$ and $N = N_P \approx 11$ for $N = 150$.) Table 2 shows all our results for the five different wedge billiard systems studied in this

Table 2. Comparison between the scaled semiclassical energy eigenvalues $\tilde{E}_n$, calculated from the zeroes of the functional determinant $D(\tilde{E})$, and the exact scaled eigenvalues $\tilde{E}_n^{\text{exact}}$ of the Schrödinger equation, for different wedge angles. The averages were calculated for the number of energy eigenvalues shown in the last column.

wedge angle	T-matrix dimension	figure	$< (\tilde{E}_n - \tilde{E}_n^{\text{exact}}) >$	$< (\tilde{E}_n - \tilde{E}_n^{\text{exact}})^2 >^{1/2}$	number of eigenvalues
60°	25	6(a)	0.028	0.133	30
60°	150	6(b)	0.030	0.088	30
49°	25	5(a)	0.046	0.154	24
49°	150	5(b)	0.027	0.081	30
45°	25	7(a)	0.029	0.093	26
45°	150	7(b)	0.033	0.057	30
41°	25	8(a)	0.058	0.137	30
41°	150	8(b)	0.029	0.055	30
30°	25	9(a)	0.058	0.098	20
30°	150	9(b)	0.029	0.056	30

paper. In each case, the scaled semiclassical energy eigenvalues $\tilde{E}_n$ were determined from the zeros of the functional determinant $D(\tilde{E})$. In the table we list the values of the mean deviation $< (\tilde{E}_n - \tilde{E}_n^{\text{exact}}) >$ and the root-mean-square deviation $< (\tilde{E}_n - \tilde{E}_n^{\text{exact}})^2 >^{1/2}$ of the $\tilde{E}_n$ from the exact energy eigenvalues of the Schrödinger equation $\tilde{E}_n^{\text{exact}}$, calculated over the lowest 30 eigenvalues (or fewer if the quantization scheme failed to give all 30 eigenvalues—see the last column of the table). For each angle, results are given for T-matrices of dimension 25 and 150. Remarkably, the rms deviations for the 150×150 T-matrices are smaller for the 41° and 30° wedges than for any other entries in the table.

Evidently, the mixed regime presents no great challenge to the transfer operator approach, in contrast to quantization schemes based on the Gutzwiller trace formula and the dynamical zeta function. This conclusion is supported by the recent studies of a smooth nonscalable potential (the Nelson potential) carried out by Haggerty [6]. Instead of calculating energy eigenvalues, Haggerty determined the eigenstates of the variable $1/\hbar$ at two fixed energies, the lower one corresponding to classical motion that is mostly regular, the higher one to classical motion that is mostly chaotic. In both cases he found excellent agreement between the exact quantum results and the values calculated by means of Bogomolny's transfer operator.

Bogomolny's semiclassical quantization scheme

2.4. Periodic orbits from traces of T^m

It is interesting to see how the periodic orbits of the system can be obtained from the transfer operator formalism. The key to doing this is the relation (see [1, section 6]),

$$\ln \zeta_S(E) = -\sum_{\gamma}\sum_{n=1}^{\infty} \frac{\exp[in(S_\gamma/\hbar - \nu_\gamma \pi/2)]}{n[\det(M_\gamma - 1)]^{1/2}} = -\sum_{m=1}^{\infty} \frac{1}{m}\mathrm{Tr}(T^m). \qquad (30)$$

Here $\zeta_S(E)$ is the Selberg zeta function or dynamical zeta function, which can be expressed as an infinite product over the periodic orbits of the system, as in (6). The first sum in (30) is over the primitive periodic orbits of the system, labelled by γ, with S_γ the action, M_γ the monodromy matrix and ν_γ the Maslov index of the primitive periodic orbit γ. The sum over n counts the number of traversals of a given primitive periodic orbit. Finally, in the sum over m, the trace of T^m is nonzero only when there is a sequence of m mappings which starts and ends in the same cell of the PSS. In order that these m segments make up a periodic orbit, the trajectories must join smoothly at each crossing and the initial momentum must be equal to the final momentum. How this is achieved will be described presently.

The periodic orbits are obtained by calculating the Fourier transform of (30). Since the actions of the wedge billiard scale with energy according to [23, 25] $S_\gamma(E) = S_\gamma(1)E^{3/2}$, we put $u = E^{3/2}$ and define the Fourier transform of $\mathrm{Tr}(T^m)$ to be,

$$F_m(\omega) = \int_0^{u_{\max}} \mathrm{Tr}(T^m)\exp(-i\omega u)\mathrm{d}u. \qquad (31)$$

We have previously reported [5] the results of calculations of $F_m(\omega)$ for the first four traces for the 49° wedge, employing a T-matrix calculated using a fixed division of the PSS into cells of equal width Δ. Peaks in the Fourier transforms were found to occur at the actions of the shortest periodic orbits and their multiple traversals. Here, in figure 11, we show

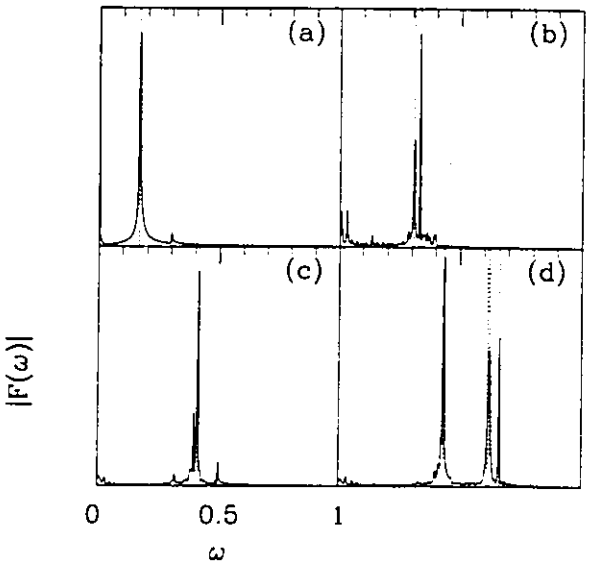

Figure 11. Results for the 49° wedge of the Fourier transforms of $\mathrm{Tr}(T^m)$ calculated from (31). The T-matrix used was 200 × 200. (*a*) $F_1(\omega)$; (*b*) $F_2(\omega)$; (*c*) $F_3(\omega)$; (*d*) $F_4(\omega)$.

similar results for the 49° wedge calculated from a 200 × 200 T-matrix constructed using the scaling method. The 200 cells of the PSS extended from the vertex out to $r_{\max} = 61.4$

T Szeredi et al

along the tilted wall, and the integrand in (31) was computed at 512 equally-spaced points extending out to $u_{max} = (40.3)^{3/2} = 256$. The vertical dashed lines in figure 11 lie at the positions $S_\gamma(1)$ of the shortest periodic orbits of the 49° wedge. (See [24], table II, for the actions of these orbits and their labels.) It is satisfying to see that $F_1(\omega)$ has a single peak at the action of the V orbit, while $F_2(\omega)$ has peaks at the actions of the orbits TV and V^2. Furthermore, $F_3(\omega)$ has peaks at the actions of the orbits TVV and V^3, and $F_4(\omega)$ has peaks at the actions of $TTVV$, $(TV)^2$, $TVVV$ and V^4, in order of increasing actions.

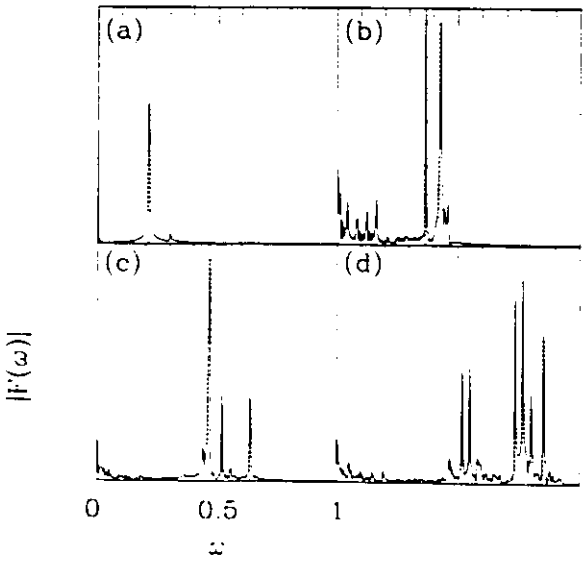

Figure 12. Results for the 60° wedge of the Fourier transforms of $\mathrm{Tr}(T^m)$ calculated from (31). The T-matrix used was 300 × 300. (*a*) $F_1(\omega)$; (*b*) $F_2(\omega)$; (*c*) $F_3(\omega)$; (*d*) $F_4(\omega)$.

Figure 12 shows similar calculations of the Fourier transforms of the traces of T^m for the 60° wedge, calculated from a 300 × 300 T-matrix. For those peaks which we can identify with the actions of periodic orbits, indicated by the vertical dashed lines, the agreement is excellent. However, there are two mysterious peaks in figure 12(*d*), one just above the first dashed line ($TTTV$) the other just above the third dashed line ($TVVV$). Unlike the other unidentified peaks in figure 12(*b*) and (*d*), which diminish or shift their positions when the dimension of the T-matrix is increased from 200 to 300, these two mysterious peaks in $F_4(\omega)$ remain fixed in position and actually increase in intensity. This suggests that they have a physical origin, presently unknown. However, we believe that all the other unidentified peaks in figure 12(*b*) and (*d*) are caused by the numerical procedures.

Figure 13 shows similar calculations of the Fourier transforms $F_m(\omega)$ for the 45° wedge, calculated from a 200 × 200 T-matrix. The vertical dashed lines in the figure indicate the positions of the actions of periodic orbits lying on invariant tori (except for the V orbit which is isolated). These actions are readily calculated analytically for the 90° wedge by requiring that the ratio of the periods of the two independent motions be equal to a rational fraction. They are given by the formula (in units of $\hbar$),

$$S(\mu_1, \mu_2, k) = \frac{8}{3} k \frac{\mu_1 \mu_2}{(\mu_1^2 + \mu_2^2)^{1/2}} \tag{32}$$

where μ_1 and μ_2 are mutually prime positive integers, and $k = 1, 2, \ldots, \infty$. This expression also comes from the theory of Berry and Tabor [33, 34] for integrable systems, adapted to

Bogomolny's semiclassical quantization scheme

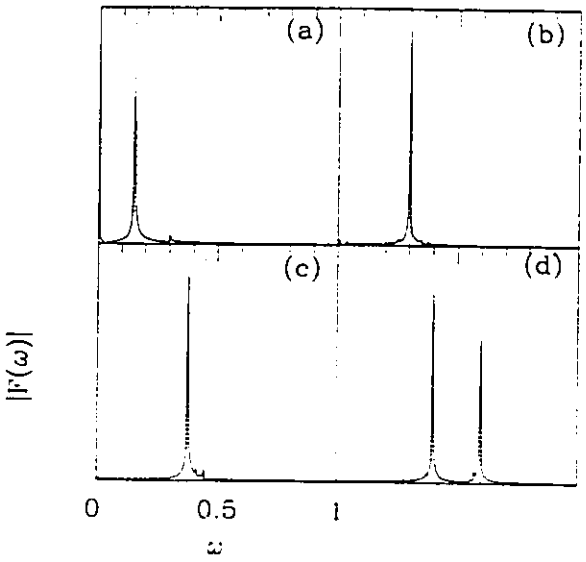

Figure 13. Results for the 45° wedge of the Fourier transforms of $\mathrm{Tr}(T^m)$ calculated from (31). The T-matrix used was 200×200. (*a*) $F_1(\omega)$. The peak lies at half the action $S(1, 1, 1)$ for the 90° wedge given by (32). (*b*) $F_2(\omega)$. The peak is at $S(1, 1, 1)$. (*c*) $F_3(\omega)$. The large peak is at $S(2, 1, 1)$. A very small peak occurs at $(3/2)S(1, 1, 1)$. (*d*) $F_4(\omega)$. The peaks lie at $S(3, 1, 1)$ and $S(1, 1, 2)$.

the case of the 90° symmetric wedge billiard. Each permissible choice of μ_1, μ_2 and k corresponds to a continuous family of periodic orbits on a torus. Figure 13 shows that in this integrable case we again find excellent agreement between the positions of the peaks in the Fourier transforms $F_m(\omega)$ and the actions of periodic orbits obtained from (32). The other integrable system studied in this paper, the circle billiard, was likewise found to give peaks in the $F_m(\omega)$ at precisely the actions of the periodic orbits of the circle, which are easily evaluated analytically.

To complete the picture we show in figures 14 and 15 the Fourier transforms $F_m(\omega)$ for the 41° and 30° wedges, calculated in each case using a 200×200 T-matrix constructed by the scaling method. In both figures there is excellent agreement between the positions of the peaks and the actions of the lowest periodic orbits, indicated by the dashed lines.

We return to the question of how the trace calculations pick out only the classical periodic orbits among all the joined trajectories. Let us consider the simplest case, $\mathrm{Tr}(T) = \sum T_{ii}$. From (1) this sum is approximately equal to the integral,

$$\sum_{\text{cl.tr.}} \frac{1}{(2\pi i\hbar)^{1/2}} \int_\Sigma \mathrm{d}q \left| \frac{\partial^2 S(q'', q'; E)}{\partial q'' \partial q'} \right|^{\frac{1}{2}}_{q''=q'=q} \exp\left[\frac{\mathrm{i}}{\hbar} S(q'', q'; E)_{q''=q'=q} - \mathrm{i}\nu \frac{\pi}{2} \right] \tag{33}$$

where Σ on the integral indicates the PSS and the sum is over all classical trajectories that return to the same position on the PSS after one crossing. We now expand $S(q'', q'; E)$ about a point q on the PSS and evaluate the integral in the stationary phase approximation. The stationary phase condition is

$$\frac{\partial S(q'', q'; E)}{\partial q''} + \frac{\partial S(q'', q'; E)}{\partial q'} = 0 \tag{34}$$

T Szeredi et al

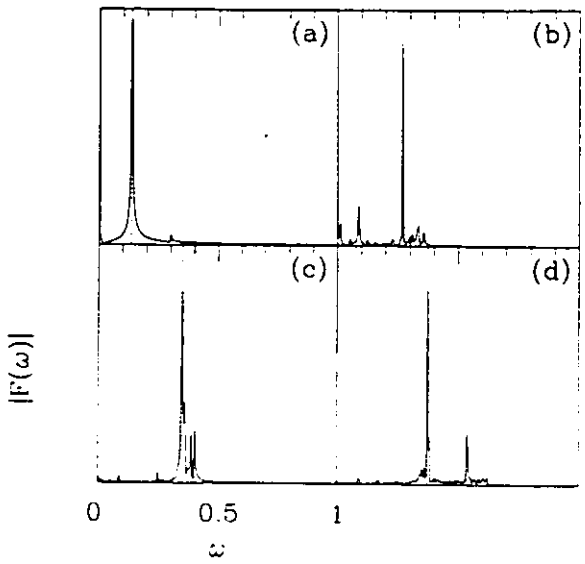

Figure 14. Results for the 41° wedge of the Fourier transforms of $\mathrm{Tr}(T^m)$ calculated from (31). The T-matrix used was 200 × 200. (*a*) $F_1(\omega)$; (*b*) $F_2(\omega)$; (*c*) $F_3(\omega)$; (*d*) $F_4(\omega)$.

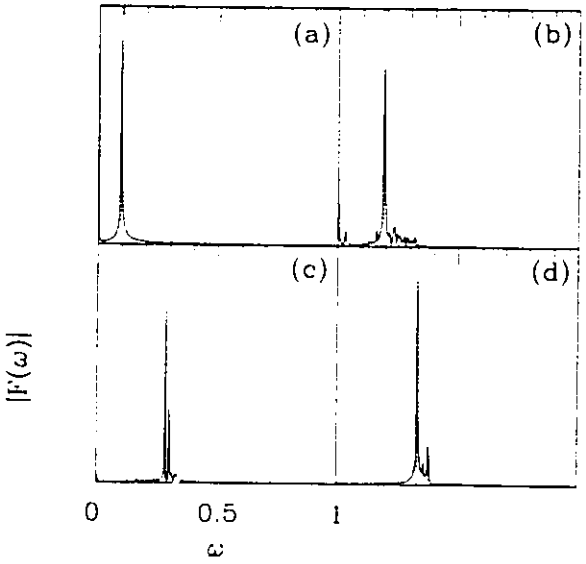

Figure 15. Results for the 30° wedge of the Fourier transforms of $\mathrm{Tr}(T^m)$ calculated from (31). The T-matrix used was 200 × 200. (*a*) $F_1(\omega)$; (*b*) $F_2(\omega)$; (*c*) $F_3(\omega)$; (*d*) $F_4(\omega)$.

where the derivatives are evaluated at $q'' = q' = q$. This condition, which we assume is satisfied at a single point $\bar{q}$, is equivalent to $p'' - p' = 0$ at the point $q = \bar{q}$. Defining

$$\varpi = \frac{1}{2}\left(\frac{\partial^2 S(q'', q'; E)}{\partial q''^2} + 2\frac{\partial^2 S(q'', q'; E)}{\partial q'' \partial q'} + \frac{\partial^2 S(q'', q'; E)}{\partial q'^2}\right) \tag{35}$$

Bogomolny's semiclassical quantization scheme

where the derivatives are evaluated at the point $q'' = q' = \bar{q}$, and using the fact that,

$$\int_{-\infty}^{\infty} \exp\left[\mathrm{i}\frac{\Xi}{\hbar}(q-\bar{q})^2\right]\mathrm{d}q = \left(\frac{\pi\mathrm{i}\hbar}{|\Xi|}\right)^{\frac{1}{2}} \exp[-\mathrm{i}\nu_\Xi\pi/2] \tag{36}$$

where $\nu_\Xi = 0$ for $\Xi > 0$ and $\nu_\Xi = 1$ for $\Xi < 0$, we obtain,

$$\mathrm{Tr}(T) \approx \sum_\gamma \frac{1}{|2\Xi|^{\frac{1}{2}}} \left|\frac{\partial S_\gamma(q'', q'; E)}{\partial q''\partial q'}\right|^{\frac{1}{2}}_{q''=q'=\bar{q}} \exp\left[\frac{\mathrm{i}}{\hbar}S_\gamma(q'', q'; E)_{q''=q'=\bar{q}} - \mathrm{i}(\nu+\nu_\Xi)\frac{\pi}{2}\right]. \tag{37}$$

The sum is now over periodic orbits which cross the PSS just once, and the factor in front of the exponential is exactly the same as in Gutzwiller's derivation of the trace formula [7, 8]. Thus, it can be replaced by $[\det(M_\gamma - 1)]^{-1/2}$ where M_γ is the monodromy matrix for the periodic orbit passing through $\bar{q}$. By comparing with (30) we see that the Maslov index for the periodic orbit is $\nu_\gamma = \nu + \nu_\Xi$, which is exactly the same as Gutzwiller's result. Of course, for a finite T-matrix, $\mathrm{Tr}(T) = \sum T_{ii}$ will be an approximation to this result. A similar demonstration of how the trace operation yields the contribution ν_Ξ to the Maslov index has also been given by Boasman [17].

The extension of the preceding calculation to $\mathrm{Tr}(T^2)$ and traces of higher powers of T is relatively straightforward [17]. Each multiplication of the finite T-matrices is approximated by an integral over the PSS, which can be evaluated by the stationary phase method. (See [1, (A1.15)–(A1.21)].) The stationary phase condition at each intermediate crossing of the PSS ensures that the classical trajectories will join up smoothly at the crossings.

2.5. Finite approximations to the transfer operator and the dynamical zeta function

The formal relation $\zeta_S(E) = \det[1 - T(E)]$ was introduced in (5). Since we have been investigating finite approximations to the transfer operator, the question arises as to what they imply for finite approximations to the dynamical zeta function. In this subsection we explore this connection.

For a system with two freedoms displaying hard chaos, a finite approximation to $\zeta_S(E)$ can be obtained by retaining only a finite number of primitive periodic orbits in the product over γ in (6). Alternatively, the infinite product can be expanded in a Dirichlet series and the expansion truncated at some point [11–14]. In this case the expansion has the form,

$$\zeta_S(E) = 1 + \sum_{n=1}^{N} C_n(E). \tag{38}$$

Here, the sum is over *pseudo orbits*—linear combinations of primitive periodic orbits with energy E, including repetitions, and ordered according to increasing *pseudoaction* or increasing *word length* (when there is a suitable symbolic dynamics for the system). In the present discussion we shall assume that there is a symbolic dynamics such that the number of symbols characterizing a pseudo orbit (the word length) is the same as the number of crossings of the PSS, as is the case for the 49° wedge billiard with the PSS along the tilted wall of the wedge. Then $C_n(E)$ is the contribution to the sum from all pseudo orbits of word length n.

In the present section we have been considering a finite approximation to the transfer operator based on introducing N suitably chosen cells along the PSS in coordinate space. This naturally leads to the following expansion:

$$\det[1 - T(E)] = \varepsilon_{\alpha\beta\ldots\nu}(\delta_{1\alpha} - T_{1\alpha})(\delta_{2\beta} - T_{2\beta})\ldots(\delta_{N\nu} - T_{N\nu}) = 1 + \sum_{n=1}^{N} A_n(E) \tag{39}$$

T Szeredi et al

where $\varepsilon_{\alpha\beta\ldots\nu}$ is the antisymmetric tensor of order N and summations are implied over the repeated indices. The coefficient $A_n(E)$ can be expressed as the sum over all possible n-dimensional determinants that can be formed by choosing n columns and the corresponding n rows out of the $N \times N$ T-matrix. It can be interpreted as being the contribution from those trajectories which cross the PSS exactly n times. Because of the determinantal form of each term contributing to $A_n(E)$, the only nonzero contributions are from trajectories that do not pass more than once through any cell on the PSS.

Bogomolny argues that since the trajectories which cross the PSS N times or less are the only ones contributing to the right-hand side of (39), it is plausible that the only nonzero contributions to the pseudo orbit expansion at energy E in (38) come from pseudo orbits which cross the PSS N times or less, i.e. from pseudo orbits having word length $n \leqslant N$. This would mean that all the $C_n(E)$ for $n \geqslant N$ sum to zero in (38), or that $C_n(E) = 0$ for every $n > N$. It is this latter possibility which Bogomolny considers (see [1, section 9]) and which we investigate here for the 49° wedge billiard.

In previous work on the 49° wedge billiard [25] we calculated all pseudo orbits with word length $n \leqslant 19$. It is, therefore, an easy matter to calculate each $C_n(E)$ in (38) as a function of E for n up to 19. If there is a correspondence between the behaviour of $A_n(E)$ in (39) and $C_n(E)$ in the pseudo orbit expansion, then at low energies only orbits with small n should contribute, and, as E increases, pseudo orbits with longer word length should begin to contribute. This 'cut-in' behaviour conjectured to occur in $C_n(E)$ is a natural consequence of the dynamics. (It is not the same as the 'smoothed' cut-in behaviour described by the complementary error function in the theory of Berry and Keating [13].)

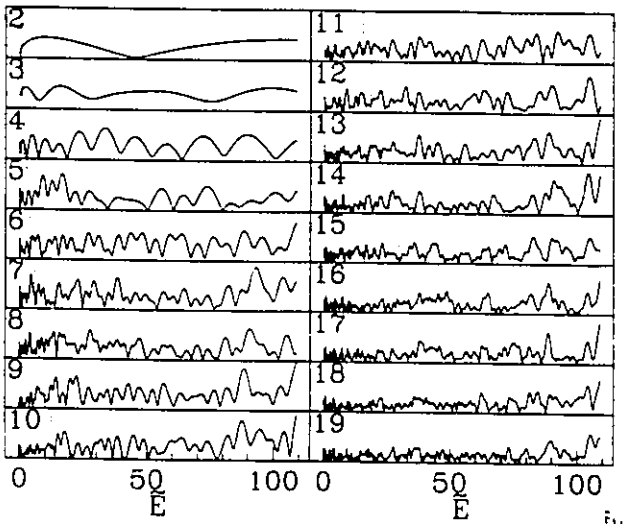

Figure 16. Plots of $|C_n(\tilde{E})|$ against $\tilde{E}$ for the 49° wedge. $C_n(E)$ is the contribution to the dynamical zeta function from pseudo orbits in the theory of Berry and Keating [11] which collide n times with the tilted wall. The value of n is given to the left of each plot. The dashed line is the position of $\tilde{E}^*$.

In figure 16 we plot the first 19 contributions $|C_n(E)|$ to the pseudo orbit expansion, equation (38), for the 49° wedge billiard. Plotted as a vertical dashed line for each value of n is

$$E^* = \left(\frac{3\pi\hbar\cos\phi}{2\sqrt{2}}\right)^{\frac{2}{3}} n^{\frac{2}{3}} \tag{40}$$

Bogomolny's semiclassical quantization scheme

as given by (13), with $N_P(E)$ set equal to n. Over the energy range of the calculations it is not obvious that there is a natural cut-in of the contributions from pseudo orbits of increasing word length. If there *is* a cut-in, it is certainly not sharp.

3. The transfer operator and symbolic dynamics

When any classical trajectory of a given system can be labelled by a sequence of symbols, drawn from a suitable alphabet, it is possible to construct a completely different partition of the PSS into cells in phase space. The corresponding transfer operator has a somewhat different appearance (see [1, (10.14)]). It is interesting to explore the consequences of this approach and assess the accuracy of the semiclassical energy eigenvalues to which it leads.

Trajectories of the wedge billiard are characterized by sequences of two symbols, which we denote as T and V. With the PSS chosen to be along the tilted wall of the wedge, any classical trajectory can be divided into segments, each consisting of a mapping from one point on the PSS to another. Each segment can be assigned a symbol, T or V, according as the mapping is a T-mapping or a V-mapping. In our earlier work on the wedge billiard [23, 24] we found that for wedge angles greater than 45°, every periodic orbit of the system corresponds to a sequence of Ts and Vs which is unique, apart from cyclic permutations of the symbols. On the other hand, not every sequence of n symbols corresponds to an actual periodic orbit of the system: some sequences are *pruned* by the dynamics of the system [35, 18]. For example, if parentheses are used to enclose a sequence of symbols which repeats indefinitely, corresponding to a periodic orbit, then the sequence (T) does not correspond to an actual periodic orbit for any wedge angle (other than 90°) since the billiard must eventually collide with the vertical wall. Another example is that there is no periodic orbit (TTV) for the 49° wedge, although such a periodic orbit does exist for the 60° wedge. For a given system, one would like to discover the *pruning rules* specifying which orbits (periodic or otherwise) exist and which do not. While it may be possible to discover a few simple pruning rules, in general the number of such rules will be infinite.

When a binary code exists one can obtain a partition of the PSS by identifying phase-space cells with all possible sequences having a fixed number of symbols [1, 2]. As an illustration, consider the partition of the PSS derived from 2-symbol cells. Using the symbols T and V appropriate to the wedge billiard, we have four possible cells, denoted as TT, TV, VT and VV. (Alternatively, these could be labelled as 1, 2, 3 and 4.) Thus, for example, the periodic orbit $(TTVVTVV)$ passes successively through the cells TT, TV, VV, VT, TV, VV and VT, this sequence being repeated indefinitely. Figure 17 shows the PSS consisting of the tilted wall for the 49° wedge. The seven points on the diagram are located at the values of (r, p_r) corresponding to the seven collisions made by the billiard with the tilted wall while traversing the periodic orbit $(TTVVTVV)$. The PSS is shown divided into four cells, labelled according to the two mappings immediately following each collision. Thus, in our example, the two points located in the VT region have the property that the next collision with the tilted wall results from a V-mapping, while the collision after that results from a T-mapping. The boundaries between the cells were found by firing the billiard out of the wedge vertex at all possible angles, and determining the T or V nature of the two subsequent mappings in each case. It is noteworthy that the areas of the cells are not equal, although they are approximately so.

The same procedure is readily extended to 3-symbol cells, denoted by TTT, TTV, TVT, TVV, VTT, VTV, VVT and VVV. This leads to a partition of the PSS into eight approximately equal areas labelled by the T or V nature of the three mappings immediately following each collision. The extension of this procedure to 4-symbol cells is

T Szeredi et al

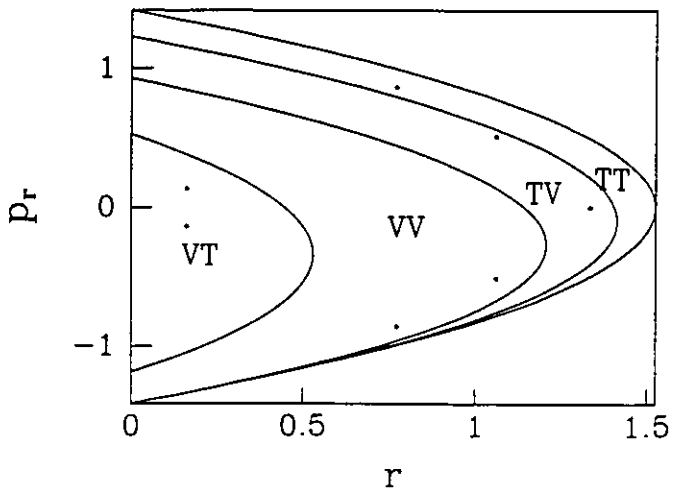

Figure 17. The PSS in the phase space (r, p_r) of the tilted wall of the 49° wedge. The PSS is divided into four cells labelled by the two mappings immediately following each collision. The points shown were generated by the periodic orbit $TTVVTVV$.

straightforward.

The resulting picture of the PSS for the 49° wedge, shown in figure 18, reveals an interesting feature. Instead of the expected 16 approximately equal areas, only 14 are found by the method of firing the billiard out of the wedge vertex and determining the four subsequent mappings. Cells labelled as $TTVT$ and $TVTT$ were not generated by this procedure. Furthermore, when the 1048 primitive periodic orbits having word length $n \leqslant 19$ of the 49° wedge were analysed into sequences of four symbols following each collision with the PSS, in a manner analogous to the example above for 2-symbol cells, it was found that the sequences $TTVT$ and $TVTT$ never occurred. We infer that the absence of these sequences constitutes two simple pruning rules for the 49° wedge.

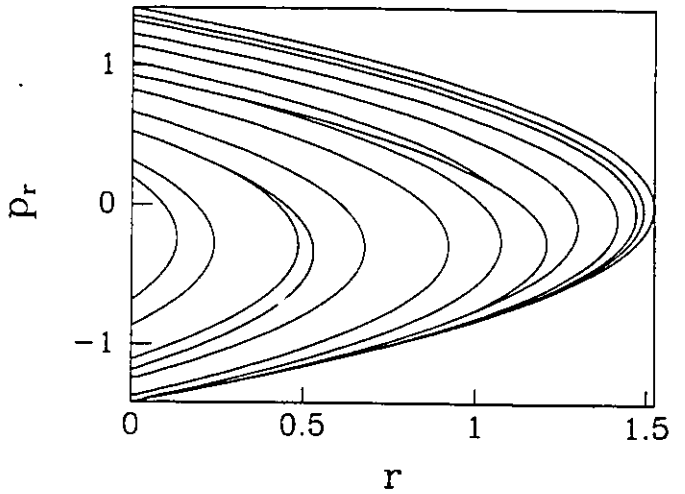

Figure 18. Partition of the PSS of the preceding figure into 4-symbol cells. Only 14 cells were generated by the procedure described in the text, the missing cells being $TTVT$ and $TVTT$.

Bogomolny's semiclassical quantization scheme

It should be possible to use this procedure to find additional pruning rules in a systematic way. We have not pursued this in great detail, but for 5-symbol cells we have found that there are 28 cells in the PSS of the 49° wedge, implying that there are no new pruning rules consisting of forbidden sequences of 5 symbols. For similar reasons, there are no new pruning rules consisting of forbidden sequences of 6 symbols. However, new pruning rules have been found to arise for sequences of 7, 8 and 9 symbols.

The division of a suitably chosen PSS into n-symbol cells provides a different way of calculating approximate semiclassical energy eigenvalues. In this case the elements of the T-matrix are constructed from the formula (see [1, (10.14)]),

$$T_{mk} = A_{mk} \exp[\mathrm{i}(S_{mk}/\hbar - \nu_{mk}\pi/2) - u_{mk}/2] \tag{41}$$

where $A_{mk} = 1$ if there is a group of classical trajectories beginning in cell m and ending in cell k, and is 0 otherwise. Here S_{mk} is the action, ν_{mk} is the phase index, and u_{mk} is the stability exponent of a representative classical trajectory from cell m to cell k. In the case of a partition of the PSS into n-symbol cells, the dimension of the T-matrix is 2^n. The semiclassical energy eigenvalues are to be found from,

$$\det[\delta_{mk} - T_{mk}(E)] = 0. \tag{42}$$

One way of calculating the matrix elements T_{mk} is to relate them to the properties of the periodic orbits of the system. For any of the wedge billiard systems we define

$$X_\gamma = \exp[\mathrm{i}S_\gamma(1)E^{3/2} - \mathrm{i}\nu_\gamma(1)\pi/2 - u_\gamma(1)/2] \tag{43}$$

where $S_\gamma(1)$, $\nu_\gamma(1)$ and $u_\gamma(1)$ are the action, Maslov index and stability exponent calculated for the primitive periodic orbit γ at $E = 1$. For the 49° and 60° wedge billiards these quantities have been calculated for more than one thousand primitive periodic orbits. (The values for the shortest primitive periodic orbits are given in tables I and II of [24].) Now, since any primitive periodic orbit labelled by n symbols is made up of n segments which go from the PSS back to the PSS, one can determine the initial and final cells for each segment and use a representative classical trajectory linking each pair of cells to calculate S_{mk}, ν_{mk} and u_{mk}. Thus, if a certain periodic trajectory corresponds to the sequence of symbols $(\sigma_1\sigma_2\ldots\sigma_n)$ where σ_i serves to label the ith cell, then we can make the approximations,

$$S_{\gamma=\sigma_1\sigma_2\ldots\sigma_n} \approx S_{\sigma_1\sigma_2} + S_{\sigma_2\sigma_3} + \ldots + S_{\sigma_n\sigma_1} \tag{44}$$

$$\nu_{\gamma=\sigma_1\sigma_2\ldots\sigma_n} \approx \nu_{\sigma_1\sigma_2} + \nu_{\sigma_2\sigma_3} + \ldots + \nu_{\sigma_n\sigma_1} \tag{45}$$

$$u_{\gamma=\sigma_1\sigma_2\ldots\sigma_n} \approx u_{\sigma_1\sigma_2} + u_{\sigma_2\sigma_3} + \ldots + u_{\sigma_n\sigma_1}. \tag{46}$$

It follows from (41)–(46) that,

$$X_{\gamma=\sigma_1\sigma_2\ldots\sigma_n} \approx T_{\sigma_1\sigma_2}T_{\sigma_2\sigma_3}\ldots T_{\sigma_n\sigma_1}. \tag{47}$$

This approximation can be expected to be good if the cells on the PSS are sufficiently small.

Bogomolny has described in some detail the situation corresponding to 2-symbol cells. (See [1], (10.32)–(10.37).) In this case the matrix element describing, for example, the trajectory going from cell TV to cell VV is denoted as T_{TVV}. The T-matrix has the form,

$$T(E) = \begin{pmatrix} T_{TTT} & T_{TTV} & 0 & 0 \\ 0 & 0 & T_{TVT} & T_{TVV} \\ T_{VTT} & T_{VTV} & 0 & 0 \\ 0 & 0 & T_{VVT} & T_{VVV} \end{pmatrix} \tag{48}$$

T Szeredi et al

When $\det[1 - T(E)]$ is expanded and set equal to zero, we obtain,

$$\begin{aligned}
&1 - T_{TTT} - T_{VVV} - (T_{TVT}T_{VTV} - T_{TTT}T_{VVV}) \\
&- (T_{VTV}T_{TVV}T_{VVT} - T_{TVT}T_{VTV}T_{VVV}) \\
&- (T_{TTV}T_{TVT}T_{VTT} - T_{TTT}T_{TVT}T_{VTV}) \\
&- (T_{TTV}T_{TVV}T_{VVT}T_{VTT} - T_{TTT}T_{TVV}T_{TVV}T_{VVT} \\
&- T_{TTV}T_{TVT}T_{VTT}T_{VVV} + T_{TTT}T_{VTV}T_{TVT}T_{VVV}) = 0. \qquad (49)
\end{aligned}$$

With the approximation of (47) we can now express this equation in terms of the X_γ's for the primitive periodic orbits. The result is

$$\begin{aligned}
1 - X_T - X_V - (X_{TV} - X_T X_V) - (X_{TVV} - X_{TV}X_V) - (X_{TTV} - X_T X_{TV}) \\
-(X_{TTVV} - X_T X_{TVV} - X_{TTV}X_V + X_T X_{TV} X_V) = 0. \qquad (50)
\end{aligned}$$

It is interesting to note that the left-hand side of this equation constitutes a *cycle expansion* of the kind introduced by Cvitanović and Eckhardt [35, 18], X_T and X_V being *fundamental cycles* and the terms enclosed in parentheses being *curvature corrections*, up to word length of 4. However, because each term in the expansion (49) of the determinant consists of a product of matrix elements in which there occurs one element from each row and one element from each column, the cycle expansion involves only *irreducible orbits*. These are defined by Bogomolny to be primitive periodic orbits which do not pass more than once through any cell of the PSS. Thus, (50) is the cycle expansion in irreducible orbits corresponding to the partition of the PSS into 2-symbol cells.

The lowest energy eigenvalues of the quantum system can be found from (50) using X_T, X_V, X_{TV}, X_{TVV}, X_{TTV} and X_{TTVV} calculated as a function of energy from the properties of the corresponding primitive periodic orbits. However, as was mentioned at the beginning of this section, the primitive periodic orbits (T) and (TTV) are pruned in the case of the 49° wedge. We therefore make the approximations,

$$X_T \approx \frac{X_{TTTVV}}{X_{TTVV}} \qquad X_{TTV} \approx \frac{X_{TTVV}X_{TV}}{X_{TVV}}. \qquad (51)$$

With these replacements in (50) we can now evaluate $|\det[1-T(\tilde{E})]|$ or, better, the functional determinant $D(\tilde{E})$, as a function of the scaled energy $\tilde{E}$. The result is shown in figure 19(a). The vertical dashed lines in figure 19 lie at the exact scaled energies $\tilde{E}_n^{\text{exact}}$. We see that the first two zeros of $D(\tilde{E})$ are close to the first two energy eigenvalues, but the curve fails to give the third and fourth energy eigenvalues, and also the ninth and tenth energy eigenvalues. These results are not unreasonable for a 4×4 T-matrix. (If the number of Planck cells is 4, equation (19) gives $\tilde{E} \approx 2.3$.)

A similar calculation can be carried out for the 8×8 T-matrix corresponding to 3-symbol cells. In this case there are 9 independent products of T elements to be estimated from the primitive periodic orbits. The resulting curve for $D(\tilde{E})$ against $\tilde{E}$ is shown in figure 19(b). Now the first eight zeros lie close to the exact scaled energy eigenvalues, but the curve misses the ninth and tenth eigenvalues. (When the number of Planck cells is 8, equation (19) gives $\tilde{E} \approx 9.3$.)

Figure 19(c) shows the curve for $D(\tilde{E})$ against $\tilde{E}$ for the 16×16 T-matrix corresponding to 4-symbol cells. In this case we used the properties of 19 primitive periodic orbits of the 49° wedge to estimate the unknown quantities in the expansion of the determinant. On the whole, the curve is not an improvement over that for 3-symbol cells, since it now misses the eighth and ninth eigenvalues. (When $N_P(\tilde{E}) = 16$, equation (19) gives $\tilde{E} \approx 37$.)

Bogomolny's semiclassical quantization scheme

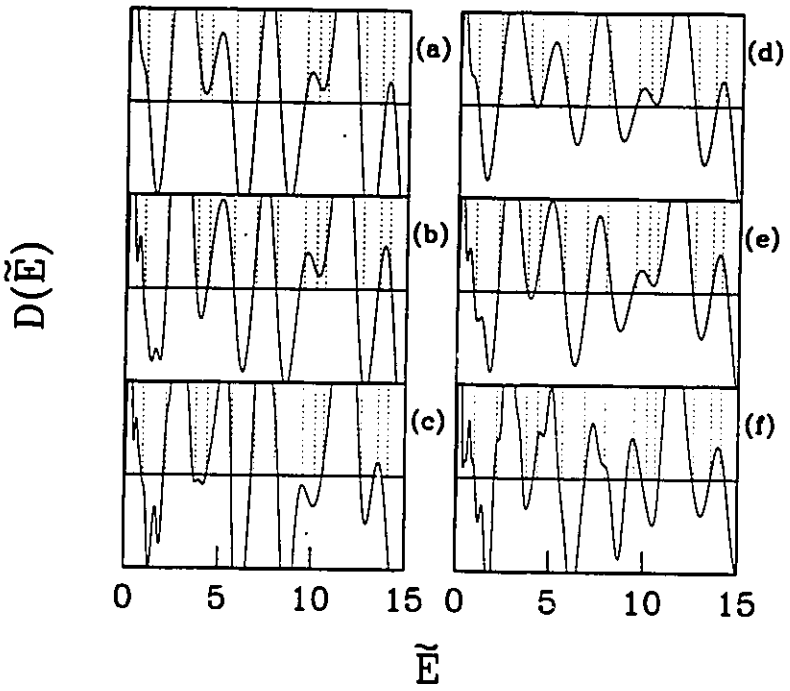

Figure 19. Plot of $D(\tilde{E})$ as a function of the scaled energy $\tilde{E}$ for the wedge billiard with $\phi = 49°$. (*a*), (*b*) and (*c*) correspond to 2-, 3- and 4-symbol cells respectively, with the X_γ's for pruned primitive periodic orbits replaced by approximate expressions like (51). (*d*), (*e*) and (*f*) correspond to 2-, 3- and 4-symbol cells respectively, with the X_γ's for pruned primitive periodic orbits set equal to zero.

Instead of making replacements such as those in (51) for the case of 2-symbol cells, one can try replacing all the X's corresponding to pruned orbits by zeros in expansions such as (50). This may be just as reasonable a guess for the pruned orbits as approximations such as (51). The results obtained for $D(\tilde{E})$ as a function of $\tilde{E}$ for 2-, 3- and 4-symbol cells are shown in figure 19(*d*), (*e*) and (*f*). We see that there is perhaps a slight improvement in comparison with the results of figure 19(*a*), (*b*) and (*c*), but we do not think the outcome is significantly better.

It is instructive to compare the results for $D(\tilde{E})$ based on the symbolic dynamics with plots of $D(\tilde{E})$ calculated using T-matrices of comparable size in the coordinate space representation. Figure 20 shows such a comparison. To the right of the curves in figure 20(*a*), (*b*) and (*c*), which are the same as figure 19(*a*), (*b*) and (*c*), we show plots of $D(\tilde{E})$ calculated by the scaling method of section 2, using T-matrices of dimensions 4, 8 and 16 respectively. The curves in figure 20(*d*) and (*e*) are clearly not as good as the curves in figure 20(*a*) and (*b*) from the symbolic dynamics, but figure 20(*f*) is definitely superior to figure 20(*c*).

To sum up, we note first of all that a quantization scheme based on the symbolic dynamics requires a knowledge of the shortest primitive periodic orbits and their properties, unlike the representation of the transfer operator in coordinate space. This is generally a disadvantage. However, if one has available the shortest primitive periodic orbits, and if the symbolic dynamics is *complete* (meaning no pruning occurs), the present method for n-symbol cells may be implemented by computing the cycle expansion in *irreducible*

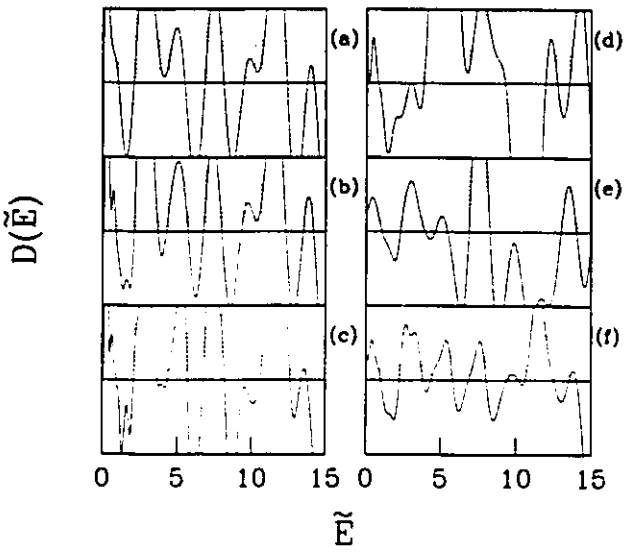

Figure 20. Plot of $D(\tilde{E})$ as a function of the scaled energy $\tilde{E}$ for the wedge billiard with $\phi = 49^\circ$. (*a*), (*b*) and (*c*) are the same plots as (*a*), (*b*) and (*c*) in the preceding figure. (*d*), (*e*) and (*f*) were calculated from T-matrices in the coordinate space representation having dimensions of 4, 8 and 16 respectively.

periodic orbits having code length up to 2^n. On the other hand, if some of the periodic orbits are pruned and the pruning rules are unknown, there is no systematic way of solving for various products of T-matrix elements in terms of the primitive periodic orbits, making it difficult to implement the present method for n-symbol cells with $n \geqslant 4$. Moreover, there is no guarantee that a pruned system will provide enough independent relations to solve for the required products of the T-elements. We conclude that, although this approach is interesting as an alternative formulation of Bogomolny's transfer operator, it is not a good way of estimating semiclassical energy eigenvalues.

4. Discussion and conclusions

The studies reported in this paper show that, overall, finite approximations to Bogomolny's transfer operator in coordinate space are capable of giving excellent results for the semiclassical energy eigenvalues of a variety of systems. While our calculations have been limited to the wedge billiard and the circle billiard, the results appear to be about equally satisfactory for systems showing hard chaos (the 49° and 60° wedges), for systems showing soft chaos or mixed behaviour (the 41° and 30° wedges), and for integrable systems (the circle billiard and the 45° wedge billiard). This is the main conclusion of our work.

There are several advantages to the transfer operator approach to semiclassical quantization compared with quantization schemes based on knowing the periodic orbits of the system.

1. Most important is the fact that it is not necessary to know about the periodic orbits

of the system and, therefore, not necessary to have a systematic way of finding them—a difficult task in a generic system, particularly if a symbolic representation of the periodic orbits is not known. Not needing the periodic orbits also implies that there is no problem regarding the infinite families of primitive periodic orbits with nearly the same action, which arise in the anisotropic Kepler problem [36] and in the wedge billiard [24, 25]. In periodic orbit theory, these infinite families cannot be treated in a straightforward manner because the stationary phase approximation, used to derive the Gutzwiller trace formula, fails as one approaches the accumulation point of a given family. Bogomolny's theory avoids this problem because it does not employ the stationary phase approximation to pull out the periodic orbits of the system.

2. A second major advantage is that, in calculating a finite approximation to the transfer operator up to some energy $E_{\max}$, it is not necessary to know about the classical motion on a scale very much smaller than a cell of area $2\pi\hbar$ on any suitably chosen PSS in phase space. This is equivalent to saying that one does not need to know the classical motion crossing the PSS in coordinate space on a scale very much smaller than half a de Broglie wavelength. Our calculations for the wedge billiard at five different wedge angles bear this out. Although a division of the PSS in phase space into $N_{\rm P}(E)$ Planck cells (see equation (4)) does not yield very good results for the energy eigenvalues in the vicinity of E, increasing the number of cells by a factor of about 10 greatly improves the accuracy of the results at this energy. Thus, although the Planck cells are too coarse, it is unnecessary to know the details of the classical motion on scales smaller than about one tenth of a Planck cell in order to obtain very good semiclassical estimates of the energy eigenvalues by means of the transfer operator in coordinate space. It is in this sense that one can say that the Heisenberg uncertainty principle is built into the theory in a natural way.

3. There appear to be no formal convergence problems in Bogomolny's method of calculating semiclassical energy eigenvalues. This is in contrast to calculations employing the Gutzwiller trace formula or the dynamical zeta function which, in general, are not absolutely convergent because of the exponential proliferation of periodic orbits with increasing action or word length [37, 38, 25].

4. Even if the Gutzwiller periodic orbit sum (or zeta product) were absolutely convergent, the number of primitive periodic orbits required to determine N_m accurate energy eigenvalues increases exponentially with N_m, whereas in Bogomolny's approach, the required dimension of the T-matrix increases in proportion to $N_m^{1/2}$ (see (19), with $\tilde{E}^{1/2} \approx N_{\rm TF}(\tilde{E})$ from (17) and (18)), which in turn implies that the number of matrix elements that have to be calculated increases linearly with N_m. This difference in the computational requirements is sufficient to turn an intractable calculation into one that can be readily performed.

What disadvantages might one encounter in implementing Bogomolny's method of calculating semiclassical energy eigenvalues? Since the formalism does not specify how to choose the PSS, it is conceivable that one might have some difficulty in making a suitable choice, although this was not a problem in the present work. Probably the best choice is the one for which it is easiest to calculate the classical trajectories from one point on the PSS to another, including the actions and phase indices. Another guideline may be not to choose the PSS to be larger than necessary. (For the wedge billiard, we found that calculations performed with the PSS chosen to be the vertical wall plus the tilted wall were not as satisfactory as the ones with the PSS taken to be the tilted wall alone.)

Finally, we would like to mention that there is an interesting connection between the quantitative aspect of point 2 above and the conclusion reached by Tomsovic and Heller [39, 40] from their studies of the stadium billiard in the time domain. To obtain close

agreement between certain correlation functions derived from the semiclassical and the exact quantum time-dependent Green functions, they found it necessary to include contributions from classical trajectories propagating over comparatively long times—long enough, in fact, to produce heteroclinic orbits winding back and forth many times through a given Planck cell in the phase space. This is similar to our finding that accurate semiclassical energy eigenvalues require a knowledge of the classical dynamics in phase space on a scale of about one tenth of a Planck cell. It would be very interesting to know if the converse is true, that is, whether it is possible to deduce the details of the classical dynamics *on this scale* from the exact quantum energy eigenvalues and eigenfunctions. The answer to this question would tell us a great deal about the precise nature of 'quantum smoothing of the classical motion'.

Acknowledgments

We would like to thank E B Bogomolny for helpful discussions at an early stage of this work. We have also benefited from discussions with R K Bhaduri, M Kvale, D Provost and N D Whelan. This research was supported by the Natural Sciences and Engineering Research Council of Canada.

References

[1] Bogomolny E B 1992 *Nonlinearity* 5 805
[2] Bogomolny E B 1992 *CHAOS* 2 5
[3] Lauritzen B 1992 *CHAOS* 2 409
[4] Bogomolny E B and Caroli M 1993 *Physica* 67D 88
[5] Szeredi T, Lefebvre J H and Goodings D A 1993 *Phys. Rev. Lett.* 71 2891
[6] Haggerty M R 1993 *PhD thesis* Massachusetts Institute of Technology
[7] Gutzwiller M C 1971 *J. Math. Phys.* 12 343
[8] Gutzwiller M C 1990 *Chaos in Classical and Quantum Mechanics* (New York: Springer)
[9] Berry M V 1986 *Quantum Chaos and Statistical Nuclear Physics*, ed T H Seligman and H Nishioka *Lecture Notes in Physics Vol. 263* (Berlin: Springer) p 1
[10] Voros A 1988 *J. Phys. A: Math. Gen.* 21 685
[11] Berry M V and Keating J P 1990 *J. Phys. A: Math. Gen.* 23 4839
[12] Keating J P 1992 *Proc. R. Soc.* A 436 99
[13] Berry M V and Keating J P 1992 *Proc. R. Soc.* A 437 151
[14] Sieber M and Steiner F 1991 *Phys. Rev. Lett.* 67 1941
[15] Doron E and Smilansky U 1992 *CHAOS* 2 117
[16] Doron E and Smilansky U 1992 *Nonlinearity* 5 1055
[17] Boasman P A 1992 *PhD thesis* University of Bristol
[18] Artuso R, Aurell E and Cvitanović P 1990 *Nonlinearity* 3 325, 361
[19] Berry M V 1981 *Eur. J. Phys.* 2 91
[20] Lehtihet H E and Miller B N 1986 *Physica* 21D 93
[21] Richter P H, Scholz H-J and Wittek A 1990 *Nonlinearity* 3 45
[22] Wittek A 1991 *doctoral thesis* University of Bremen
[23] Szeredi T and Goodings D A 1992 *Phys. Rev. Lett.* 69 1640
[24] Szeredi T and Goodings D A 1993 *Phys. Rev.* E 48 3518
[25] Szeredi T and Goodings D A 1993 *Phys. Rev.* E 48 3529
[26] Wojtkowski M P 1990 *Commun. Math. Phys.* 126 507
[27] Whelan N D, Goodings D A and Cannizzo J K 1990 *Phys. Rev.* A 42 742
[28] Chernov N I 1991 *Physica* 53D 233
[29] Schulman L S 1981 *Techniques and Applications of Path Integration* (New York: Wiley) p 38
[30] Aurich R and Steiner F 1992 *Phys. Rev.* A 45 583
[31] Goodings D A and Szeredi T 1991 *Am. J. Phys.* 59 924
[32] Berry M V 1978 *Topics in Nonlinear Dynamics, La Jolla, 1978 (Proc. of the Workshop on Topics in Nonlinear Dynamics.)* AIP Conf. Proc. No. 46, ed by S Jorna (New York, AIP) p 16
[33] Berry M V and Tabor M 1976 *Proc. R. Soc.* A 349 101
[34] Berry M V and Tabor M 1977 *J. Phys. A: Math. Gen.* 10 371
[35] Cvitanović P and Eckhardt B 1989 *Phys. Rev. Lett.* 63 823
[36] Tanner G and Wintgen D 1992 *CHAOS* 2 53
[37] Eckhardt B and Aurell E 1989 *Europhys. Lett.* 9 509
[38] Sieber M and Steiner F 1990 *Phy. Lett.* 144 A 159
[39] Tomsovic S and Heller E J 1991 *Phys. Rev. Lett.* 67 664

Chapter 4

Eigenvalues of the T-Operator

In previous chapters, we have used the straightforward definition of Bogomolny's semiclassical quantization condition, looking for energies at which the determinant $|\det[1 - T(E)]|$ becomes zero. However, Bogomolny's semiclassical quantization condition is also the characteristic equation for the T-operator and can be interpreted as the energy for which an eigenvalue of the T-operator is 1. In this way, the eigenvalues of the T-operator are responsible for generating the energy eigenstates of the system. To emphasize the distinction between the eigenvalues of the T-operator and the energy eigenvalues of the Hamiltonian, it is helpful to note that the T-operator and its eigenvalues can be calculated for any energy E. The energy eigenvalues of the Hamiltonian correspond to the particular energies $E = E_n$ for which one of the eigenvalues of the T-operator is unity. The focus of this chapter is on the properties of T-operator eigenvalues of the circle and wedge billiards. Some of the work on the circle billiard presented here overlaps with Boasman's thesis [6]. The T-operator eigenvalues of the wedge billiard have not been studied before.

The studies described in this chapter were undertaken to explore the conjecture that the T-operator eigenvalues might show qualitatively different behaviour for the regular and chaotic systems. While studying the Nelson potential (a smooth potential), Haggerty [21] [22] noticed that the T-operator eigenvalues behave differently as a function of energy depending on whether the system is 'nearly' integrable or 'mostly' chaotic. However, Boasman [6], who discusses in detail the properties of T-operator eigenvalues for the circle billiard (an integrable system) and qualitatively investigates the T-operator eigenvalues of the Africa (a mixed system) and stadium (a chaotic system) billiards, does not find a difference in behaviour of the T-operator eigenvalues depending on the type of dynamical system. Could these differing results concerning the behaviour of T-operator eigenvalues come from the fact that Boasman was studying force-free billiards where the shape of the boundary determines the dynamics of the system and that Haggerty's system involves a smooth potential? Since the wedge billiard involves a combination of a smooth potential and billiard boundaries, how do the T-operator eigenvalues behave in this case? Are there any properties of the T-operator eigenvalues which are characteristic of particular types of dynamical systems? The primary motivation for this chapter is to attempt to answer these questions.

In addition to the work of Haggerty [21] [22] and Boasman [6] [7], there are two other papers which discuss, to some extent, the eigenvalues of the T-operator. Lauritzen [28] presents a general form for the T-operator of integrable systems and

shows that in the semiclassical limit, Bogomolny's semiclassical quantization condition is equivalent to EBK quantization. Also, from this general form, one can easily derive an analytic expression for the T-operator eigenvalues as a function of energy in the limit $\hbar \to 0$. Bogomolny and Caroli [9] discuss the distribution of T-operator eigenvalues for completely chaotic Hamiltonian systems defined by surfaces or billiards with constant negative curvature, in the context of demonstrating the unitarity of the T-operator.

This chapter is organized in the following way. A very brief description of the general behaviour of the T-operator eigenvalues as a function of energy is presented in Sec. 4.1. From this, I show how to use the T-operator eigenvalues to find energy eigenstates of the system. Then, I apply this technique to the circle and wedge billiards and compare these results with the ones found in Chap. 3. In Sec. 4.2, I focus on the T-operator eigenvalues of integrable systems and based on Lauritzen's work, I describe their special connection with quantum numbers of the Hamiltonian system. The particular examples used to illustrate this are the circle and 45° wedge billiards. Finally, in Sec. 4.3, I discuss the properties of T-operator eigenvalues in more detail and investigate the possibility that they can reveal information about the dynamical nature of the system. These results are related to those of a very recent study by Rouvinez [37] on the properties of the eigenvalues of the scattering matrix $S(E)$.

4.1 Energy Eigenstates from T-Operator Eigenvalues

As mentioned at the beginning of this chapter, one of the two ways to interpret Bogomolny's semiclassical quantization condition is to find the energies $E = E_n$ for which one of the eigenvalues of the T-operator becomes unity. These energies $E = E_n$ are the energy eigenstates of the Hamiltonian system. According to Haggerty [21] [22], this method of finding energy eigenstates produces better results than the method of finding the minima of $|\det[1 - T(E)]|$. With the method involving the determinant, it becomes increasingly difficult at higher energies to resolve the minima which indicate energy eigenstates of the system. Since the T-operator is only unitary in the semiclassical limit and, the T-matrix is a finite approximation to the T-operator, the T-matrix eigenvalue which satisfies the quantization condition is only approximately equal to one. Consequently, taking the determinant, involving a product of all the eigenvalues of the T-matrix, has the effect of obscuring the minima [21] [22]. However, the problem of resolving energy eigenstates is no longer an issue when they are obtained directly from the eigenvalues of the T-matrix and all of the energy eigenstates up to $N_p(E)$ can be located. The only drawback of this method is that a program is required to follow the T-operator eigenvalues as a function of energy and this can considerably slow down the execution speed.

4.1.1 General Behaviour of T-operator Eigenvalues

The T-operator eigenvalues vary continuously as a function of energy. In the complex plane, they trace out curves (subsequently referred to as *T-operator eigenvalue curves*) that rotate about the origin in the counterclockwise direction as the energy is increased (Fig. 4.1). Initially, at low energies, all of the T-operator eigenvalues hover close to the origin with magnitudes typically less than 0.1. Their magnitudes gradually increase with increasing energy and, one by one, they spiral out towards the unit circle. Once they reach the vicinity of the unit circle, they continue to rotate but remain in that region for all higher energies. The circle billiard eigenvalue curves shown in Fig. 4.1(b) are from the first ten T-operator eigenvalues that move out to the unit circle. Although it is not evident on this figure, each T-operator eigenvalue spiralled out to the unit circle at a different energy. An interesting characteristic of the T-operator eigenvalues of the circle billiard is that they all spiral out with approximately the same rate and begin at the same phase angle.

For a given energy, the T-operator has a subset of eigenvalues which have reached the proximity of the unit circle and a second subset of eigenvalues near the origin or in the process of arriving at the unit circle. The T-operator eigenvalues near the unit circle are the ones which contribute to the energy spectrum. They satisfy Bogomolny's semiclassical quantization condition as the eigenvalue curves cross the positive real axis. Since the T-operator is unitary only in the limit $\hbar \to 0$, it is not

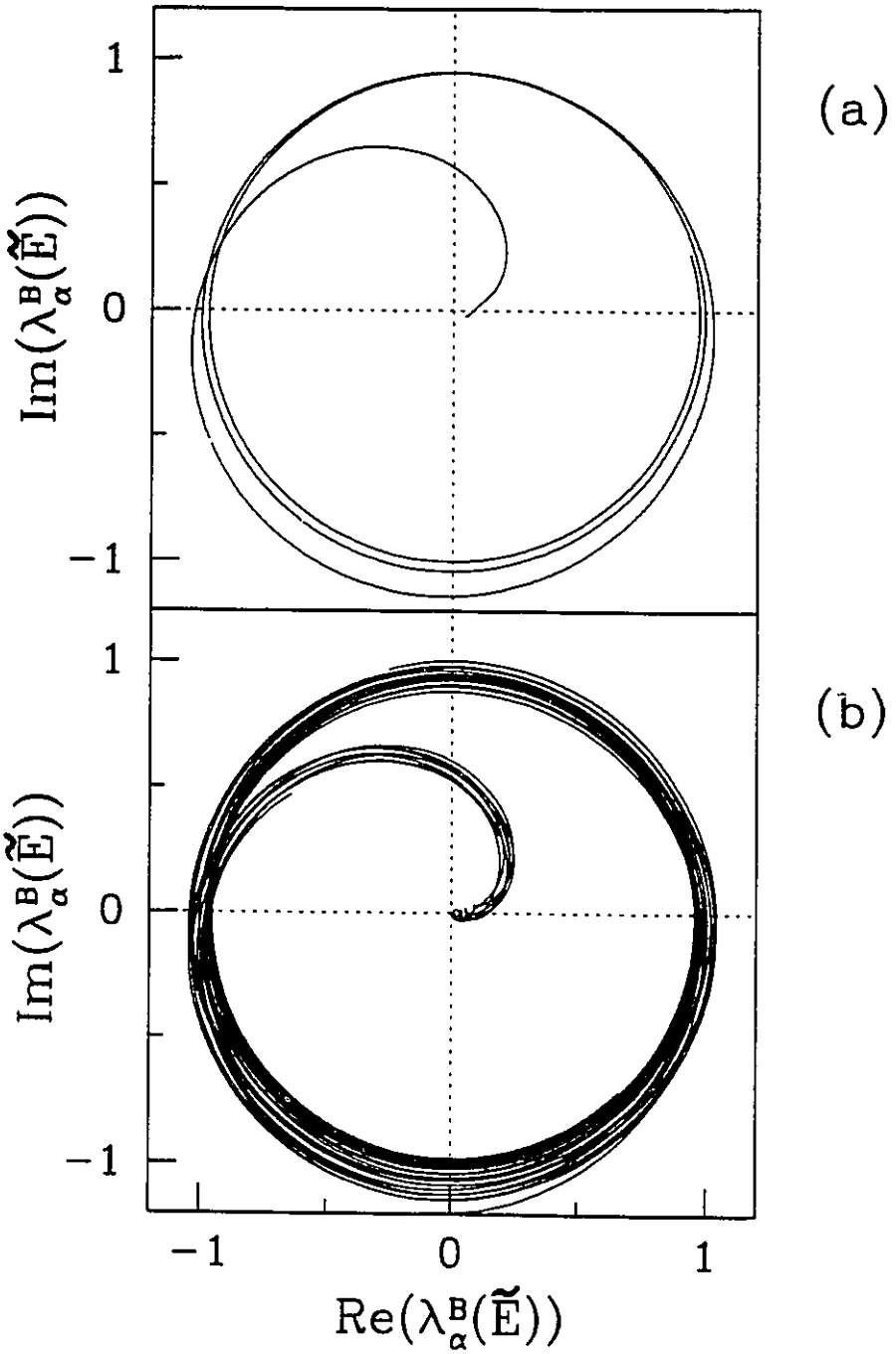

Figure 4.1: The generic behaviour of T-operator eigenvalues $\lambda_\alpha^B(\tilde{E})$ as a function of scaled energy $\tilde{E}$ portrayed in the complex plane. The T-operator eigenvalues were obtained from the 150×150 T-matrix for the circle billiard. (a) The eigenvalue curve for the 6th T-matrix eigenvalue. (b) The eigenvalue curves for the first ten T-matrix eigenvalues. There are two T-operator eigenvalue curves, one at $\approx 135°$ and the other at $\approx 270°$, which do not start at the origin. This occurs since when $\tilde{E} = 0$, $E \approx 1.2$, and the two first eigenvalue curves have already spiralled out from the origin.

surprising that the T-operator eigenvalues do not lie exactly on the unit circle. Also, there are errors induced by finite approximations to the T-operator, but these can be reduced by increasing the dimension of the T-matrix (or, equivalently, the number of cells on the PSS). Hence, as the T-operator eigenvalues spiral outward from the origin, one must decide at which point (with which magnitude) they start contributing to the energy spectrum. Unfortunately, this critical magnitude depends on the system and on the amount of errors induced by finite approximations. A 'bad' choice for the critical magnitude can obviously lead to additional or missing energy eigenstates.

Fortunately, for most systems studied to date, a 'good' choice for the critical magnitude has not been difficult to estimate from a brief survey of the behaviour of the T-operator eigenvalue curves. For example, a critical magnitude of 0.7 poses no problem for T-matrices of the circle billiard. In the worst case, such as the Nelson potential in a 'nearly regular' régime, the eigenvalue curves spiral out very gradually making it very difficult to choose the critical magnitude [21] [22]. For this potential, there is an overlapping region of magnitudes roughly between 0.475 and 0.55 where T-operator eigenvalues that cross the positive real axis may or may not contribute to the energy spectrum. Thus, unfortunately, in these cases, the magnitude alone is not sufficient to distinguish between cases that should or should not contribute to the energy spectrum. Haggerty found that he could classify these troublesome cases by comparing the semiclassical staircase with the Thomas-Fermi smoothed staircase function [21] [22]. Otherwise, for all other T-operator eigenvalues, a critical value of

0.5 worked well.

A plot of the imaginary part of the T-operator eigenvalues as a function energy (Fig. 4.2) is another informative way to look at the behaviour of the eigenvalue curves. From Fig. 4.2, one can see the energy at which each T-operator eigenvalue begins to move out to the unit circle. The crossing with the positive real axis in Fig. 4.1 corresponds to a crossing of the energy axis from a negative to a positive imaginary part in Fig. 4.2. These crossings generate the approximate energy eigenstates of the system and may be compared to the exact energy eigenstates (marked by circles on the energy axis of Fig. 4.2). In general, the number of T-operator eigenvalues that have reached the unit circle at a particular energy is given by $N_p(E)$ (for the circle billiard, an expression for $N_p(E)$ was derived in Sec. 2.2 of Chap. 3). All remaining T-operator eigenvalues, the number depending on the dimension of the T-matrix, have magnitudes less than unity (most of them being close to zero). Hence, strictly speaking, only a subset of the T-matrix is approximately unitary (the term 'approximately' is used since the magnitudes of the T-operator eigenvalues are not exactly unity except in the limit $\hbar \to 0$). When the dimension of the T-matrix equals $N_p(E)$, *all* of the T-operator eigenvalues are near the unit circle and the entire T-matrix is approximately unitary. A detailed discussion of this is given by Boasman [6].

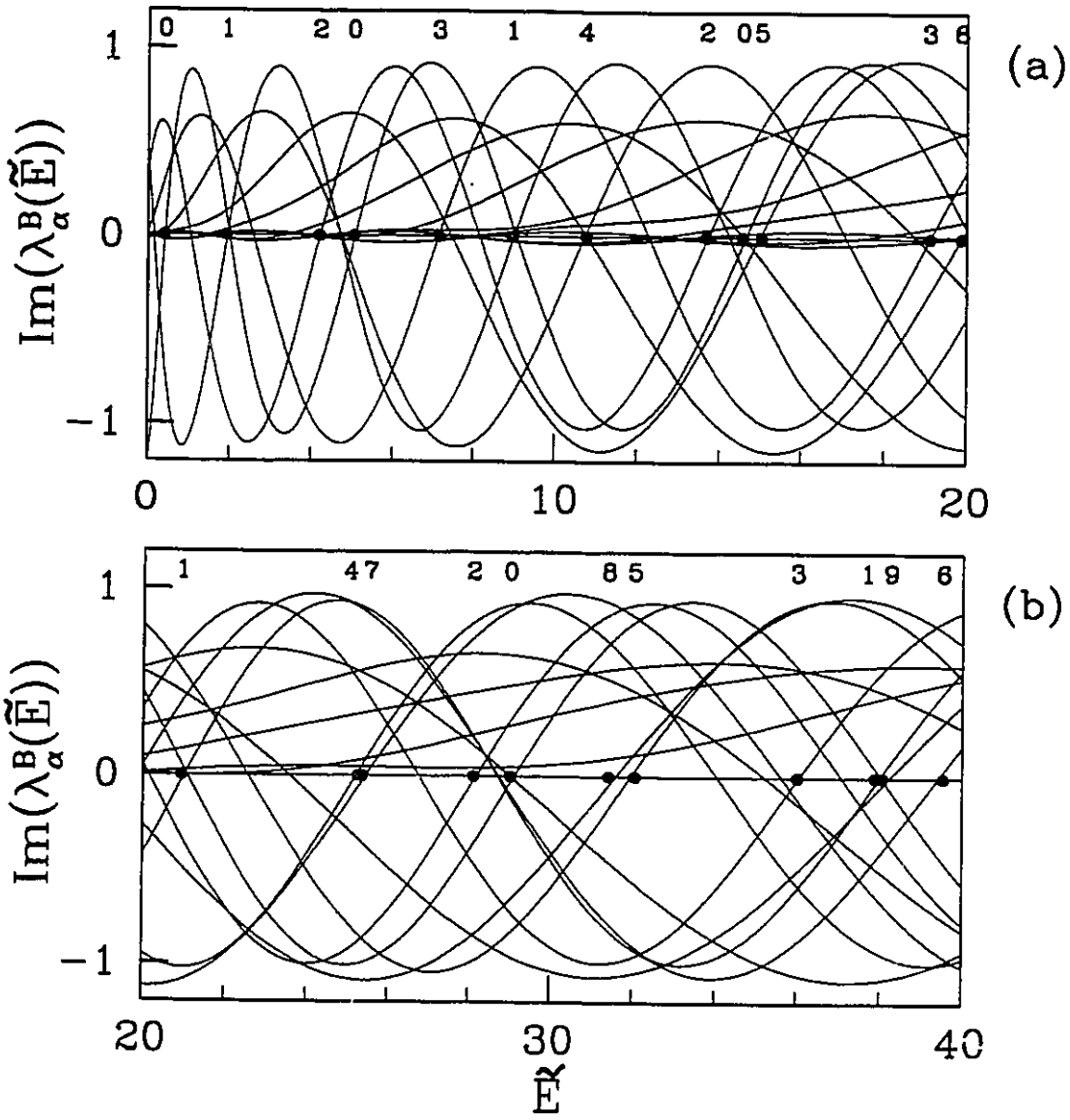

Figure 4.2: Eigenvalue curves $\mathrm{Im}(\lambda_\alpha^B(\tilde{E}))$ for the circle billiard plotted as a function of scaled energy $\tilde{E}$. The T-matrix used was 150×150. The circles on the energy axis mark the locations of exact energy eigenstates. The numbers above the energy eigenvalues are the values of the quantum number ν (see Appendix A). Notice that a particular eigenvalue curve locates energy eigenvalues with the same quantum number ν.

4.1.2 New Results for the Circle and Wedge Billiards

Briefly, the numerical procedure for finding energy eigenstates involves following the T-operator eigenvalues as a function of energy. In general, this is achieved by numerically diagonalizing the T-matrix at discrete energy values incremented by small energy steps. When a T-operator eigenvalue has a magnitude above the critical value, it contributes to the energy spectrum whenever it crosses the positive real axis. Since energy is incremented by small finite amounts, one will obtain energies for which a T-operator eigenvalue is just below or above the positive real axis. A simple linear extrapolation can be used to estimate the energy of the crossing. A critical magnitude of 0.7 and energy increments of $\Delta\tilde{E} = 0.01$ were used in this study.

For the circle billiard, it is not necessary to numerically diagonalize the T-matrix since it has a special form allowing one to write an analytic expression for its eigenvalues. This special form can be demonstrated by considering the T-matrix elements (combining Eqs. (2),(9) and (10) of Chap. 3),

$$T_{kl} = \left(\frac{\pi R(2mE)^{\frac{1}{2}}}{i\hbar N^2}\sin\left(\frac{|k-l|\,\pi}{N}\right)\right)^{\frac{1}{2}}\exp\left[\frac{i2R(2mE)^{\frac{1}{2}}}{\hbar}\sin\left(\frac{|k-l|\,\pi}{N}\right) - i\pi\right] \qquad (4.1)$$

where R is the radius of the circle and N is the number of cells along the Poincaré surface of section (circle boundary) or the matrix dimension. It is easy to see that this T-matrix is symmetric since $\sin\frac{|l-k|\pi}{N} = \sin\frac{|k-l|\pi}{N}$. In addition, since $\sin\frac{|N-l|\pi}{N} = \sin\frac{|(l+j)-j|\pi}{N}$, $T_{N,l} = T_{l+j,j}$ and the T-matrix has the general form

$$T(E) = \begin{bmatrix} t_0 & t_1 & t_2 & \cdots & t_2 & t_1 \\ t_1 & t_0 & t_1 & \cdots & t_3 & t_2 \\ t_2 & t_1 & t_0 & \cdots & t_4 & t_3 \\ \vdots & \vdots & \vdots & \ddots & \vdots & \vdots \\ t_2 & t_3 & t_4 & \cdots & t_0 & t_1 \\ t_1 & t_2 & t_3 & \cdots & t_1 & t_0 \end{bmatrix}$$

This matrix is a special case of cyclic matrices (circulants) for which the eigenvalues are given analytically by

$$\lambda_k = \sum_{l=0}^{N-1} t_l e^{\frac{2\pi kli}{N}} \tag{4.2}$$

where, in this case,

$$t_l = \left(\frac{\pi R(2mE)^{\frac{1}{2}}}{i\hbar N^2} \sin\left(\frac{l\pi}{N}\right) \right)^{\frac{1}{2}} \exp\left[\frac{i2R(2mE)^{\frac{1}{2}}}{\hbar} \sin\left(\frac{l\pi}{N}\right) - i\pi \right]. \tag{4.3}$$

This expression is equivalent to Eq.(5.66) given in Boasman's thesis [6], derived in a slightly different manner. Hence, the eigenvalues of the T-operator for the circle billiard can be calculated with Eq.(4.2) rather than by numerically diagonalizing the T-matrix, greatly decreasing the execution time. Unfortunately, there isn't a similar analytic expression for the T-operator eigenvalues for the wedge billiard and one must use a numerical diagonalization routine.

The scaled semiclassical energy eigenstates $\tilde{E}_n$ for the circle billiard and for five different wedge billiards, and in each case for two matrix dimensions, were recalculated using the technique of the T-operator eigenvalue curves. New results for the mean deviation $\langle(\tilde{E}_n - \tilde{E}_n^{exact})\rangle$ and the root-mean-square deviation $\langle(\tilde{E}_n - \tilde{E}_n^{exact})^2\rangle^{\frac{1}{2}}$ of $\tilde{E}_n$ from the exact energy eigenstates of the Schrödinger equation $\tilde{E}_n^{exact}$, are given

in Table 4.1. This table is very similar to Table 2 of Chap. 3 and it compares the results obtained from the T-operator eigenvalue curves (new) with those calculated from the zeros of the functional determinant $D(\tilde{E})$ (old). The results for the circle billiard which were not given in Chap. 3 have been added to Table 4.1. The exact energy eigenvalues for the circle billiard are zeros of the Bessel function (Appendix A) and were calculated using Numerical Recipes routines [32]. Similarly, for the 45° wedge billiard, the exact energy eigenvalues were calculated using the quantum solution (Appendix A) and Numerical Recipes routines for the Airy functions. For the wedge angles other than 45°, the exact energy eigenvalues were calculated by Szeredi [39] using the brute-force method of numerically diagonalizing a large Hamiltonian matrix (typical dimensions: 4900×4900). The energy eigenstates were then scaled using the Thomas Fermi staircase function: $\tilde{E}_n = N_{TF}(E_n)$. For the wedge billiards, $N_{TF}(E_n)$ is given by Eq. (17) of Chap. 3 while for the circle billiard, it is given by [25]

$$N_{TF}(E) = \frac{mR^2E}{2\hbar} - R\left(\frac{mE}{2\hbar}\right)^{\frac{1}{2}} + \frac{1}{6}. \tag{4.4}$$

As discussed in Chap. 3, the functional determinant $D(\tilde{E})$ calculated from 25×25 T-matrices often failed to produce 30 energy eigenvalues (the number of eigenvalues we decided to use for the statistical calculations of Table 4.1). For example, in the case of the 49° wedge, the functional determinant fails to cross the energy axis at $\tilde{E} \approx 28$ (see Fig. 6(a) of Chap. 3 and Fig. 4.3). Since the scaled semiclassical

billiard system	T-matrix dimension	$\langle(\tilde{E}_n - \tilde{E}_n^{exact})\rangle$ new	old	$\langle(\tilde{E}_n - \tilde{E}_n^{exact})^2\rangle^{\frac{1}{2}}$ new	old	number of eigenstates
circle	25	0.015	–	0.270	–	30
circle	150	0.015	–	0.015	–	30
60° wedge	25	0.030	0.025	0.084	0.125	30
60° wedge	150	0.025	0.028	0.078	0.081	30
49° wedge	25	0.040	0.042	0.106	0.145	24
49° wedge	150	0.023	0.025	0.077	0.076	30
45° wedge	25	0.039	0.028	0.076	0.087	26
45° wedge	150	0.030	0.031	0.051	0.053	30
41° wedge	25	0.046	0.054	0.077	0.130	30
41° wedge	150	0.028	0.027	0.048	0.051	30
30° wedge	25	0.043	0.053	0.083	0.089	20
30° wedge	150	0.026	0.026	0.050	0.052	30

Table 4.1: New results for the energy eigenvalues of the circle and wedge billiards. Comparison between the scaled energy eigenvalues $\tilde{E}_n$, calculated from the T-operator eigenvalue curves (new) and from the zeros of the functional determinant $D(\tilde{E})$ (old), and the exact scaled energy eigenvalues $\tilde{E}_n^{exact}$ of the Schrödinger equation. Although 30 energy eigenvalues were obtained with the new method, the averages were calculated for the number of energy eigenvalues that could be obtained with the old method. The values for the wedge billiard are slightly different than the ones quoted in Table 2 of Chap. 3 since these were rescaled according to Eq. (17) of Chap. 3.

energy eigenvalues are determined from the zeros of $D(\tilde{E})$, no estimates of the 25th and 26th could be obtained. Figure 4.3 demonstrates how this problem is eliminated by using the T-operator eigenvalue curves to locate the energy eigenvalues. We had no difficulty locating the first 30 energy eigenvalues for all T-matrices of Table 4.1 but for the sake of comparison with the results listed in Table 2 of Chap. 3, we kept the same number of energy eigenvalues. Hence, in terms of resolving energy eigenvalues, the method based on the T-operator eigenvalue curves is more successful.

The comparison made in Table 4.1 shows that the values for $\langle(\tilde{E}_n - \tilde{E}_n^{exact})\rangle$ are not significantly different for the two methods but that the results for $\langle(\tilde{E}_n - \tilde{E}_n^{exact})^2\rangle^{\frac{1}{2}}$ are consistantly better when the energy eigenvalues are found from the T-operator eigenvalue curves. The improvement in $\langle(\tilde{E}_n - \tilde{E}_n^{exact})^2\rangle^{\frac{1}{2}}$ is more pronounced for the 25×25 T-matrices. Hence, in terms of minimizing the effect of errors caused by finite approximations, the method based on the T-operator eigenvalue curves is, once again, better. In fact, overall, the method based on the T-operator eigenvalue curves produces better results but, one must be willing to accept a longer execution time.

When I calculated the differences between the scaled semiclassical energy eigenvalues $\tilde{E}_n$ and the exact energy eigenvalues $\tilde{E}_n^{exact}$, I noticed an overall increase in the absolute errors as a function of energy. Hence, it appears that Bogomolny's T-operator method works better at lower energies than at higher energies. At this point, it is worthwhile to make the following clarification. The T-operator is a semiclassical

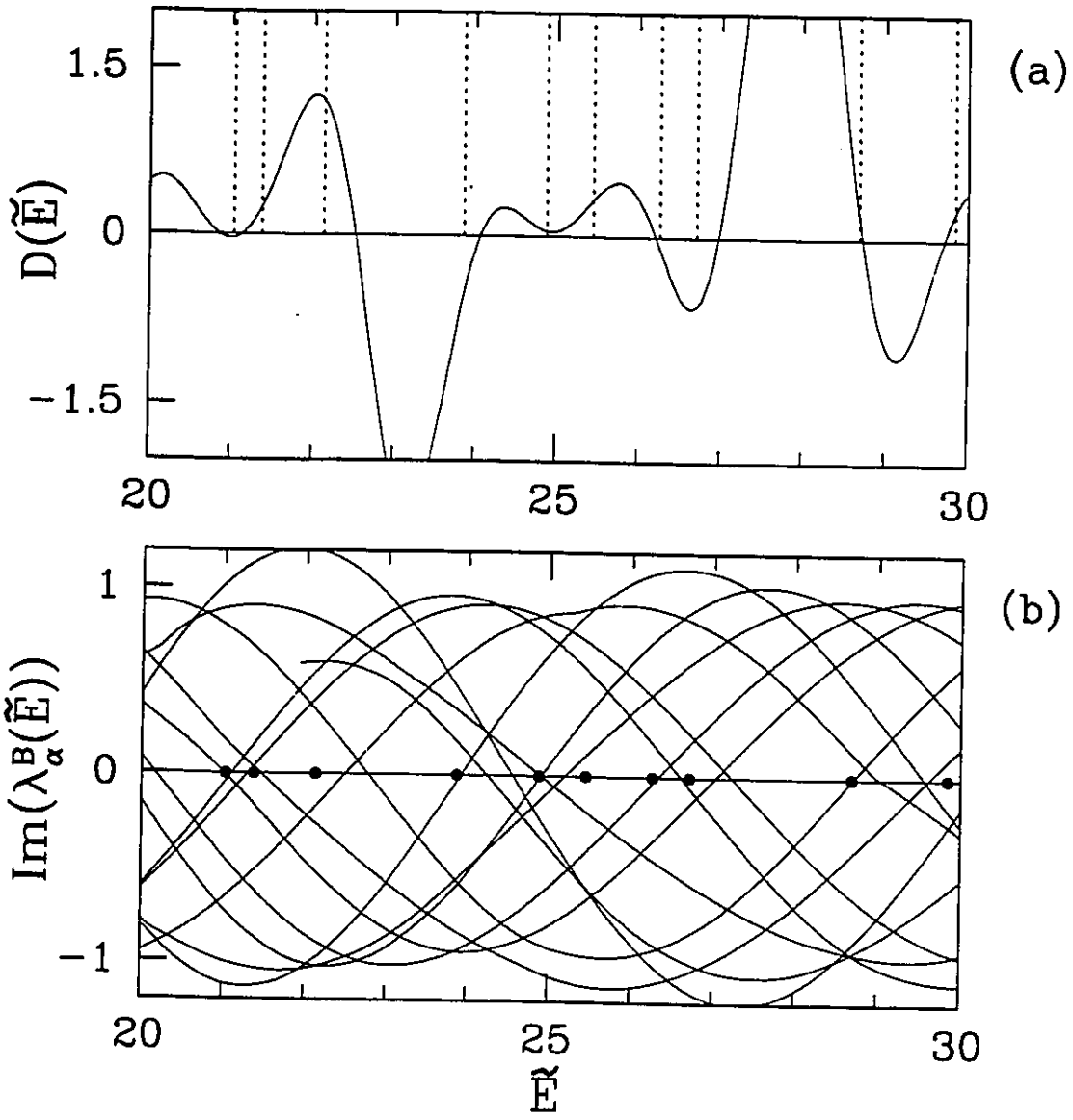

Figure 4.3: Comparison of: (a) the functional determinant $D(\tilde{E})$ and (b) T-operator eigenvalue curves $\mathrm{Im}(\lambda_\alpha^B(\tilde{E}))$ for the 25 × 25 T-matrix of the 49° wedge billiard. $D(\tilde{E})$ fails to give estimates for the 25th and 26th energy eigenvalues (located near $\tilde{E} = 25.5$) while the T-eigenvalue curves have no difficulties in locating them.

propagator in the sense that, in relation to the exact quantum mechanical propagator, it is correct to leading order of $\hbar$. On this basis alone, the T-operator is expected to give better approximations to the exact energy eigenvalues in the limit $\hbar \to 0$ (or, at high energies). However, as energy is increased, larger T-matrices are required to give a more accurate representation of the physical situation (this is essentially because $N_p(\tilde{E})$ increases with energy). In our calculations, we are keeping the T-matrix dimension N constant for all energy values (for the reasons described in Sec. 2.3.1 of Chap. 3). Consequently, as energy is increased, the "resolution" of the T-matrix is effectively decreasing since it no longer contains enough detailed information to be accurate. Perhaps one way to overcome this problem would be to keep the ratio $N/N_p(\tilde{E})$ constant for all energies. However, there is no guarantee that the desirable ratio $N/N_p(\tilde{E})$ for low energies is the same for high energies (we have not investigated this in detail).

4.2 T-Operator Eigenvalue Curves of Integrable Systems

While studying the Nelson potential in the 'nearly' regular régime, Haggerty noticed that the eigenstates produced by a single eigenvalue curve have the same 'almost good' quantum number [21] [22]. Similarly, by labelling the eigenstates of the circle billiard according to their quantum number ν (Appendix A), we found that

individual eigenvalue curves produced eigenstates with the same quantum number ν (see Fig. 4.2). This suggested that the relation between T-operator eigenvalue curves (or T-operator eigenvalues) and quantum numbers might be a general result for all integrable systems.

In Sec. 4.2.1, I will provide a theoretical explanation for the connection between eigenvalue curves and quantum numbers based on the work of Lauritzen [28] on semiclassical quantum maps of integrable systems. In Sec. 4.2.2, I will show how this theory applies to the circle billiard. The eigenvalue curves for the 45° wedge billiard are studied in Sec. 4.2.3. In this case, there is a discrepancy between the theoretical prediction for the behaviour of the eigenvalue curves and their actual trend obtained from Bogomolny's T-operator.

4.2.1 The semiclassical T-operator for Integrable Systems

It has been demonstrated by Lauritzen [28] that for a separable system with two freedoms, Bogomolny's semiclassical quantization condition becomes equivalent to EBK quantization in the limit $\hbar \to 0$. Hence, at relatively high energies, the semiclassical energy eigenstates obtained with Bogomolny's T-operator will have the same values as EBK energy eigenstates. This has been shown explicitly for the rectangular billiard by Lauritzen [28], and for the circle billiard by Boasman [6]. A consequence of the connection with EBK, is that one can write an analytic expression approximating the T-operator eigenvalue curves. This EBK form explicitly shows

the semiclassical unitarity of the T-operator [28] and provides an explanation for the relationship between eigenvalue curves and quantum numbers of integrable systems.

Consider the simplest case, a separable Hamiltonian system with two degrees of freedom described by the position coordinates (x,y). Choose a PSS along one of the coordinate axes, say the y-direction. In the limit $\hbar \to 0$, the T-operator takes the form [28]

$$T^{EBK}(y,y';E)=\sum_{n_y=0}^{n_{max}} \phi_{n_y}(y)\phi^*_{n_y}(y') \exp\left(\frac{i}{\hbar} I_x\left(E, I_y = 2\pi\hbar\left(n_y + \frac{\nu_y}{4}\right)\right) - \frac{i\nu_x\pi}{2}\right) \qquad (4.5)$$

where I_x and I_y are action variables, and n_y is the quantum number which, in the semiclassical limit, quantizes the action I_y. The variables ν_x and ν_y are phase indices which have been added to Lauritzen's expression [28] in agreement with EBK quantization. The sum in Eq. (4.5) is finite and n_{max} defines the maximum value of n_y. The basis function defined on the PSS, $\phi_{n_y}(y)$, is a particular linear combination (determined by the boundary conditions) of the EBK eigenfunctions [44],

$$\phi^{EBK}_{n_y}(y) = \frac{1}{(2\pi\hbar i)^{1/2}} \left|\frac{\delta^2 S_y(y,n_y)}{\delta n_y \delta y}\right|^{1/2} \exp\left(\pm\frac{i}{\hbar} S_y(y,n_y)\right), \qquad (4.6)$$

where $S_y(y,n_y)$ is the one dimensional action

$$S_y(y,n_y) = \int_{y_o}^{y} p_y\left(y', I_y = 2\pi\hbar\left(n_y + \frac{\nu_y}{4}\right)\right) dy'. \qquad (4.7)$$

It can easily be shown that the T-matrix corresponding to $T^{EBK}(y,y';E)$ is diagonal in the orthogonal basis $\{\phi_m(y)\}$ by substituting Eq.(4.5) into the usual definition for matrix elements:

$$\begin{aligned} T^{EBK}_{m,m'}(E) &= \int\int \phi^*_m(y) T^{EBK}(y,y';E)\phi_{m'}(y')\,\mathrm{d}y\,\mathrm{d}y' \\ &= \exp\left(\frac{i}{\hbar} I_x\left(E, I_y = 2\pi\hbar\left(n_y + \frac{\nu_y}{4}\right)\right) - \frac{i\nu_x\pi}{2}\right)\delta_{m,n_y}\delta_{m',n_y}. \end{aligned} \quad (4.8)$$

The diagonal elements of the T-matrix in Eq. (4.8) are the semiclassical T-operator eigenvalues

$$\lambda^{EBK}_{n_y}(E) = \exp\left(\frac{i}{\hbar} I_x\left(E, I_y = 2\pi\hbar\left(n_y + \frac{\nu_y}{4}\right)\right) - \frac{i\nu_x\pi}{2}\right). \quad (4.9)$$

Equation (4.9) clearly shows that each T-operator eigenvalue is associated with a particular quantum number n_y.

Due to the unitarity of the T-operator in the semiclassical limit, the T-operator eigenvalues defined by Eq. (4.9) must have unit modulus which implies that the action $I_x\left(E, I_y = 2\pi\hbar\left(n_y + \frac{\nu_y}{4}\right)\right)$ must be real. In the examples to be described later in this section, it will be seen that this sets a restriction on the values of n_y and that for a particular energy E, n_y may have integer values from 0 up to a maximum n_{max}. The maximum n_{max} implies that the sum in Eq. (4.5) is finite and the corresponding unitary semiclassical T-matrix has the dimension n_{max}. Also, the value of n_{max} increases as a function of energy, which means that an increasing number of T-operator eigenvalues are required to give the energy spectrum up to some energy E. The relationship between n_{max} and $N_p(E)$ will be shown.

The T-operator can be regarded as a semiclassical operator $\hat{T}^{EBK}(E)$ which acts on the eigenstates $\phi_{n_y}(y)$ defined on the PSS and has corresponding eigenvalues defined by Eq. (4.9). To construct the semiclassical T-matrix for a separable Hamiltonian system, one must compute the matrix elements

$$T^{EBK}_{\alpha\beta}(E) = \langle\alpha|\hat{T}^{EBK}(E)|\beta\rangle \tag{4.10}$$

where $\{|\alpha\rangle\}$ is the orthonormal basis consisting of the normalized EBK eigenstates of the separable Hamiltonian system defined on the PSS. In other words, if the PSS is chosen to be $x = C$, where C is a constant, the coordinate space representation of $|\alpha\rangle$ is given by $\langle x = C, y|\alpha\rangle = \langle x = C, y|n_x, n_y\rangle = \phi_{n_x}(x = C)\phi_{n_y}(y)$. Since the T-operator is diagonal with respect to $\phi_{n_y}(y)$, the T-matrix for the Hamiltonian system will be diagonal with respect to $|\alpha\rangle$ and have corresponding eigenvalues $\lambda^{EBK}_{\alpha}(E) = T^{EBK}_{\alpha\alpha}$. Bogomolny's semiclassical quantization condition is satisfied when

$$\mathrm{Im}(\lambda^{EBK}_{\alpha}(E)) = 0 \qquad \text{and} \qquad \mathrm{Re}(\lambda^{EBK}_{\alpha}(E)) = 1. \tag{4.11}$$

By imposing the conditions of Eq.(4.11) on the eigenvalues of the semiclassical T-operator, one obtains the EBK energy eigenstates. Also, $\lambda^{EBK}_{\alpha}(E)$ provides an approximation for the behaviour of the eigenvalue curves.

4.2.2 T-operator Eigenvalue Curves for the Circle Billiard

Boasman [6] gives an integral form for the T-operator eigenvalue curves of

the circle billiard and, by evaluating this integral with the method of stationary phase, he derives a semiclassical expression. He also outlines the EBK solution to the circle billiard (following Berry and Ozorio de Almeida [4]) and shows that the EBK energy eigenstates are equivalent to those obtained from the semiclassical T-operator eigenvalue curves. In this section, the same form for the semiclassical T-operator eigenvalue curves is derived, in the context of Lauritzen's general form. Also, the connection between the eigenvalue curves and quantum numbers is emphasized.

In Sec. 2.2 of Chap. 3, we derived an expression for the T-operator of the circle billiard. In this case, we chose the boundary at $r = R$ as the PSS and the coordinate q as the distance around the circumference from a chosen reference point. Combining Eqs. (1), (9) and (10) of Chap. 3, the T-operator takes the form:

$$T(q,q';E) = \frac{1}{\sqrt{2\pi i\hbar}}\sqrt{\frac{(2mE)^{1/2}}{2R}\sin\left(\frac{|q-q'|}{2R}\right)}\exp\left[\frac{i}{\hbar}\left(2R(2mE)^{\frac{1}{2}}\sin\left(\frac{|q-q'|}{2R}\right)-\pi\hbar\right)\right]. \quad (4.12)$$

With the coordinate transformation $q = R\theta$, Eq. (4.12) can be written in terms of the angular coordinate θ, indicating the angular position of q on the circular boundary. In this case, Eq. (4.12) becomes

$$T(\theta,\theta';E) = \frac{1}{\sqrt{2\pi i\hbar}}\sqrt{\frac{R(2mE)^{1/2}}{2}\sin\left(\frac{|\theta-\theta'|}{2}\right)}\exp\left[\frac{i}{\hbar}\left(2R(2mE)^{\frac{1}{2}}\sin\left(\frac{|\theta-\theta'|}{2}\right)-\pi\hbar\right)\right]. \quad (4.13)$$

Our goal is to show that, in the limit $\hbar \to 0$, the T-operator of Eq. (4.13) reduces to Lauritzen's form given by Eq. (4.5). We begin by finding the basis functions $\phi_{n_\theta}(\theta)$ defined on the PSS. For the circle billiard, the angular momentum is constant

(Appendix C) and, when quantized, is given by $p_\theta = n_\theta \hbar$. Consequently, the action for the angular coordinate is given by

$$S_\theta(\theta, n_\theta) = \int^\theta n_\theta \hbar \, d\theta' = n_\theta \hbar \theta \tag{4.14}$$

Substituting Eq. (4.14) into Eq. (4.6), the EBK eigenfunctions for the circle billiard become

$$\phi_{n_\theta}^{EBK}(\theta) = \frac{1}{\sqrt{2\pi i}} \exp(\pm i n_\theta \theta) \tag{4.15}$$

These eigenfunctions are equivalent to the exact quantum solutions (Appendix A). Since the only restriction on the basis eigenfunction $\phi_{n_\theta}(\theta)$ is that it be single valued (ie. the quantum number n_θ must be an integer), $\phi_{n_\theta}(\theta)$ consists of the linear combinations of $\phi_{n_\theta}^{EBK}(\theta)$, which are sine or cosine functions, given by

$$\phi_{n_\theta}(\theta) = \begin{cases} \frac{1}{\sqrt{2\pi}}, & n_\theta = 0 \\ \frac{1}{\sqrt{\pi}} \cos(n_\theta \theta), & n_\theta \neq 0 \\ \frac{1}{\sqrt{\pi}} \sin(n_\theta \theta), & n_\theta \neq 0 \end{cases}$$

To determine whether the T-matrix is diagonal in the basis $\phi_{n_\theta}(\theta)$, we can compute the T-matrix elements, using Eq. (4.8), defined by

$$T_{n_\theta, n'_\theta}^{EBK}(E) = \frac{1}{\sqrt{2\pi i \hbar}} \int_0^{2\pi} \int_0^{2\pi} \phi_{n_\theta}(\theta) T(\theta, \theta'; E) \phi_{n'_\theta}(\theta') \, d\theta \, d\theta'. \tag{4.16}$$

In the limit $\hbar \to 0$, the integrals in Eq. (4.16) can be evaluated using the stationary phase approximation. Consider the basis eigenfunction $\phi_{n_\theta}(\theta) = \cos(n_\theta \theta)/\sqrt{\pi}$ (the same derivation and result applies to the other basis functions). Then, Eq. (4.16)

becomes

$$T^{EBK}_{n_\theta,n'_\theta}(E) = \frac{1}{4\pi\sqrt{2\pi i\hbar}}\int_0^{2\pi}\int_0^{2\pi}\left[e^{-in_\theta\theta}T(\theta,\theta';E)e^{in'_\theta\theta'} + e^{-in_\theta\theta}T(\theta,\theta';E)e^{-in'_\theta\theta'}\right.$$
$$\left.+e^{in_\theta\theta}T(\theta,\theta';E)e^{in'_\theta\theta'} + e^{in_\theta\theta}T(\theta,\theta';E)e^{-in'_\theta\theta'}\right]\,d\theta\,d\theta'. \qquad (4.17)$$

Now, consider the integral with respect to θ. For the first term of Eq. (4.17), the main contribution to this integral comes from the points θ near the stationary point θ_0 for which

$$2R\sqrt{2mE}\frac{\partial}{\partial\theta}\left[\sin\left(\frac{\theta-\theta'}{2}\right)\right]\Big|_{\theta=\theta_0} - n_\theta\hbar = 0. \qquad (4.18)$$

The stationary point obtained from Eq. (4.18) is given by

$$\theta_0 = \theta' + 2\cos^{-1}\left(\frac{n_\theta\hbar}{\sqrt{2mE}R}\right). \qquad (4.19)$$

Carrying out the saddlepoint integration, the first term of Eq. (4.17) becomes

$$\int_0^{2\pi}\int_0^{2\pi} e^{-in_\theta\theta}T(\theta,\theta';E)e^{in'_\theta\theta'}\,d\theta\,d\theta' = \sqrt{2\pi i\hbar}e^{-\pi/2}$$
$$\times\exp\left[\frac{i}{\hbar}\left(2R\sqrt{2mE}\sqrt{1-\frac{n_\theta^2\hbar^2}{2mER^2}} - 2n_\theta\hbar\cos^{-1}\left(\frac{n_\theta\hbar}{\sqrt{2mE}R}\right) - \pi\hbar\right)\right]$$
$$\times\int_0^{2\pi} e^{\left[i(n_\theta-n'_\theta)\theta'\right]}\,d\theta'. \qquad (4.20)$$

The remaining integral, with respect to θ', is simply the kronecker delta function $\delta_{n_\theta,n'_\theta}$. Hence, the first term of Eq. (4.17) becomes

$$\int_0^{2\pi}\int_0^{2\pi} e^{-in_\theta\theta}T(\theta,\theta';E)e^{in'_\theta\theta'}\,d\theta\,d\theta' = 2\pi\sqrt{2\pi i\hbar}$$
$$\exp\left[\frac{i}{\hbar}\left(2R\sqrt{2mE}\sqrt{1-\frac{n_\theta^2\hbar^2}{2mER^2}} - 2n_\theta\hbar\cos^{-1}\left(\frac{n_\theta\hbar}{\sqrt{2mE}R}\right) - \frac{3\pi\hbar}{2}\right)\right]\delta_{n_\theta,n'_\theta} \quad (4.21)$$

The fourth term in Eq. (4.17) produces the same result as the first whereas, the second and third terms become zero since they involve the kronecker delta function $\delta_{n_\theta,-n'_\theta}$. Finally, we are left with

$$T^{EBK}_{n_\theta,n'_\theta}(E) = \exp\left[\frac{i}{\hbar}\left(2R\sqrt{2mE}\sqrt{1-\frac{n_\theta^2\hbar^2}{2mER^2}} - 2n_\theta\hbar\cos^{-1}\left(\frac{n_\theta\hbar}{\sqrt{2mE}R}\right) - \frac{3\pi\hbar}{2}\right)\right]\delta_{n_\theta,n'_\theta}. \quad (4.22)$$

Clearly, according to Eq. (4.22), the T-matrix is diagonal in the basis $\phi_{n_\theta}(\theta)$. In addition, the exponent involves the sum of the radial classical action (Eq. (C.4)),

$$I_r(E, I_\theta = 2\pi\hbar n_\theta) = 2R\sqrt{2mE}\sqrt{1-\frac{n_\theta^2\hbar^2}{2mER^2}} - 2n_\theta\hbar\cos^{-1}\left(\frac{n_\theta\hbar}{\sqrt{2mE}R}\right), \quad (4.23)$$

and a phase factor of $-3\pi\hbar/2$ (Appendix C). Hence, in the limit $\hbar \to 0$, the T-operator for the circle billiard can be expressed in Lauritzen's EBK form:

$$T^{EBK}(\theta,\theta') = \sum_{n_\theta=0}^{n_{max}} \phi_{n_\theta}(\theta)\phi^*_{n_\theta}(\theta')\exp\left(\frac{i}{\hbar}I_r(E, I_\theta = 2\pi\hbar n_\theta) - \frac{i3\pi}{2}\right). \quad (4.24)$$

The elements of the semiclassical T-matrix for the circle billiard are obtained from Eq.(4.10) where in this case, the EBK eigenfunctions are represented by $\langle r = R, \theta|n_r, n_\theta\rangle = \phi^{EBK}_{n_r}(r = R)\phi_{n_\theta}(\theta)$ (or equivalently, $|\alpha\rangle = |n_\theta\rangle$). Since we are dealing

with Dirichlet boundary conditions, the wavefunctions are zero along the circle billiard boundary at $r = R$. Consequently, $\phi_{n_r}^{EBK}(r = R) = 0$ and the EBK eigenfunctions $\phi_{n_r}^{EBK}(r = R)\phi_{n_\theta}(\theta)$ are zero along the PSS at $r = R$. However, technically, the PSS is an infinitesimal distance δr inside of the billiard boundary. Therefore, we are actually considering the EBK eigenfunctions $\phi_{n_r}^{EBK}(r = R + \delta r)\phi_{n_\theta}(\theta)$ which are not zero. The semiclassical T-operator eigenvalues are

$$\begin{aligned}
\lambda_\alpha^{EBK}(E) &= \langle \alpha' | \hat{T}^{EBK}(E) | \alpha \rangle \\
&= \langle n_\theta' | \hat{T}^{EBK}(E) | n_\theta \rangle \\
&= \exp\left(\frac{i}{\hbar} I_r(E, I_\theta = 2\pi\hbar n_\theta) - \frac{i3\pi}{2} \right) \delta_{n_\theta', n_\theta} \\
&= \lambda_{n_\theta}^{EBK}(E)
\end{aligned} \tag{4.25}$$

From Eq.(4.25), it is evident that each semiclassical T-operator eigenvalue curve is associated with a particular value of the quantum number n_θ corresponding to ν of the Bessel function (Appendix A). Also, the restriction that $I_r(E, I_\theta = 2\pi\hbar n_\theta)$ of Eq. (4.23) must be real sets the maximum value of n_θ as

$$n_{max} = \sqrt{\frac{2mER^2}{\hbar^2}}. \tag{4.26}$$

Equation (4.26) is half the value of $N_p(E) = 2R(2mE)^{\frac{1}{2}}/\hbar$ which estimates the number of Planck cells on the PSS that exist at energy E for the circle billiard (see Sec. 2.2 of Chap. 3). Since the semiclassical T-operator involves $2n_{max} + 1$ eigenstates at

energy E then, at high energies, n_{max} and $N_p(E)$ are in agreement.

It is important to emphasize that Eq. (4.26) can also be interpreted as the minimum energy $E_{min} = (n_\theta^2\hbar^2)/(2mR^2)$ for which a T-operator eigenvalue curve $\lambda_{n_\theta}^{EBK}(E)$ is defined. For energies $E < E_{min}$, the radial classical action $I_r(E, I_\theta = 2\pi\hbar n_\theta)$ is no longer real and consequently, the T-operator eigenvalue curve $\lambda_{n_\theta}^{EBK}(E)$ does not exist. Hence, the *spiral tails* of the T-operator eigenvalue curves, describing the way T-operator eigenvalues moved out from the origin to the unit circle, are not predicted by the EBK eigenvalue curves $\lambda_\alpha^{EBK}(E)$. However, an interesting connection is made between classical and quantum mechanics. The T-operator eigenvalue, associated with a particular quantum number n_θ, reaches the unit circle at the minimum energy E_{min} for which the corresponding classical motion, with momentum $p_\theta = n_\theta\hbar$, is allowed.

In an attempt to model the spiral tails of the T-operator eigenvalue curves $\lambda_{n_\theta}^{EBK}(E)$, I considered the complex action,

$$\tilde{I}_r(E, I_\theta = 2\pi\hbar n_\theta) = i2R\sqrt{2mE}\left[\sqrt{\frac{n_\theta^2\hbar^2}{2mER^2} - 1} - \frac{n_\theta\hbar}{\sqrt{2mE}}\ln\left(\frac{n_\theta\hbar}{\sqrt{2mE}R} + \sqrt{\frac{n_\theta^2\hbar^2}{2mER^2} - 1}\right)\right], \quad (4.27)$$

which is derived in the same manner as $I_r(E, I_\theta = 2\pi\hbar n_\theta)$ (Appendix C) however, with the complex momentum $\tilde{p}_r = \pm i\sqrt{2mE}\sqrt{\frac{n_\theta^2\hbar^2}{2mER^2} - 1}$. The resulting EBK eigenvalue curves are

$$\tilde{\lambda}_{n_\theta}^{EBK}(E) = \exp\left(\frac{1}{\hbar}\tilde{I}_r(E, I_\theta = 2\pi\hbar n_\theta) - \frac{i3\pi}{2}\right). \quad (4.28)$$

Equation (4.28) correctly models the increasing magnitude of the T-operator eigenvalue (from zero to one) but, fails to reproduce the spiral behaviour since $\tilde{\lambda}_{n_\theta}^{EBK}(E)$ does not rotate in the complex plane as a function of E (it simply moves out in straight line along the direction $\exp(-i3\pi/2)$).

Finally, the semiclassical energy eigenvalues of the circle billiard are obtained from the quantization condition (Eq. (4.11))

$$\frac{2\sqrt{2mE}}{\hbar}\left[\sqrt{R^2-\frac{(n_\theta\hbar)^2}{2mE}}-\frac{n_\theta\hbar}{\sqrt{2mE}}\cos^{-1}\left(\frac{n_\theta\hbar}{\sqrt{2mE}R}\right)\right]-\frac{i3\pi}{2}=2\pi n_r. \quad (4.29)$$

Eq. (4.29) shows that the first energy eigenvalue of the n_θ-eigenvalue curve corresponds to $n_r = 0$, while the next energy eigenvalue occurs when $n_r = 1$, and so on. The index n_r is therefore associated with the zeros of the Bessel function J_{n_θ}. Hence, each eigenvalue curve corresponds to a particular Bessel function and the energy eigenvalues lying on each curve are the zeros of this Bessel function.

In Fig. 4.4, the semiclassical T-operator eigenvalue curves $\mathrm{Im}(\lambda_\alpha^{EBK}(\tilde{E}))$ obtained from Eq. (4.25) are compared to the T-operator eigenvalue curves $\mathrm{Im}(\lambda_\alpha^{B}(\tilde{E}))$ constructed from the 50×50 T-matrix. The tails (dotted lines) attached to the T-operator eigenvalue curves $\mathrm{Im}(\lambda_\alpha^{EBK}(\tilde{E}))$ are the curves $\tilde{\lambda}_{n_\theta}^{EBK}(\tilde{E})$ of Eq. (4.28).

The most striking difference between the two types of curves is the range of values between which they oscillate. The EBK T-operator eigenvalue curves $\mathrm{Im}(\lambda_\alpha^{EBK}(\tilde{E}))$ oscillate strictly between the values of ± 1, reflecting the fact that they are derived from a unitary operator. In comparison, the T-operator eigenvalue

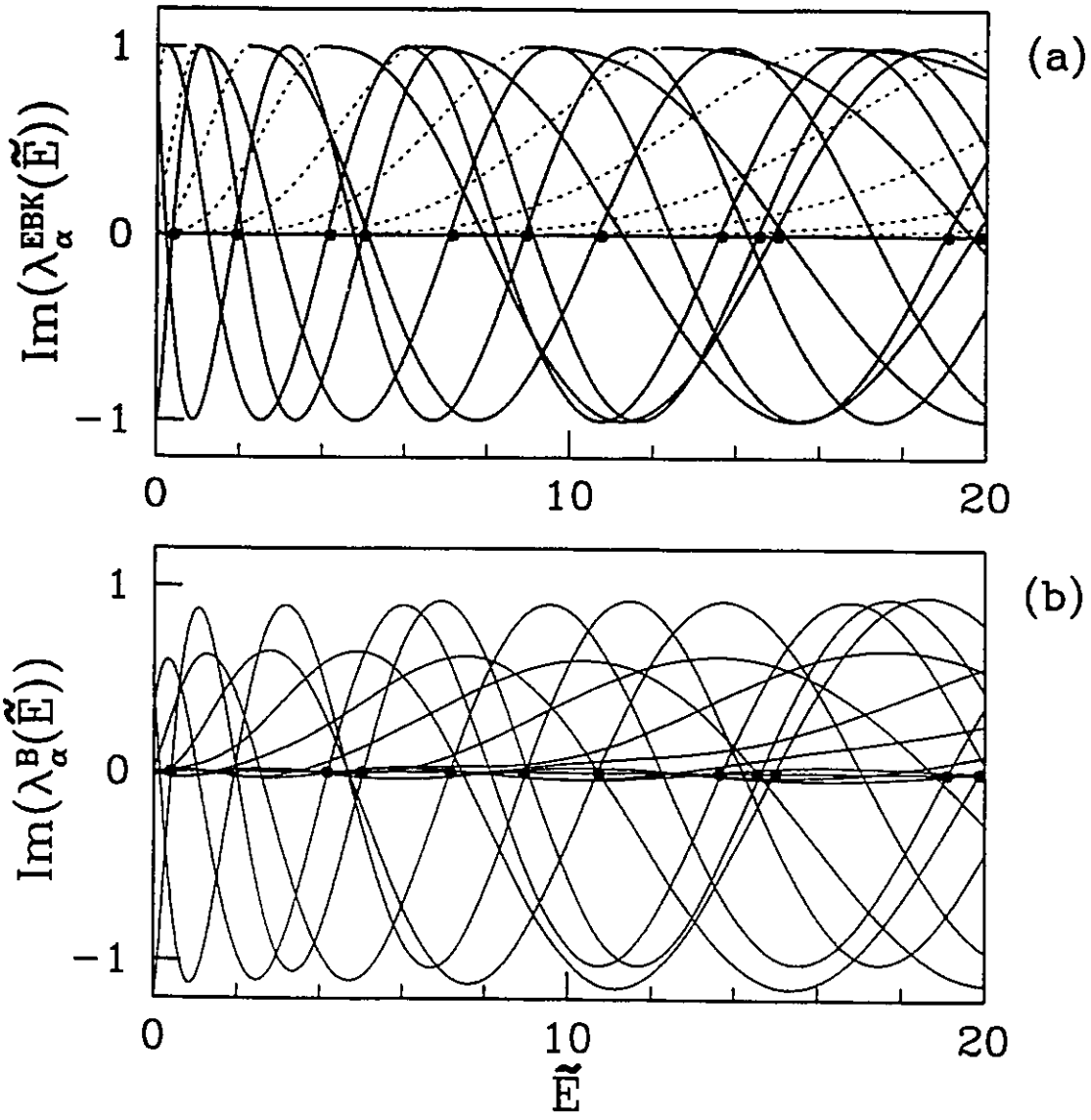

Figure 4.4: Comparison of semiclassical eigenvalue curves $\mathrm{Im}(\lambda_\alpha^{EBK}(\tilde{E}))$ (in (a) and (c)) with eigenvalue curves $\mathrm{Im}(\lambda_\alpha^{B}(\tilde{E}))$ (in (b) and (d)) constructed from the 50×50 T-matrix for the circle billiard. The dotted lines in (a) and (c) are the T-operator eigenvalue curves $\tilde{\lambda}_{n_\theta}^{EBK}(E)$ of Eq. (4.28). The circles drawn on the energy axis indicate the positions of the exact energy eigenstates. Although there are some differences between the two types of curves, more importantly, they link energy eigenstates in the same way.

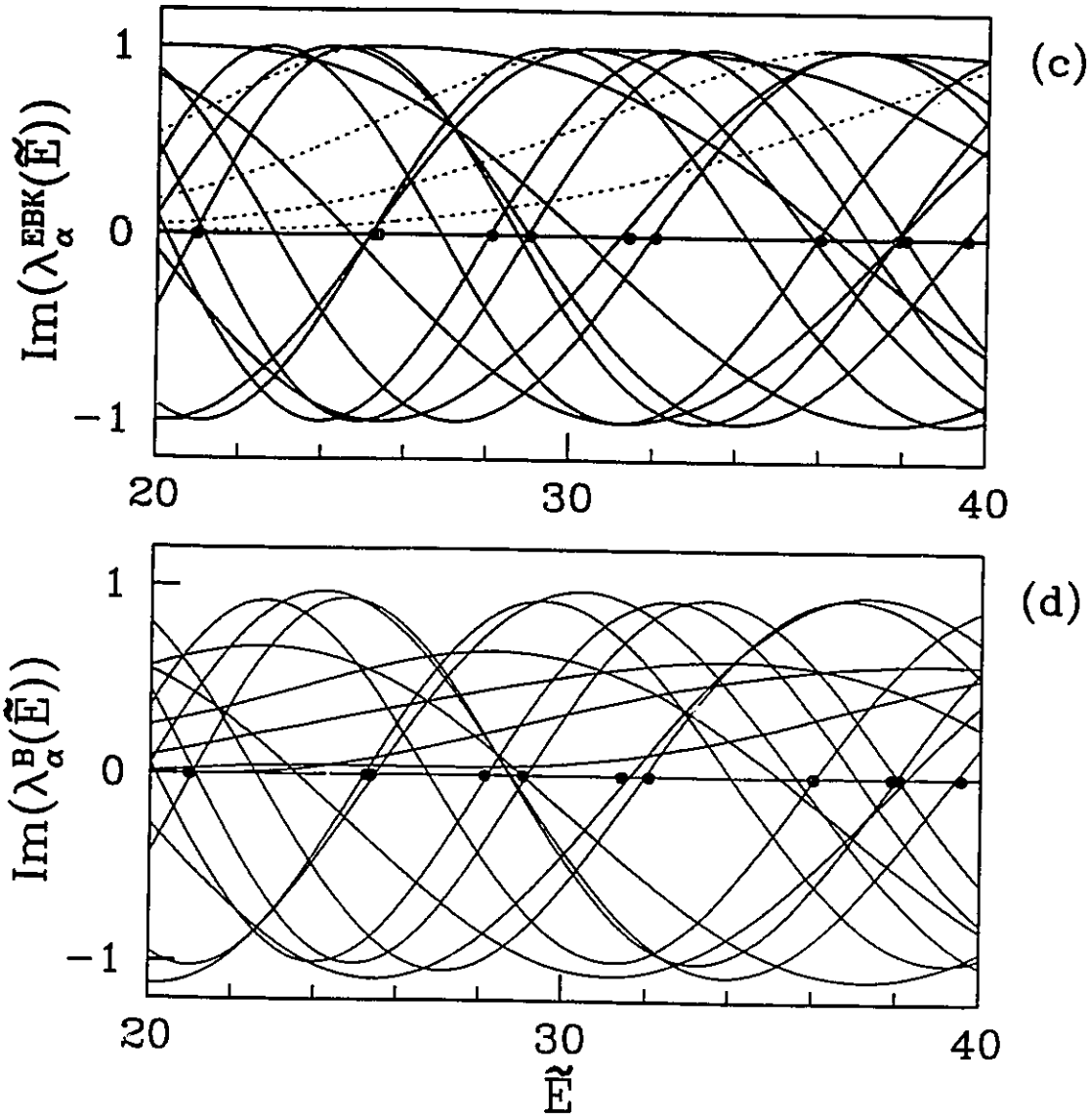

Figure 4.4: continued.

curves $\mathrm{Im}(\lambda_\alpha^B(\tilde{E}))$ are shifted down such that the maximums do not quite reach the value of 1 and the minimums surpass the value of -1. This shift is to be expected since the T-operator is not unitary at low energies. In fact, Boasman [6] was able to demonstrate, analytically, that Bogomolny's eigenvalue curves are shifted along the direction $\exp(-i\pi/4)$ from the unit circle in the complex plane. The convergence to unitarity is seen by following one particular curve. Gradually, with increasing energy, it moves towards values between ± 1. Eventually, in the limit $\hbar \to 0$, the eigenvalue curves $\mathrm{Im}(\lambda_\alpha^B(\tilde{E}))$ become identical to $\mathrm{Im}(\lambda_\alpha^{EBK}(\tilde{E}))$.

Another interesting observation is that in this range of energy, the T-operator eigenvalue curves $\mathrm{Im}(\lambda_\alpha^B(\tilde{E}))$ approximate the exact energy eigenstates better than the semiclassical eigenvalue curves $\mathrm{Im}(\lambda_\alpha^{EBK}(\tilde{E}))$. Again, this is not surprising since $\mathrm{Im}(\lambda_\alpha^{EBK}(\tilde{E}))$ is derived from $\mathrm{Im}(\lambda_\alpha^B(\tilde{E}))$ using a stationary phase approximation. Hence, at low energies, $\mathrm{Im}(\lambda_\alpha^{EBK}(\tilde{E}))$ approximate $\mathrm{Im}(\lambda_\alpha^B(\tilde{E}))$.

From Fig. 4.4, it can be seen that the magnitudes of the tails of the T-operator eigenvalue curves $\lambda_\alpha^B(\tilde{E})$ are properly estimated by those of $\tilde{\lambda}_\alpha^{EBK}(\tilde{E})$ (dotted line). However, the tails $\tilde{\lambda}_\alpha^{EBK}(\tilde{E})$ do not oscillate about the $\tilde{E}$-axis implying that they do not rotate around the origin like the those of $\lambda_\alpha^B(\tilde{E})$.

Despite these differences, the eigenvalue curves $\mathrm{Im}(\lambda_\alpha^B(\tilde{E}))$ and $\mathrm{Im}(\lambda_\alpha^{EBK}(\tilde{E}))$ are similar in the way that they locate the energy eigenstates. The energy eigenstates connected by one eigenvalue curve $\mathrm{Im}(\lambda_\alpha^B(\tilde{E}))$ are the same energy eigenstates connected by one eigenvalue curve $\mathrm{Im}(\lambda_\alpha^{EBK}(\tilde{E}))$. In this way, the semiclassical T-

operator eigenvalue curves yield the quantum numbers of integrable systems.

4.2.3 T-Operator Eigenvalue Curves for the 45° Wedge Billiard

Although the 45° wedge billiard is non-separable, it is an integrable system with two freedoms for which the T-operator can be written in Lauritzen's EBK form. However, to develop the EBK form for the T-operator of the 45° wedge billiard, we will first consider the 90° symmetric wedge billiard.

Recall from Sec. 2.3 of Chap. 3 that the 90° symmetric wedge billiard can be described by the XY-coordinate system running parallel to the walls of the billiard. Consider the straight line along one of the walls, say the X-coordinate, as the PSS. Referring to Eq.(4.5), to develop the EBK form for the T-operator, we need to express the classical action variable I_Y in terms of the total energy E and the quantized action variable $I_X = 2\pi\hbar(n_X + \nu_X/4)$. For the symmetric wedge billiard, the expressions for the classical actions I_X and I_Y are identical (Eq. (C.8) of Appendix C with $m = 1$ and $g = 1$);

$$I_X = \frac{8}{3}E_X^{3/2} \qquad \text{and} \qquad I_Y = \frac{8}{3}E_Y^{3/2}, \tag{4.30}$$

where E_X and E_Y are the energies for the X and Y motions respectively. The Maslov indices related to these action variables are $\nu_X = 3$ and $\nu_Y = 3$ (Appendix C). The action variables of Eq. (4.30) are related to each other using the total energy

$E = E_X + E_Y$. In addition, the EBK quantization of the action variable I_X (Appendix B) leads to the energy E_X of the form:

$$E_{n_X} = \left[\frac{3\pi\hbar}{4}\left(n_X + \frac{3}{4}\right)\right]^{2/3}. \tag{4.31}$$

Hence, combining Eqs. (4.30), (4.31) and the total energy relation, we obtain

$$I_X(E, n_Y) = \frac{8}{3}\left(E - \left[\frac{3\pi\hbar}{4}(n_Y + \frac{3}{4})\right]^{\frac{2}{3}}\right)^{\frac{3}{2}} \tag{4.32}$$

Consequently, the semiclassical T-operator for the 90° symmetric wedge billiard takes the form

$$T^{EBK}(X, X'; E) = \sum_{n_X=0}^{n_{max}} \phi_{n_X}(X)\phi^*_{n_X}(X')\exp\left(\frac{i}{\hbar}I_Y\left(E, I_X = 2\pi\hbar\left(n_X + \tfrac{3}{4}\right)\right) - \tfrac{i3\pi}{2}\right). \tag{4.33}$$

The basis eigenfunctions $\phi_{n_X}(X)$ are constructed from a linear combination of the EBK eigenfunctions $\phi^{EBK}_{n_X}(X)$ defined by Eq. (4.6). The action for the X-coordinate is given by

$$\begin{aligned} S_X(X, n_X) &= \int_0^X p_X(E_X, X)\mathrm{d}X = \int_0^X \sqrt{E_{n_X} - \frac{X}{\sqrt{2}}}\mathrm{d}X \\ &= \frac{4}{3}\left[E_{n_X}^{\frac{3}{2}} - (E_{n_X} - \frac{X}{\sqrt{2}})^{\frac{3}{2}}\right]. \end{aligned} \tag{4.34}$$

Substituting Eq. (4.34) into Eq. (4.6), the EBK eigenfunctions for the 90° wedge billiard become

$$\phi^{EBK}_{n_X}(X) = C\left(\frac{1}{2(E_X - \frac{X}{\sqrt{2}})}\right)^{\frac{1}{4}}\exp\left(-i\frac{4}{3\hbar}\left[E_{n_X}^{\frac{3}{2}} - (E_{n_X} - \frac{X}{\sqrt{2}})^{\frac{3}{2}}\right]\right) \tag{4.35}$$

Since we require that the wavefunction vanishes at the billiard boundary, the basis state $\phi_{n_X}(X)$ is the linear combination of these EBK eigenfunctions which gives a sine function.

What differentiates the 90° wedge billiard from the 45° wedge billiard, is the basis states $\{|\alpha\rangle\}$. For the 45° wedge, the energy eigenfunctions must vanish along the line $X = Y$ (to satisfy the boundary condition that the wavefunction vanishes along the vertical wall). This condition is achieved with the antisymmetric linear combination of the primitive wavefunctions $\phi_{n_1}(X)\phi_{n_2}(Y)$,

$$\begin{aligned}\Phi_\alpha(X,Y) &= A_{n_1,n_2}(\phi_{n_1}(X)\phi_{n_2}(Y) - \phi_{n_2}(X)\phi_{n_1}(Y)) \\ &= A_{n_1,n_2}(\langle X,Y|n_1,n_2\rangle - \langle X,Y|n_2,n_1\rangle)\,, \end{aligned} \tag{4.36}$$

where A_{n_1,n_2} is the normalization constant, equal to $\frac{1}{2}$ for $n_1 = n_2$ and $\frac{1}{\sqrt{2}}$ for $n_1 \neq n_2$. For the 90° wedge billiard, both the antisymmetric and symmetric linear combinations are allowed. In general, Eq.(4.36) is a nontrivial solution only when $n_1 \neq n_2$. Hence, the energy spectrum for the 45° wedge billiard consists of the energy eigenstates of the 90° wedge billiard with quantum numbers $n_1 \neq n_2$. Along the PSS, the energy eigenfunctions for the 45° wedge billiard are given by

$$\begin{aligned}\Phi_\alpha(X,Y=0) &= A_{n_1,n_2}(\langle X,Y=0|n_1,n_2\rangle - \langle X,Y=0|n_2,n_1\rangle) \\ &= A_{n_1,n_2}(C_{n_2}\langle X|n_1\rangle - C_{n_1}\langle X|n_2\rangle)\,, \end{aligned} \tag{4.37}$$

where $C_n = \phi_n(Y = 0)$ is a constant. As discussed in Sec. 4.2.2, the PSS is technically an infinitesimal distance δY from the billiard boundary. Hence, $C_n = \phi_n(Y = 0)$ is nonzero and the energy eigenfunctions of Eq. (4.37) are not zero. In addition, since the PSS is very close to the boundary, $C_{n_1} \approx C_{n_2}$.

Operating the semiclassical T-operator on the energy eigenfunctions Eq. (4.37) produces the result,

$$\hat{T}^{EBK}(E)|\alpha\rangle = A_{n_1,n_2}\left(C_{n_2}\exp(iI_X(E,n_1)/\hbar)|n_1\rangle - C_{n_1}\exp(iI_X(E,n_2)/\hbar)|n_2\rangle\right). \quad (4.38)$$

Setting $\alpha = n_2 - n_1$ with $n_2 > n_1$ (to avoid double counting) in Eq.(4.38), one obtains

$$\begin{aligned}\hat{T}^{EBK}(E)|\alpha\rangle = A_\alpha\,(&C_{\alpha+n_1}\exp(iI_X(E,n_1)/\hbar)|n_1\rangle \\ &-C_{n_1}\exp(iI_X(E,\alpha+n_1)/\hbar)|\alpha+n_1\rangle)\end{aligned} \quad (4.39)$$

Since $n_1 \neq n_2$ for the eigenstates of the 45° wedge billiard, $\alpha \geq 1$. Finally, the semiclassical T-operator eigenvalues are obtained by evaluating the matrix elements based on Eq. (4.10),

$$\begin{aligned}\lambda_\alpha^{EBK}(E) &= \langle\alpha'|\hat{T}^{EBK}(E)|\alpha\rangle \\ &= A_{\alpha'}A_\alpha\left[C_{\alpha'+n_1'}C_{\alpha+n_1}\exp(iI_X(E,n_1)/\hbar)\langle n_1'|n_1\rangle\right. \\ &\quad -C_{n_1'}C_{\alpha+n_1}\exp(iI_X(E,n_1)/\hbar)\langle\alpha'+n_1'|n_1\rangle \\ &\quad \left.-C_{\alpha'+n_1'}C_{n_1}\exp(iI_X(E,\alpha+n_1)/\hbar)\langle n_1'|\alpha+n_1\rangle\right.\end{aligned}$$

$$
\begin{aligned}
&+C_{n_1'}C_{n_1}\exp(iI_X(E,\alpha+n_1)/\hbar)\langle\alpha'+n_1'|\alpha+n_1\rangle\Big] \\
= \;& \frac{1}{2}\Big(C^2_{\alpha+n_1}\exp(iI_X(E,n_1)/\hbar) \\
&+C^2_{n_1}\exp(iI_X(E,\alpha+n_1)/\hbar)\Big)\,\delta_{n_1',n_1}\delta_{\alpha',\alpha},
\end{aligned}
\tag{4.40}
$$

where the energy E is determined by,

$$
E=\left(\frac{3\pi}{4}\left(\alpha+n_1+\frac{3}{4}\right)\right)^{\frac{2}{3}}+\left(\frac{3\pi}{4}\left(n_1+\frac{3}{4}\right)\right)^{\frac{2}{3}}. \tag{4.41}
$$

An interesting point that one draws from the final expression in Eq. (4.40) is that the semiclassical eigenvalue curves are associated with the difference in quantum numbers $\alpha = n_2 - n_1$ rather than a single quantum number n_1 or n_2. Also, keeping the integer α constant and varying the energy E forces the quantum number n_1 to vary according to Eq. (4.41). By substituting Eq. (4.41) into Eq. (4.40), $\lambda_\alpha^{EBK}(E) = \exp(2\pi n_1)$, and it becomes clear that Bogomolny's semiclassical quantization condition is satisfied for every integer value of n_1. Hence, the first energy eigenvalue encountered by a semiclassical eigenvalue curve has the quantum number $n_1 = 0$, the second one has $n_1 = 1$, and so on.

To recover the full solution for the 90° wedge billiard, the matrix elements are computed with the symmetric wavefunctions as well as the antisymmetric ones. The semiclassical T-operator eigenvalues calculated with the symmetric eigenstates are given by the same expression as Eq. (4.40) for indices $\alpha \geq 0$ (since $\alpha = 0$ is allowed for the symmetric eigenstates). Hence, for the 90° wedge billiard, there exists

one eigenvalue curve with index $\alpha = 0$ and two identical eigenvalue curves for every index $\alpha > 0$.

Fig. 4.5 is a comparison of the semiclassical eigenvalue curves $\mathrm{Im}(\lambda_\alpha^{EBK}(\tilde{E}))$ with the eigenvalue curves $\mathrm{Im}(\lambda_\alpha^{B}(\tilde{E}))$ of the 150 × 150 T-matrix. Since the T-operator is not unitary at low energies, the eigenvalue curves $\mathrm{Im}(\lambda_\alpha^{B}(\tilde{E}))$ do not oscillate strictly between the values of ± 1. Unlike the eigenvalue curves of the circle billiard, these eigenvalue curves are not obviously shifted in any preferential direction in the complex plane. Gradually, as the energy is increased, the eigenvalue curves $\mathrm{Im}(\lambda_\alpha^{B}(\tilde{E}))$ are expected to become identical to $\mathrm{Im}(\lambda_\alpha^{EBK}(\tilde{E}))$. For the reasons discussed in Sec. (4.2.2), the eigenvalue curves $\mathrm{Im}(\lambda_\alpha^{B}(\tilde{E}))$ approximate the exact energy eigenstates better than the semiclassical eigenvalue curves $\mathrm{Im}(\lambda_\alpha^{EBK}(\tilde{E}))$.

An unexpected result, demonstrated in Fig. 4.5, is that the eigenvalue curves $\mathrm{Im}(\lambda_\alpha^{B}(\tilde{E}))$ for the 45° wedge billiard do not always link energy eigenstates with the same quantum number α. There appear to be repulsions between T-operator eigenvalue curves $\mathrm{Im}(\lambda_\alpha^{B}(\tilde{E}))$ when certain T-operator eigenvalues approach each other in the complex plane. For example, near energy $\tilde{E} = 5$, the 3rd and 6th eigenvalue curves $\mathrm{Im}(\lambda_\alpha^{B}(\tilde{E}))$ (Fig. 4.5(b)) repel each other rather than crossing as the 3rd and 6th semiclassical eigenvalue curves $\mathrm{Im}(\lambda_\alpha^{EBK}(\tilde{E}))$ do (Fig. 4.5(a)). Consequently, the successive energy eigenstates located by the 3rd and 6th eigenvalue curves $\mathrm{Im}(\lambda_\alpha^{B}(\tilde{E}))$ are different from those obtained from the 3rd and 6th eigenvalue curves $\mathrm{Im}(\lambda_\alpha^{EBK}(\tilde{E}))$. The eigenvalue curve repulsions appear to be similar to energy

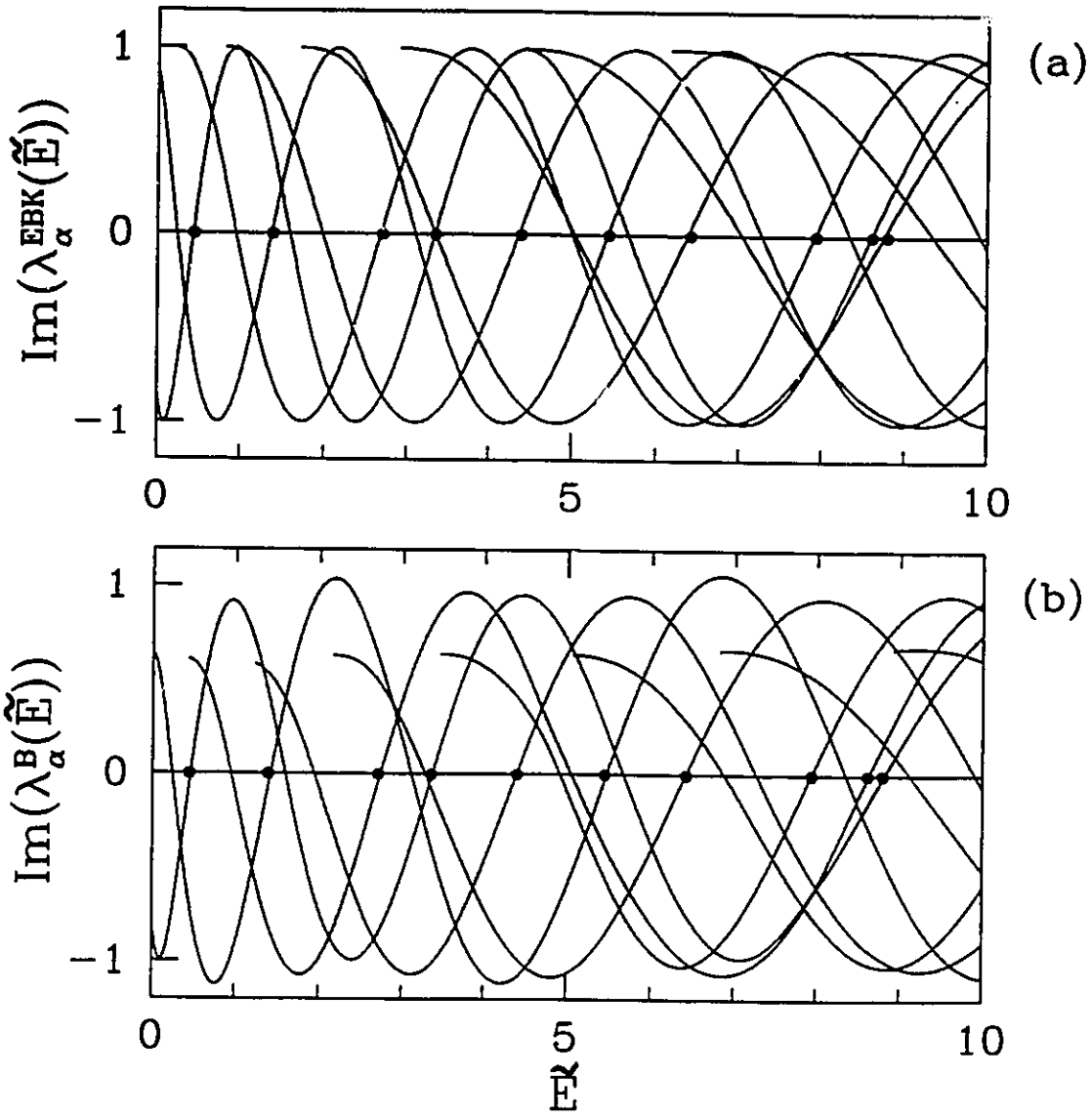

Figure 4.5: Comparison of semiclassical eigenvalue curves $\mathrm{Im}(\lambda_\alpha^{EBK}(\tilde{E}))$ (in (a) and (c)) with eigenvalue curves $\mathrm{Im}(\lambda_\alpha^{B}(\tilde{E}))$ (in (b) and (d)) from the 150×150 T-matrix for the 45° wedge billiard. The circles drawn on the energy axis indicate the positions of the exact energy eigenstates. The two types of eigenvalue curves do not link the same energy eigenstates. There appear to be repulsions between the eigenvalue curves $\mathrm{Im}(\lambda_\alpha^{B}(\tilde{E}))$.

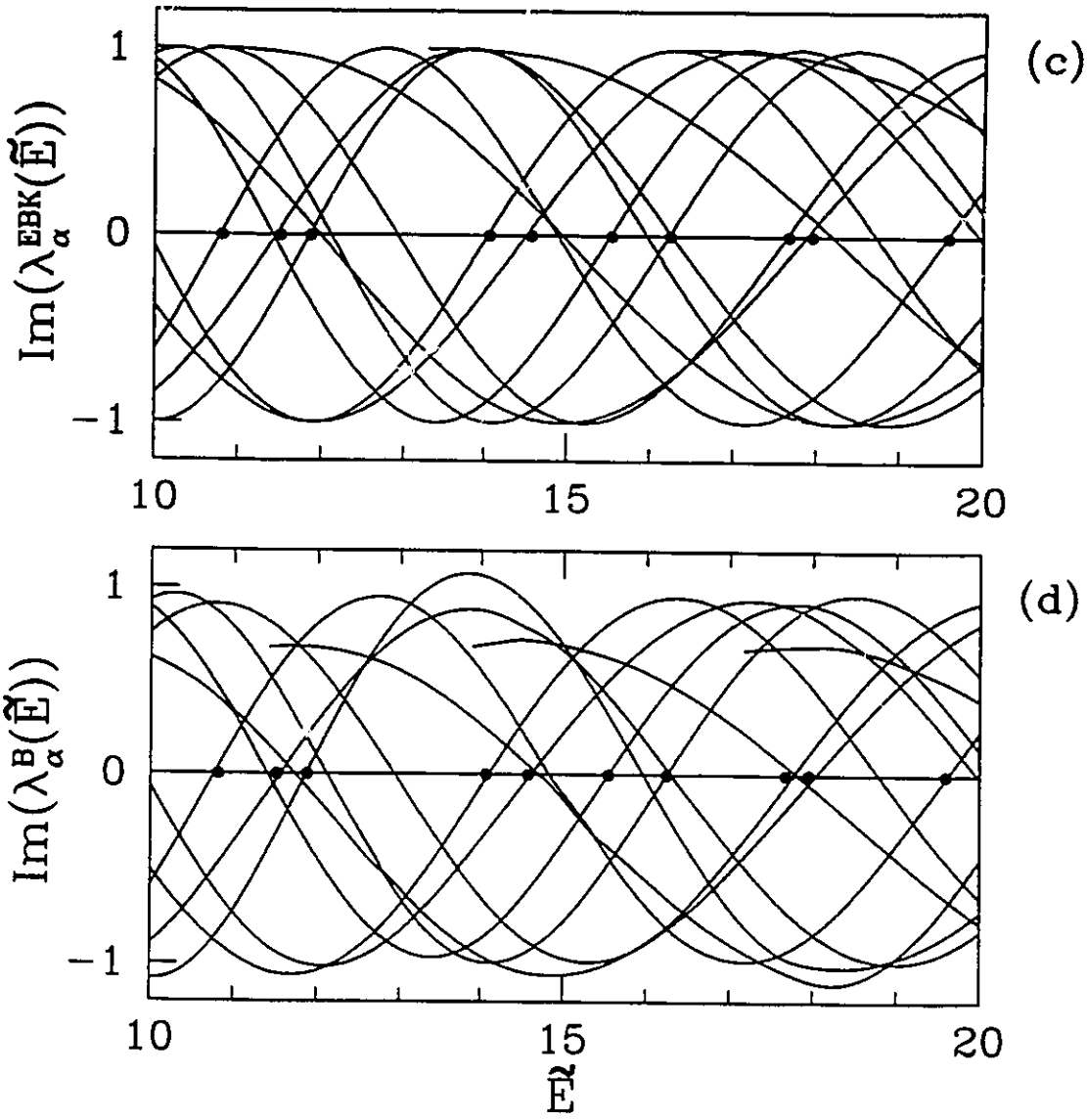

Figure 4.5: continued.

level avoided crossings. Other eigenvalue curve repulsions can be seen near energies $\tilde{E} \approx 8$ and $\tilde{E} \approx 11$ in Fig. 4.5.

Are the eigenvalue curve repulsions a *real* effect or a fabrication resulting from numerical inaccuracies? In other words, is the finite approximation to the T-operator responsible for these repulsions and is the connection between eigenvalue curves and quantum numbers only valid in the semiclassical limit? Fig. 4.6 is a comparison of the eigenvalue curves $\mathrm{Im}(\lambda_\alpha^{EBK}(\tilde{E}))$ of the 25×25 T-matrix with those from the 150×150 T-matrix (Figs. 4.5(b) and (d)). First of all, the programs used to compute the eigenvalue curves were written with double precision variables and the energy increment used in most calculations was $\Delta\tilde{E} = 0.01$. Hence, the differences between eigenvalue curves in Fig. 4.6 most likely result from the different T-matrix dimensions. While some of the T-operator eigenvalue curve repulsions observed for the 25×25 T-matrix become more pronounced for the 150×150 T-matrix (for example at $\tilde{E} \approx 5, 11 \mathrm{and} 17.5$), other repulsions diminish (like those at $\tilde{E} \approx 13 \mathrm{and} 15.5$). One would think that if the repulsions were artifacts caused by the finite approximations to the T-operator, that all the repulsions would diminish with an increase in matrix dimension, in contrast to what we have found. Futhermore, these results did not change with a further increase in matrix dimension to $N = 300$. Hence, one can only conclude that for this range of energy, the T-operator eigenvalue curves $\lambda_\alpha^B(\tilde{E})$ of the 45° wedge billiard do not correspond to particular quantum numbers. We do not understand why this happens.

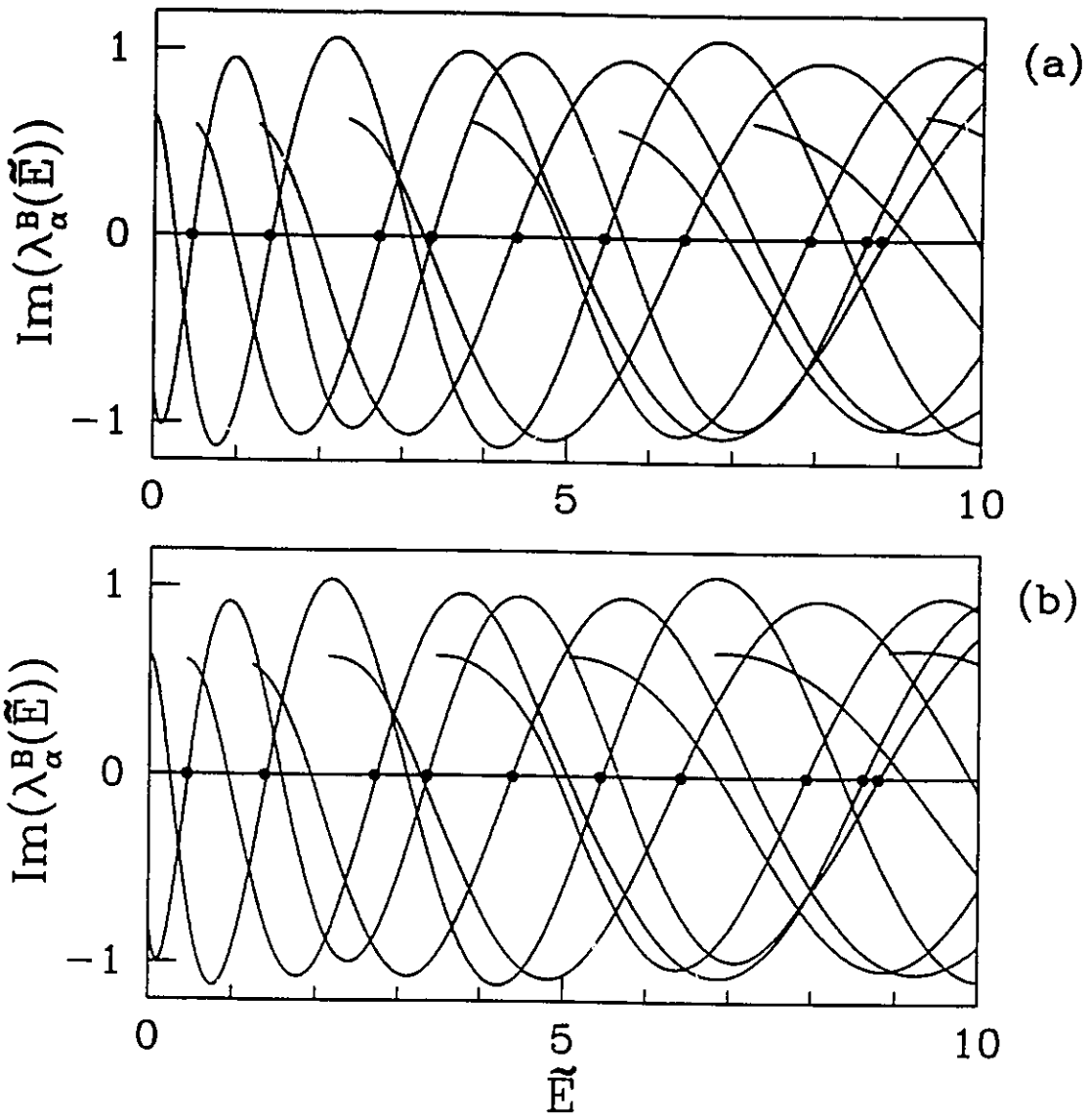

Figure 4.6: Comparison of T-operator eigenvalue curves $\mathrm{Im}(\lambda_\alpha^B(\tilde{E}))$ from the 25×25 T-matrix (in (a) and (c)) with those from the 150×150 T-matrix (in (b) and (d)) for the 45° wedge billiard. The circles drawn on the energy axis indicate the positions of the exact energy eigenstates. Some of the eigenvalue curve repulsions observed for the 25×25 T-matrix become more pronounced for the 150×150 T-matrix, while other repulsions diminish.

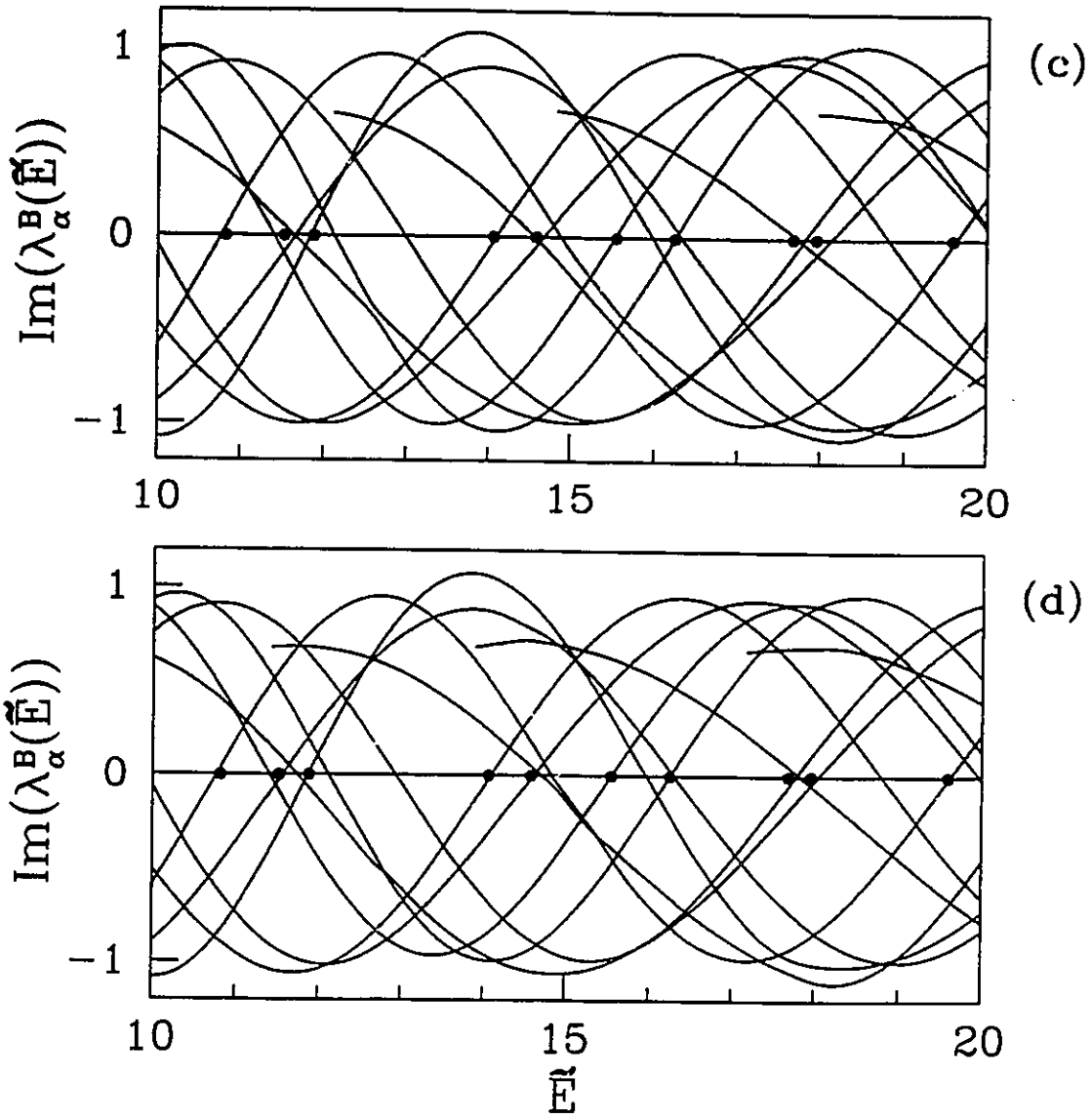

Figure 4.6: continued.

Generally, energy level repulsions occur between eigenstates with the same symmetry. Hence, at the avoided crossing of doubly degenerate energy levels, one expects that odd eigenstates will repel each other (or equivalently, the even eigenstates) but that an even and odd eigenstate will cross each other. Does this effect also occur in the 90° symmetric wedge billiard? The eigenvalue curves for the 150×150 T-matrix for the 90° symmetric wedge billiard are shown in Fig. 4.7. For the symmetric wedge billiard, the PSS is along the entire boundary. Hence, a T-matrix with dimension $N = 150$ has 75 divisions along each wall. The odd eigenvalue curves are identical to the ones obtained from the 45° wedge billiard. Most even eigenvalue curves obviously repel each other whenever odd eigenvalues curves avoid each other. For these energies, there are no instances where an odd and even eigenvalue curve interact with each other. This is consistent with symmetry arguments.

4.3 Distribution of T-Operator Eigenvalues

The main reason for studying the T-operator eigenvalue curves is to determine if they have distinguishing characteristics depending on the dynamical behaviour of the system (regular, chaotic or mixed). What prompted this investigation was the results of Haggerty [21] [22] showing that for the Nelson potential, there is a qualitative difference between the T-operator eigenvalue curves of the system in a "nearly regular" régime and those obtained for the system in a "mostly chaotic" régime. The

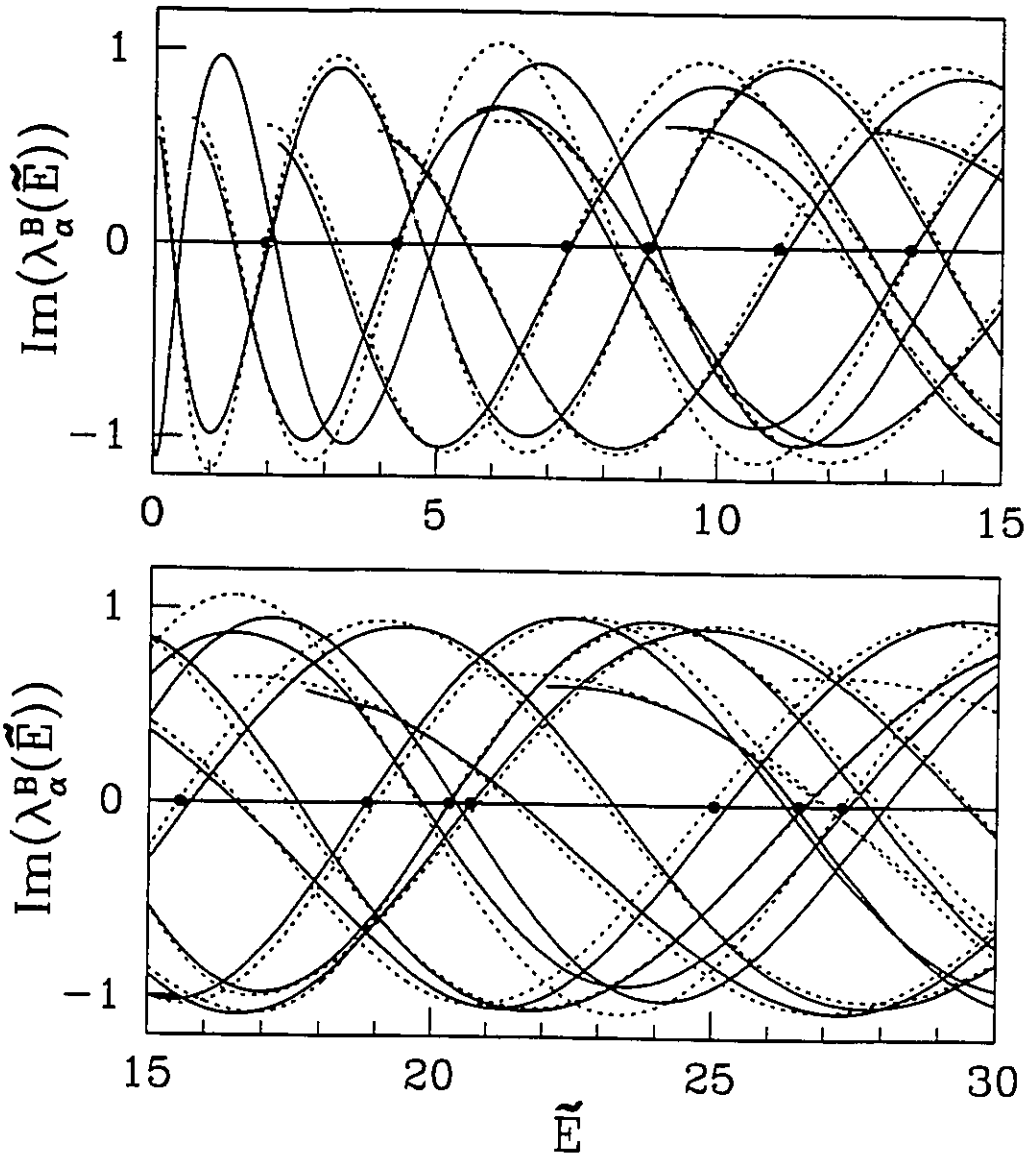

Figure 4.7: Eigenvalue curves $\mathrm{Im}(\lambda_\alpha^B(\tilde{E}))$ of the 150 × 150 T-matrix for the 90° symmetric wedge billiard. The circles drawn on the energy axis indicate the positions of the exact energy eigenstates. Some of the even and odd eigenvalue curves are represented by solid and dotted curves repectively to illustrate that repulsions only occur between eigenvalue curves of the same symmetry.

first dissimilarity is in the way that the T-operator eigenvalue curves spiral out from the origin to the unit circle in the complex plane. The T-operator eigenvalue curves of the "nearly regular" system spiral out significantly more gradually, making several more rotations around the origin, than those of the "mostly chaotic" régime. The second distinction is in the smoothness of the curves. T-operator eigenvalue curves of the "mostly chaotic" system are kinked, such that they avoid crossing each other, whenever they approach each other in the complex plane. On the other hand, T-operator eigenvalue curves of the "nearly regular" system are smooth and tend to cross each other. Could it be that T-operator eigenvalue curve repulsions (discussed in Sec. 4.2.3) is a trait of chaotic systems? Two questions that arise from these observations are: Are these qualitative differences generic? What happens to the T-operator eigenvalue curves in a régime of mixed behaviour?

Contrary to Haggerty's findings, Boasman [6] does not find any qualitative differences in the spirals of the circle, stadium and Africa billiards, despite the fact that these billiards are considerably different in their dynamical behaviour. He conjectures that the shape of the spiral near the origin reflects the 'local behaviour around each point of the boundary' rather than the global shape of the boundary determining the type of dynamical system. The global shape of the boundary is more likely reflected by the T-operator eigenvalue curves as they approach the unit circle [6]. Hence, billiards with similar smooth curved boundaries should have similar spirals near the origin but are not expected to be similar closer to the unit circle. This argu-

ment does not conflict with Haggerty's findings. Nevertheless, the spirals of the circle, stadium and Africa billiards look the same near and away from the origin, indicating that in these cases, the spiral nature of the T-operator eigenvalue curves does not give any indication of the type of dynamics. Could the different results of Haggerty and Boasman be related to the fact that in one case the systems are force-free billiards while in the other case the systems involve a smooth potential? While we will not be in a position to answer this question, we have studied the wedge billiard, a system which can display all three types of dynamical behaviour (regular, chaotic and mixed) and has aspects of a billiard (hard walls) and of a system with a smooth potential.

4.3.1 Spirals of T-operator Eigenvalue curves

Figure 4.8 compares the spiral behaviour of T-operator eigenvalue curves for the 45° wedge and 49° wedge billiards. In particular, each plot of Fig. 4.8 shows the distribution of 2300 T-operator eigenvalues with respect to the unit circle (solid line) in the complex plane. The T-operator eigenvalues were calculated from 10 matrices with dimensions between $N = 400$ and $N = 445$, and for the ratio $N/N_p(\grave{E}) = 2$. From Eq. (19) of Chap. 3, these T-operator eigenvalues correspond to relatively high scaled energies ranging from $\grave{E} \approx 5745$ to $\grave{E} \approx 7200$. The approximate unitarity of the T-operator, in this range of energy, can clearly be seen from the scatter of T-operator eigenvalues about the unit circle. The cluster of points at the origin are "subunitary" T-operator eigenvalues circling closely around the origin. In this region, there is

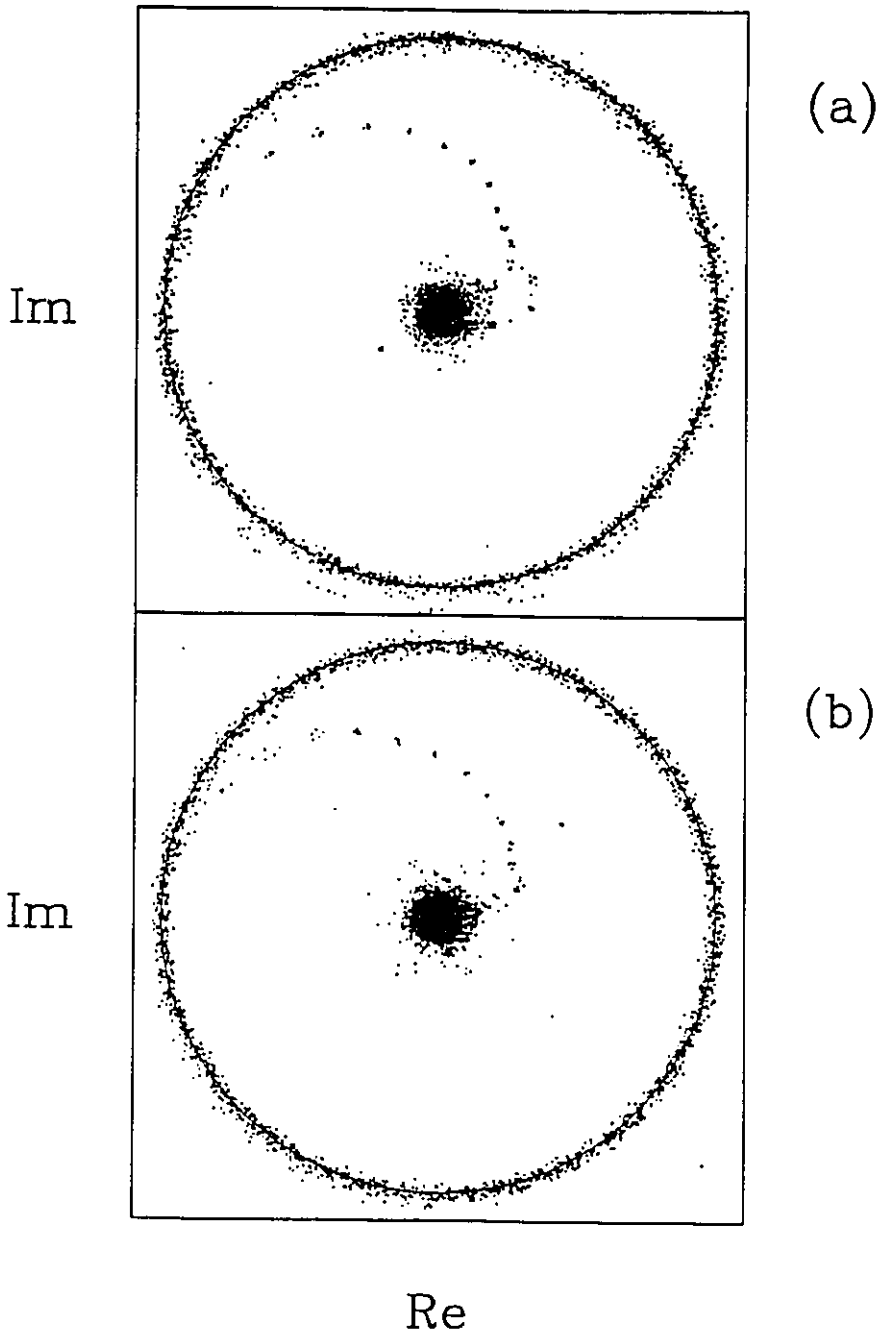

Figure 4.8: Comparison of the spiral pattern formed in the complex plane by the T-operator eigenvalues of: (a) the 45° wedge billiard (regular) and, (b) the 49° wedge billiard (chaotic). In both cases, the T-operator eigenvalues were obtained from 10 T-matrices with dimensions between $N = 400$ and $N = 445$, and with $N/N_p(\tilde{E}) = 2$. The solid line is the unit circle. The shapes of the spirals look similar and hence, do not reflect the nature of the dynamics.

no apparent trend in the movement of T-operator eigenvalues, whereas, further away from the origin, the T-operator eigenvalues line up along a spiral direction. The shape of the spirals and the angles at which they approach the unit circle are qualitatively the same for both wedge angles. Similar results were found for the 30° and 60° wedge billiards. Hence, it appears that for the wedge billiard, the form of the spiral gives no indication about the type of dynamical system.

4.3.2 Repulsions of T-operator Eigenvalue curves

In this section, we investigate the possibility that T-operator eigenvalue curves repel each other more frequently in chaotic systems than in regular systems. Such a result would identify a new feature associated with chaos in a quantum systems and could conceivably be used to interpret the energy spectra of systems with mixed behaviour. It was proposed by Percival [33] that, for systems exhibiting soft chaos in the classical regime, the energy eigenvalues of the analogous quantum system can be divided into a regular part (associated with the regular behaviour of the classical system) and an irregular part (associated with the chaotic motion in the classical system). This separation has been successfully demonstrated by Bohigas *et al.* [14] who studied the two coupled quartic oscillators. In terms of the distribution of T-operator eigenvalues, one should find more repulsions (i.e. more even distribution of T-operator eigenvalues on the unit circle) at energies corresponding to irregular energy eigenvalues than at energies close to regular energy eigenvalues.

Figure (4.9) shows the distribution of T-operator eigenvalues in the complex plane for the 45° and 49° wedge billiards at one particular scaled energy $\hat{E}$. In both cases, the T-operator eigenvalues were calculated from a 445×445 T-matrix and with the ratio $N/N_p(\hat{E}) = 2$. As examples we chose $\hat{E} \approx 7127$ for the 45° wedge and $\hat{E} \approx 7195$ for the 49° wedge. Considering only the T-operator eigenvalues on the the unit circle in Fig. (4.9), there appears to be more clustering for the 45° wedge, resulting in larger gaps between some of the T-operator eigenvalues, whereas for the 49° wedge the eigenvalues seem to be more evenly spread. This observation, in agreement with Haggerty, suggests that repulsions between T-operator eigenvalue curves are more likely to occur for chaotic systems than for regular systems.

To quantify this result, we calculated the angular differences Δ_θ between nearest neighbour T-operator eigenvalues on the unit circle. These values were normalized by dividing them by the average angular spacing between $N_p(\hat{E})$ nearest neighbours on the unit circle given by the simple expression $\overline{\Delta} = 2\pi/N_p(\hat{E})$. With 445×445 T-matrices and $N/N_p(\hat{E}) = 2$, approximately 223 T-operator eigenvalues lie on the unit circle and this is not a relatively large sample from which one can obtain reliable statistics. To overcome this problem, the nearest neighbour spacings from 19 T-matrices with dimensions between $N = 355$ and $N = 445$ (the same ones used in Sec. 4.3.1) were binned together. This way we increased our sample of normalized nearest neighbour spacings to approximately 3800, improving the statistics considerably. The histograms constructed from 3800 normalized nearest neighbour

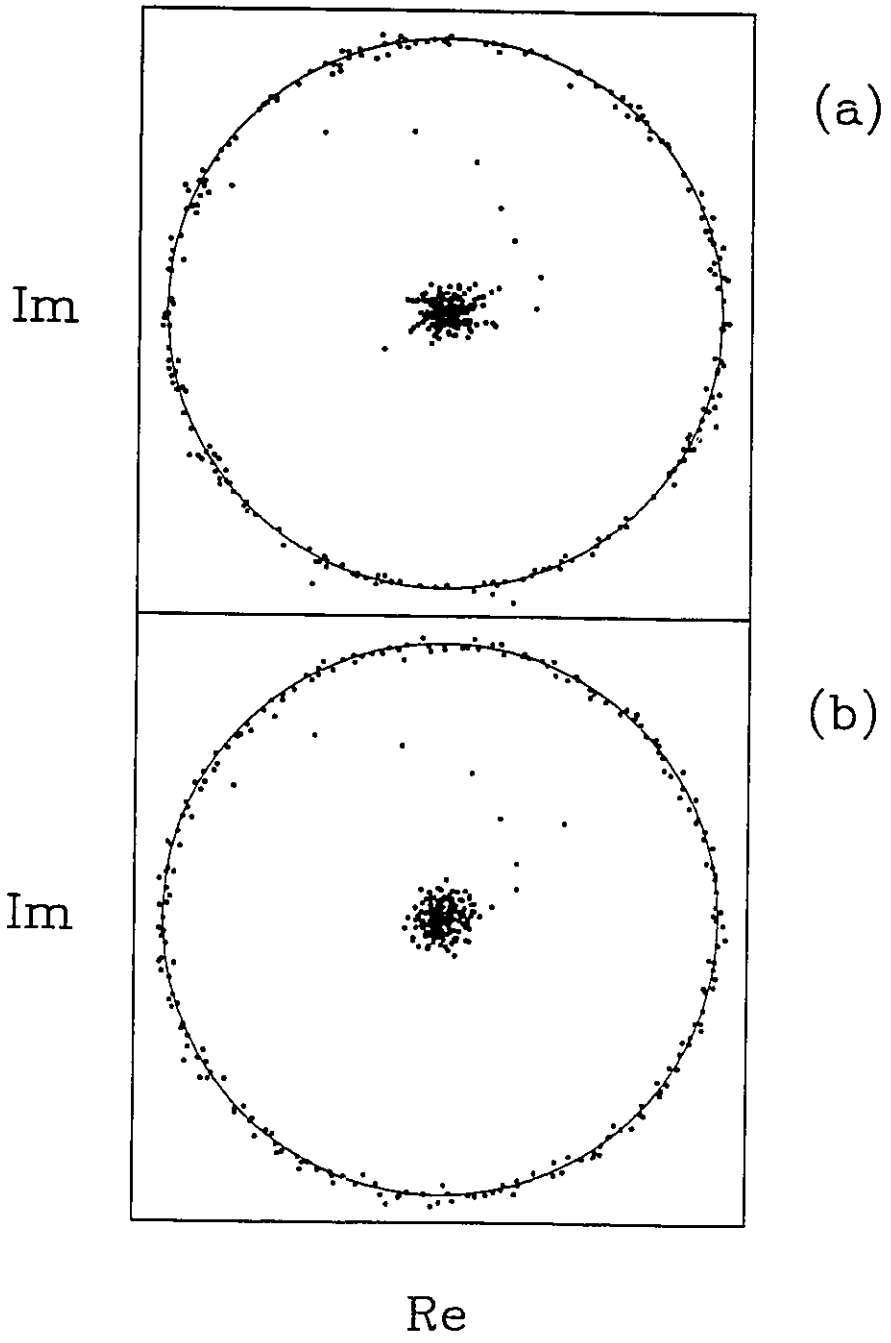

Figure 4.9: Distribution in the complex plane of the T-operator eigenvalues for: (a) the 45° wedge billiard (regular) and (b) the 49° wedge billiard. The T-operator eigenvalues were obtained from one T-matrix with dimension $N = 445$, and for $N/N_p(\tilde{E}) = 2$. The solid line is the unit circle. The T-operator eigenvalues on the unit circle in (a) are more clustered than those in (b).

spacings for the 45° and 49° wedge billiards are shown in Fig. 4.10(a). The histograms were normalized to give the probability density $P(\Delta_\theta/\overline{\Delta}_\theta)$. Figure 4.10(b) displays the cumulative distribution functions for the histograms of Fig. 4.10(a). There are definitely more T-operator eigenvalue repulsions for the 49° wedge than for the 45° wedge.

The histograms in Fig. 4.10 (a) appear to follow the same distributions (solid and dotted curves overlayed on the histograms) expected for the energy level spacings [13] [12]. The energy level spacing distribution of integrable systems is expected to follow the Poisson distribution given by

$$P(x) = \exp(-x) \tag{4.42}$$

whereas for chaotic systems with time reversal symmetry, the energy level spacing distribution is expected to follow the Wigner distribution:

$$P(x) = \frac{\pi}{2} x \exp\left(-\frac{\pi}{4} x^2\right). \tag{4.43}$$

These conclusions are supported by the recent findings of Rouvinez [37]. Rouvinez [37] has applied the scattering approach to the wedge billiard and has shown that the phase spacing distribution for the eigenvalues of the S matrices are well represented by the Poisson distribution (Eq. (4.42)) for the 45° wedge and by a Wigner distribution (Eq. (4.43)) for the 60° wedge. The connection between the distributions of energy level spacings and S matrix eigenvalue phase spacings is made through a formula

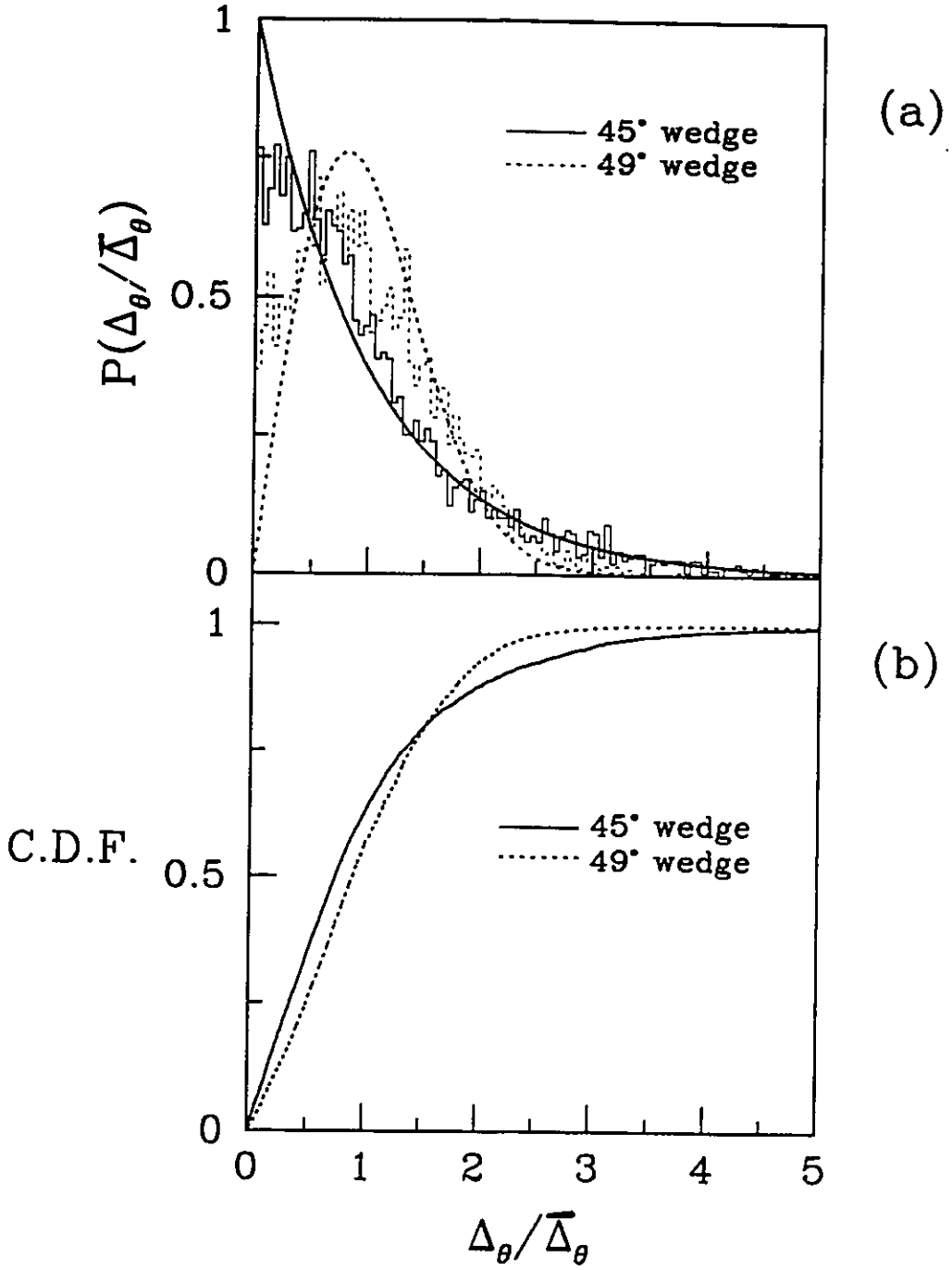

Figure 4.10: Quantitative analysis of the distribution of T-operator eigenvalue phases for the 45° (solid line) and the 49° (dotted line) wedge billiards. (a) Probability $P(s)$ of normalized T-operator eigenvalue phase spacings per bin of width 0.05. The curves overlayed on top of the distributions are the theoretical expectations. (b) Cumulative distribution functions (C.D.F.) of the normalized T-operator eigenvalue spacings for the histograms in (a). The normalized T-operator eigenvalue spacings were calculated from 19 T-matrices.

which relates the density of states and the phase velocities (Eq. (4.29) of [37]). Since it has been shown by Prosen [34] that the scattering approach reduces to Bogomolny's theory in the semiclassical limit, the findings of Rouvinez are comparable to ours.

In Fig. 4.11, the distributions for the 45° and 49° wedge billiards are compared to that of the 41° wedge (constructed from 19 T-matrices as described in the above paragraph). Technically, for the 41° wedge billiard, the distributions of T-operator eigenvalues obtained at different energies should not be binned together since we lose information about whether particular energies belong to the regular or irregular part. However, combining them should simply average the regular and chaotic distributions and produce a distribution intermediate to those of the regular and chaotic cases [5].

To investigate Percival's conjecture, one needs to study the distribution of T-operator eigenvalues at particular energy eigenvalues of the system. Unfortunately, the number of T-operator eigenvalues on the unit circle at a particular energy $\tilde{E}$ is limited by $N_p(\tilde{E})$. Consequently, the only way to obtain a large number of T-operator eigenvalues (for reasonably good statistics) is to consider very high energies and consequently, very large T-matrices. The minimum T-matrix dimension required at an energy $\tilde{E}$ is $N = N_p(\tilde{E})$ (equivalent to the ratio $N/N_p(\tilde{E}) = 1$). However, as discussed in Sec. 2.3.1 of Chap. 3, the uncertainties caused by finite approximations are reduced by increasing the ratio $N/N_p(\tilde{E})$ implying a further increase in the T-matrix dimension N. For example, suppose that for reasonably good statistics, we need a sample size of approximately 500. Then, at the minimum, the T-matrix

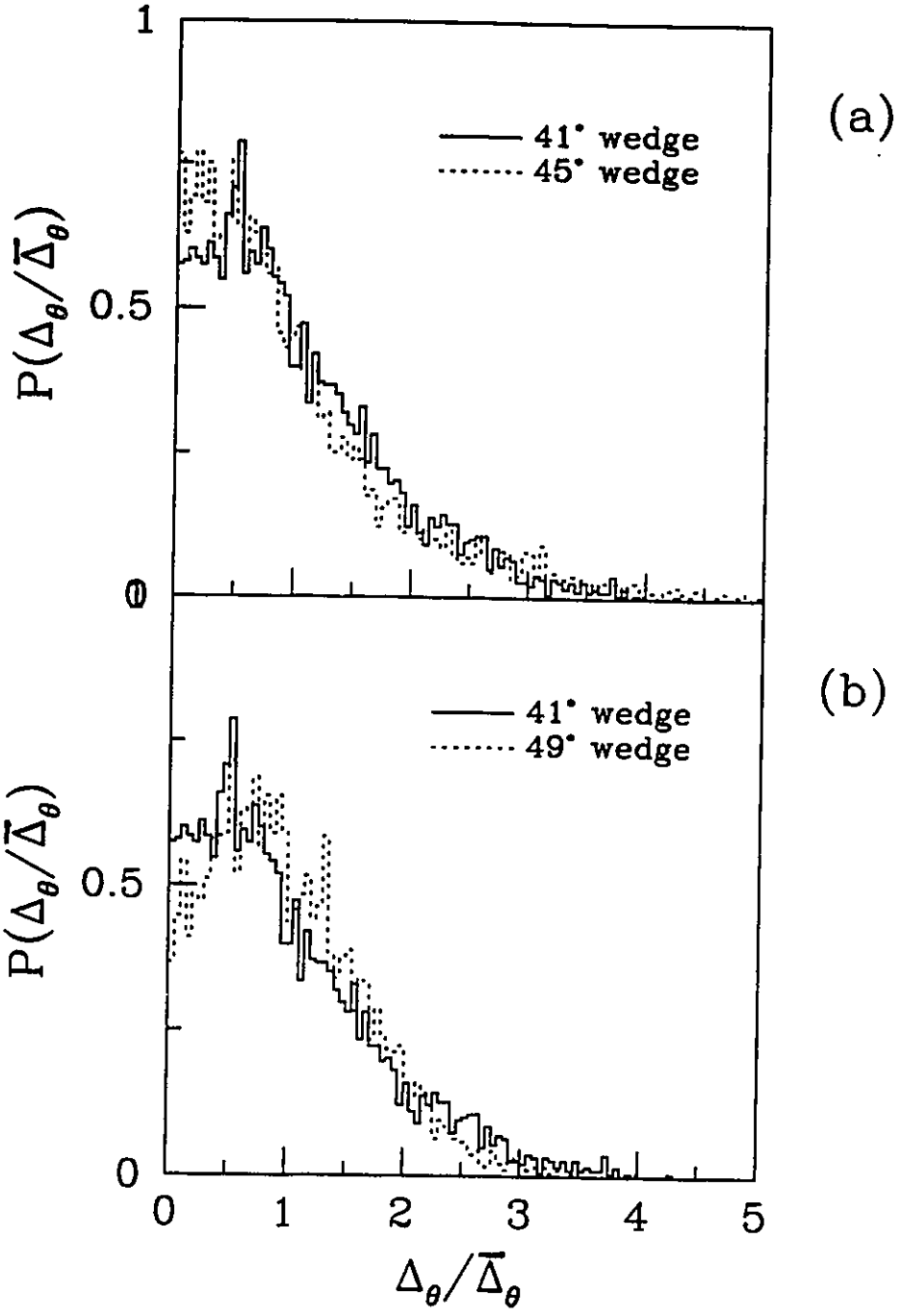

Figure 4.11: Comparison of the distributions of T-operator eigenvalues for: (a) the 45° wedge (regular) and, (b) 49° wedge (chaotic) with the 41° wedge (mixed).

dimension should be $N = 500$ and, to improve the accuracy of the normalized nearest neighbour spacings, N should be increased to even higher values (ideally up to at least $N/N_p(\tilde{E}) = 10$). It is evident that quickly, we are limited by the size of the T-matrix dimension and, as a result, this method would not make a practical way to classify energy eigenstates of systems with mixed behaviour. However, regardless of the limitations caused by the size of T-matrices, it would be worth studying, in more detail, if there exists a correlation between T-operator eigenvalue distributions and the energy eigenvalues of mixed systems. One way to proceed would involve adapting the technique developed by Bohigas et al. to the wedge billiard, to identify the energy eigenvalues that belong to either the regular or irregular part of the energy spectra. Then, the results could be compared with the energy eigenstates which have been classified independently according to the normalized nearest neighbour distribution of T-operator eigenvalues. It would be of fundamental importance if the two methods yielded consistent results.

Chapter 5

Wavefunctions from the T-Operator

In the previous chapters, the emphasis has been on the semiclasscial energy eigenvalues calculated from Bogomolny's T-operator method. In this chapter, we turn our attention to semiclassical wavefunctions and explore the capabilities of Bogomolny's T-operator method with respect to determining energy eigenfunctions. The energy eigenfunctions are constructed from the eigenfunctions of the T-operator defined on the PSS, and for this reason, one would expect that the T-operator eigenfunctions reflect properties of the system. In his thesis, Haggerty [21] presents a picture gallery of T-operator eigenfunctions on the PSS for the Nelson potential and discusses their relation to the exact energy eigenfunctions of the system. To date, no other study related to energy eigenfunctions obtained from the T-operator method has been published.

There exist two other semiclassical techniques for estimating energy eigenfunctions of general Hamiltonian systems (integrable and nonintegrable). In the en-

ergy domain, apart from the WKB approximation method (Appendix B) applying only to integrable systems, there is the scattering matrix method of Doron and Smilansky [15]. This method, which is closely related to Bogomolny's T-operator method, has been applied to the wedge billiard by Rouvinez and Smilansky[36] and Rouvinez [37]. Tomsovic and Heller [43] extract energy eigenstates for the stadium billiard from a wave-packet propagated in the time domain. Provost and Brumer [35] demonstrate the success of this method applied to a smooth chaotic system.

Other work on semiclassical wavefunctions has focussed on energy-averaged functions, not individual eigenstates, since it has been found that energy-averaged coordinate space wavefunctions are localized in the vicinity of short unstable periodic orbits (a phenomena studied and named *scarring* by Heller [23]). Individual states have contributions from many periodic orbits (Aurich and Steiner [2]). A theoretical explanation for this scarring phenomena, based on periodic orbit theory, has been provided by Berry [3] and Bogomolny [8]. In a similar way, the T-operator eigenfunctions depend on several classical trajectories and Haggerty [21] [22] has shown how to recover the actions of the trajectories which contribute to a T-operator eigenfunction. Readers are referred to a paper by Meredith [30] for an excellent review of current progress on studies of semiclassical wavefunctions.

In Sec. 5.1, we outline the general procedure for calculating semiclassical energy eigenfunctions using Bogomolny's T-operator method. In Secs. 5.2 and 5.3, this method is applied to the circle and wedge billiards. The success of this method is

evaluated in a qualitative fashion by comparing the results to exact quantum solutions. For the integrable cases, the wavefunctions are also compared to the WKB wavefunctions.

5.1 The General Relation

Analogous to the association between the T-operator eigenvalues and the energy eigenvalues of the system, there exists a correspondence between T-operator eigenfunctions, defined by Eq. (1.5), and the energy eigenfunctions of the system. At an energy $E = E_n$ satisfying Bogomolny's semiclassical quantization condition, the T-operator has en eigenvalue equal to one and an associated eigenfunction $\psi_n(q)$ defined on the PSS. This particular T-operator eigenfunction describes the dependence of the energy eigenfunction $\Psi_n(\vec{x})$ on the coordinate q along the PSS. In this way, the T-operator eigenfunctions reflect properties of the energy eigenfunctions of the system.

The coordinate-space energy eigenfunctions $\Psi_n(\vec{x})$ can be recovered from the T-operator eigenfunctions $\psi_n(q)$ defined on the PSS using the relation [10]

$$\Psi_n(\vec{x}) = \int_\Sigma G(\vec{x}, q; E_n)\psi_n(q)\, dq, \tag{5.1}$$

where $G(\vec{x}, q; E)$ is a semiclassical propagator given by

$$\begin{aligned} G(\vec{x}, q; E_n) &= \frac{1}{(-i\hbar)^{1/2}(2\pi i\hbar)^{1/2}} \sum_{c.l.} \left| \frac{1}{|\vec{p}(\vec{x})|} \det\left(\frac{\partial^2 S(\vec{x}, q; E_n)}{\partial \eta \partial q} \right) \right|^{\frac{1}{2}} \\ &\quad \times \exp\left(\frac{i}{\hbar} S(\vec{x}, q; E_n) - \frac{i\pi}{2}\nu \right). \end{aligned} \tag{5.2}$$

In Eq. (5.2), the summation is taken over all classical trajectories that connect a point q on the PSS to a point $\vec{x}$ in the allowed region of motion in coordinate space (and which do not come back and re-cross the PSS), $S(\vec{x}, q; E_n)$ is the classical action for these trajectories and ν is the related phase index whose value depends on the number of points where the semiclassical approximation breaks down (see Eq. 4.22 of Bogomolny [10]). The coordinate η is in the plane perpendicular to the classical trajectory at point $\vec{x}$, and $|\vec{p}(\vec{x})|$ is the magnitude of the momentum at point $\vec{x}$. In this study, we are only dealing with two-dimensional systems, and in this case, the determinant in Eq. (5.2) simply involves one term. A general expression for the partial derivative with respect to the coordinate η perpendicular to a trajectory at a point $\vec{x} = (x, y)$ is derived in Appendix D. From Eq. (D.6), the second derivative of Eq. (5.2) becomes

$$\frac{\partial^2 S(\vec{x}, q; E_n)}{\partial \eta \partial q} = \frac{1}{|\vec{p}(\vec{x})|} \left(p_y \frac{\partial^2 S(\vec{x}, q; E_n)}{\partial x \partial q} - p_x \frac{\partial^2 S(\vec{x}, q; E_n)}{\partial y \partial q} \right). \tag{5.3}$$

5.1.1 Numerical Computations

For the systems discussed in this study, we have chosen to construct the energy eigenfunctions numerically from the finite T-operator. The first major step involves finding the semiclassical energy eigenvalues of the system by the methods described in Chaps. 3 and 4. Then, for a particular energy eigenvalue E_n, we construct

the T-matrix in the usual fashion and numerically diagonalize it. The T-operator eigenfunction $\psi_n(q)$ corresponding to the T-operator eigenvalue closest to 1 is the appropriate function which gives the value of the energy eigenfunction $\Psi_n(\vec{x})$ along the PSS.

Since we are dealing with the finite form of the T-operator, $\psi_n(q)$ is a piecewise constant function which has an amplitude

$$\psi_n(q_m) = \frac{c_m}{\sqrt{\Delta_m}} \tag{5.4}$$

for the cell centred at q_m of width Δ_m. The constants c_m, which are generally complex, are the values obtained from the diagonalized T-matrix. Hence, if one wants to compare the amplitudes of $\psi_n(q)$ with exact solutions, one must remember to divide the constants c_m by $\sqrt{\Delta_m}$ and to normalize the entire function $\psi_n(q)$ to one. In addition, there exists an overall phase factor for the function $\psi_n(q)$ which can be chosen to minimize the imaginary part of $\psi_n(q)$ [21] [22]. Since in this study we present the probability densities, the additional phase factor is not of any importance.

The energy eigenfunctions $\Psi_n(\vec{x})$ are determined from the finite form of Eq. (5.1) in which the continuous variable q is replaced by a sum over the cells on the PSS:

$$\begin{aligned} \Psi_n(\vec{x}) &= \sum_{m=1}^{N} G(\vec{x}, q_m; E_n)\psi_n(q_m)\Delta_m \\ &= \sum_{m=1}^{N} G(\vec{x}, q_m; E_n)\sqrt{\Delta_m}c_m, \end{aligned} \tag{5.5}$$

where $G(\vec{x}, q_m; E_n)$ is the propagator given in Eq. (5.2) evaluated at the discrete points q_m on the PSS. When computing Eq. (5.5), one must keep in mind that, depending on the system, there may be points $\vec{x}$ for which $G(\vec{x}, q_m; E_n)$ is infinite (or very large). In this case, one might choose to use a gaussian smoothing algorithm to deal with these singularities. However, as discussed in Sec. 5.4.1, this may not be necessary.

5.2 The Circle Billiard

For the circle billiard, we have chosen the circular boundary as the PSS and the coordinate q as the distance around the circumference from a reference point (see Sec. 2.2 of Chap. 3). In this case, there is only one classical trajectory, a straight line connecting a point $q' = (R, \theta')$ on the circular boundary to a point $\vec{x} = (r, \theta)$ inside the billiard domain. The classical action for this trajectory is simply given by

$$S(\vec{x}, \theta'; E) = (2mE)^{1/2}(R^2 + r^2 - 2rR\cos(\theta - \theta'))^{1/2} \tag{5.6}$$

where $(2mE)^{1/2}$ is the magnitude of the total momentum. The second derivative appearing in Eq. (5.2) is obtained by transforming Eq. (5.3) to polar coordinates. The partial derivatives with respect to the x and y coordinates become

$$\frac{\partial}{\partial x} = \cos\theta \frac{\partial}{\partial r} - \frac{\sin\theta}{r}\frac{\partial}{\partial \theta}, \tag{5.7}$$

and

$$\frac{\partial}{\partial y} = \sin\theta \frac{\partial}{\partial r} + \frac{\cos\theta}{r}\frac{\partial}{\partial \theta}. \tag{5.8}$$

Since we are considering a force-free billiard, the direction angle α of the vector $\vec{p}(\vec{x})$ at (r, θ) is defined by,

$$\sin\alpha = \frac{r\sin\theta - R\sin\theta'}{d} \qquad \text{and} \qquad \cos\alpha = \frac{r\cos\theta - R\cos\theta'}{d}, \tag{5.9}$$

where $d = (R^2 + r^2 - 2rR\cos(\theta - \theta'))^{1/2}$ is the distance between the point (R, θ') on the PSS and (r, θ) inside the billiard. Substituting Eqs. (5.6), (5.7), (5.8), and (5.9) into Eq. (5.3), we obtain,

$$\begin{aligned}\left|\frac{\partial^2 S(\vec{x}, \theta'; E)}{\partial\eta\partial\theta'}\right| &= (2mE)^{\frac{1}{2}}\left|\left(\frac{R\sin(\theta-\theta')}{d}\frac{\partial^2}{\partial r\partial\theta'} + \frac{(R\cos(\theta-\theta')-r)}{rd}\frac{\partial^2}{\partial\theta\partial\theta'}\right)S(\vec{x}, \theta'; E)\right| \\ &= \frac{(2mE)^{1/2}}{d^2}R(R - r\cos(\theta - \theta')).\end{aligned} \tag{5.10}$$

Since there are no caustics, turning points or hard wall collisions for the classical trajectory between (R, θ') and (r, θ), the Morse index ν is zero. Hence, for the circle billiard, eq. (5.2) becomes

$$G(\vec{x}, \theta'; E) = \frac{1}{(-i\hbar)^{1/2}(2\pi i\hbar)^{1/2}}\left(\frac{R}{d^2}(R - r\cos(\theta - \theta'))\right)^{\frac{1}{2}}\exp\left(\frac{i}{\hbar}S(\vec{x}, \theta'; E_n)\right). \tag{5.11}$$

5.2.1 The Connection with the WKB Approximation

In Sec. 4.2, it was shown that, for the circle billiard, the T-operator can be

approximated by a matrix which provides an analytic expression for the T-operator eigenvalue curves. The energy eigenvalues obtained from this approximate form of the T-operator are equivalent to those derived from the WKB approximation. One wonders if, analogously, the energy eigenfunctions from the T-operator method are also approximated by the WKB eigenfunctions. The following derivation is an attempt to answer this question.

Beginning with Eqs. (5.1) and (5.11), and using $\phi^{EBK}_{n_\theta,\sigma}(\theta')$ of Eq. (4.15) (with $\sigma = \pm 1$) for the value of the eigenfunction along the PSS, the energy eigenfunction for the circle billiard can be written as,

$$\begin{aligned}\Psi(\vec{x}) &= \int_0^{2\pi} G(\vec{x},\theta';E)\psi_{n_\theta,\sigma}(\theta')\,d\theta' \\ &= \frac{1}{(-i\hbar)^{1/2}(2\pi i\hbar)^{1/2}}\int_0^{2\pi}\left(\frac{R}{d^2}(R-r\cos(\theta-\theta'))\right)^{\frac{1}{2}} \\ &\quad \exp\left(\frac{i}{\hbar}S(\vec{x},\theta';E)\right)\frac{1}{(2\pi i)^{1/2}}\exp\left(\pm\frac{i}{\hbar}\hbar\sigma\nu\theta'\right)\,d\theta' \qquad (5.12)\end{aligned}$$

where $\sigma = \pm 1$. In the limit $\hbar \to 0$, and as long as the prefactor is a slowly varying function of θ', the integral of Eq. (5.12) can be evaluated using the stationary phase approximation. Essentially, in the limit $\hbar \to 0$, the phase in the exponential terms varies rapidly causing all sorts of cancellations. The main contribution to this integral comes from the points θ' near the stationary points θ_0 for which

$$\left.\frac{\partial S(\vec{x},\theta';E)}{\partial\theta'}\right|_{\theta'=\theta_0} + \hbar\sigma\nu = 0. \qquad (5.13)$$

Substituting Eq. (5.6) into Eq. (5.13) leads to the equation

$$\left.\frac{-(2mE)^{1/2}Rr\sin(\theta-\theta')}{d}\right|_{\theta'=\theta_0}+\sigma\hbar\nu=0. \tag{5.14}$$

Squaring Eq. (5.14), we obtain the quadratic equation

$$\cos^2(\theta-\theta_0)-\frac{2r}{R}\left(\frac{\hbar^2\sigma^2\nu^2}{2mEr^2}\right)\cos(\theta-\theta_0)+\frac{\hbar^2\sigma^2\nu^2}{2mEr^2}\left(1+\frac{r^2}{R^2}\right)-1=0. \tag{5.15}$$

One way of solving for θ_0 is by letting

$$\cos\alpha=\frac{\hbar\sigma\nu}{\sqrt{2mE}r}. \tag{5.16}$$

With this substitution, we are restricting r to the values $r\geq\hbar\nu/\sqrt{2mE}$. In this case, we find two stationary points with the principal values given by

$$\theta_0=\theta-\sigma\left(\cos^{-1}\left(\frac{\hbar\nu}{\sqrt{2mE}R}\right)\mp\cos^{-1}\left(\frac{\hbar\nu}{\sqrt{2mE}r}\right)\right]. \tag{5.17}$$

For these points, the classcial action is

$$S(\vec{x},\theta_0;E)=(2mE)^{1/2}\left(\sqrt{R^2-\frac{\hbar^2\nu^2}{2mE}}\mp\sqrt{r^2-\frac{\hbar^2\nu^2}{2mE}}\right) \tag{5.18}$$

and, the prefactor (including the contribution from the Fresnel integral) becomes

$$\left|\frac{\partial^2S(\vec{x},\theta';E)}{\partial\eta\partial\theta'}\right|^{\frac{1}{2}}\sqrt{\left.\frac{1}{\frac{\partial^2S(\vec{x},\theta';E)}{\partial\theta'^2}}\right|_{\theta'=\theta_0}}=\sqrt{\frac{1}{\pm r(2mE)^{1/2}\sqrt{1-\frac{\hbar^2\nu^2}{2mEr^2}}}} \tag{5.19}$$

The contribution to the integral from the first stationary point (the upper sign in Eqs. (5.17), (5.18) and (5.19)) is exactly the Langer WKB solution for the circle billiard (Appendix B) and in this way, wavefunctions from the T-operator are related to those of the WKB approximation. However, the integral includes a contribution

from both stationary points and the final form is

$$\begin{aligned}\Psi(\vec{x}) \;=\; & \frac{1}{-i\hbar}\sqrt{\frac{1}{r(2mE)^{1/2}\sqrt{1-\frac{\hbar^2\nu^2}{2mEr^2}}}} \\ & \times\left[\exp i\left(\frac{(2mE)^{1/2}}{\hbar}\left(\sqrt{R^2-\frac{\hbar^2\nu^2}{2mE}}-\sqrt{r^2-\frac{\hbar^2\nu^2}{2mE}}\right)\right)\right. \\ & \times\exp\left[i\nu\left(\cos^{-1}\left(\frac{\hbar\nu}{\sqrt{2mE}r}\right)-\cos^{-1}\left(\frac{\hbar\nu}{\sqrt{2mE}R}\right)\right)\right] \\ & +\exp(-i\pi/2)\exp i\left(\frac{(2mE)^{1/2}}{\hbar}\left(\sqrt{R^2-\frac{\hbar^2\nu^2}{2mE}}+\sqrt{r^2-\frac{\hbar^2\nu^2}{2mE}}\right)\right) \\ & \times\left.\exp\left[i\nu\left(\cos^{-1}\left(\frac{\hbar\nu}{\sqrt{2mE}r}\right)+\cos^{-1}\left(\frac{\hbar\nu}{\sqrt{2mE}R}\right)\right)\right]\right] \qquad (5.20) \\ & \times\frac{1}{(2\pi i)^{1/2}}e^{i\nu\theta} \qquad (5.21)\end{aligned}$$

5.2.2 The Numerical Results

The energy eigenfunctions for the 1st and 19th excited states (chosen arbitrarily) were numerically constructed as outlined in Sec. 5.1.1. using T-matrices of dimension $N = 25$ and $N = 150$. The resulting probability densities are displayed as contour plots in Figs. 5.1 and 5.2 along with those generated by the exact quantum mechanical treatment (Appendix A) and the WKB approximation method (Appendix B). All of the probability densities shown are unprocessed (no smoothing procedure was employed) and have been properly normalized (analytically for the exact solutions and numerically for the Bogomolny and WKB solutions). The contour levels are set to the same values in all cases. It is evident that, even at low energies, the

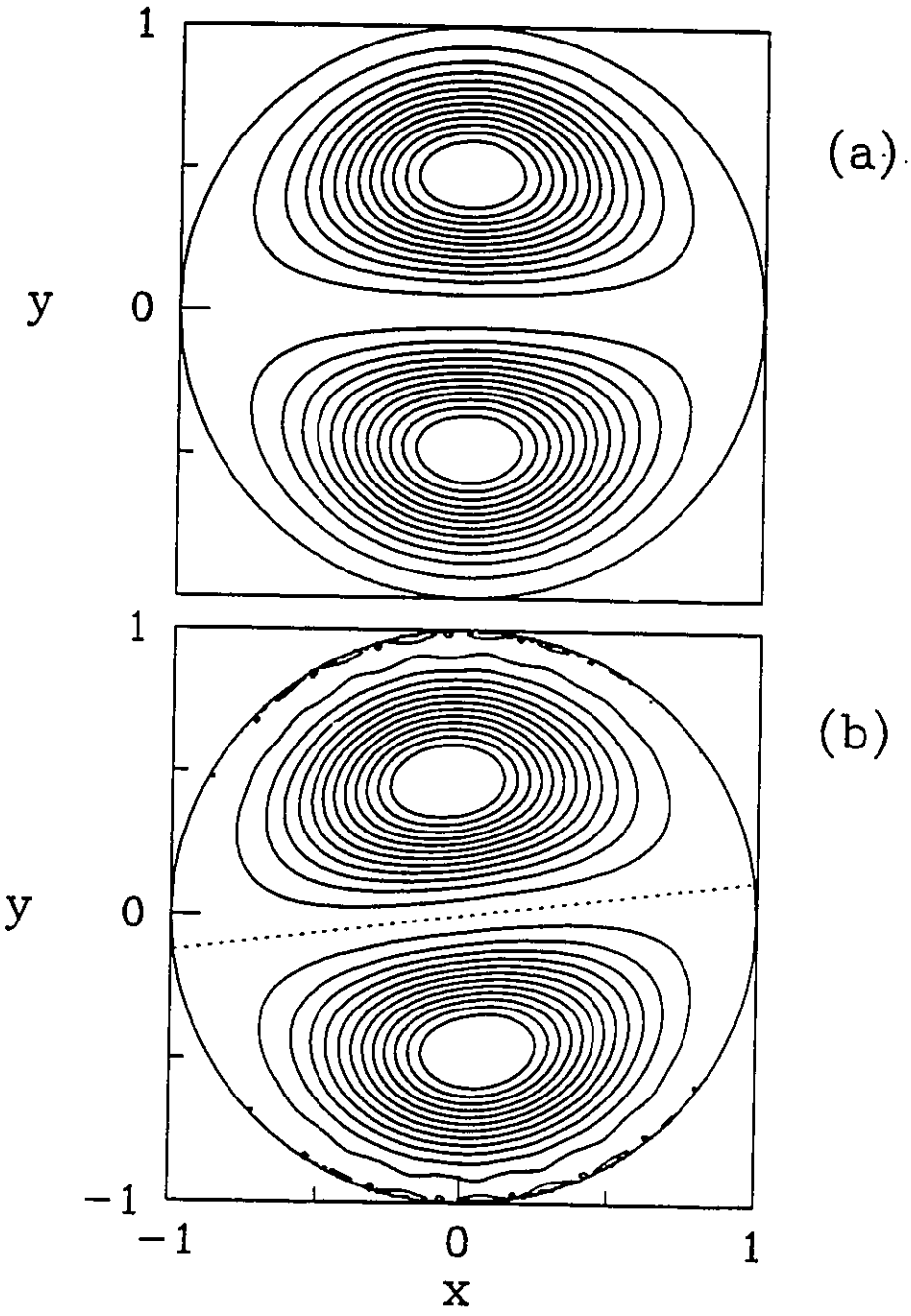

Figure 5.1: Comparison of energy eigenfunctions for the 1st excited state of the circle billiard constructed from: (a) the exact quantum solution; (b) Bogomolny's T-operator method with a 25 × 25 T-matrix; (c) Bogomolny's T-operator method with a 150 × 150 T-matrix; (d) the WKB approximation. The probability densities $|\Psi(r,\theta)|^2$ are shown with contour levels starting at 0.05 and incremented by 0.1 up to 1.15

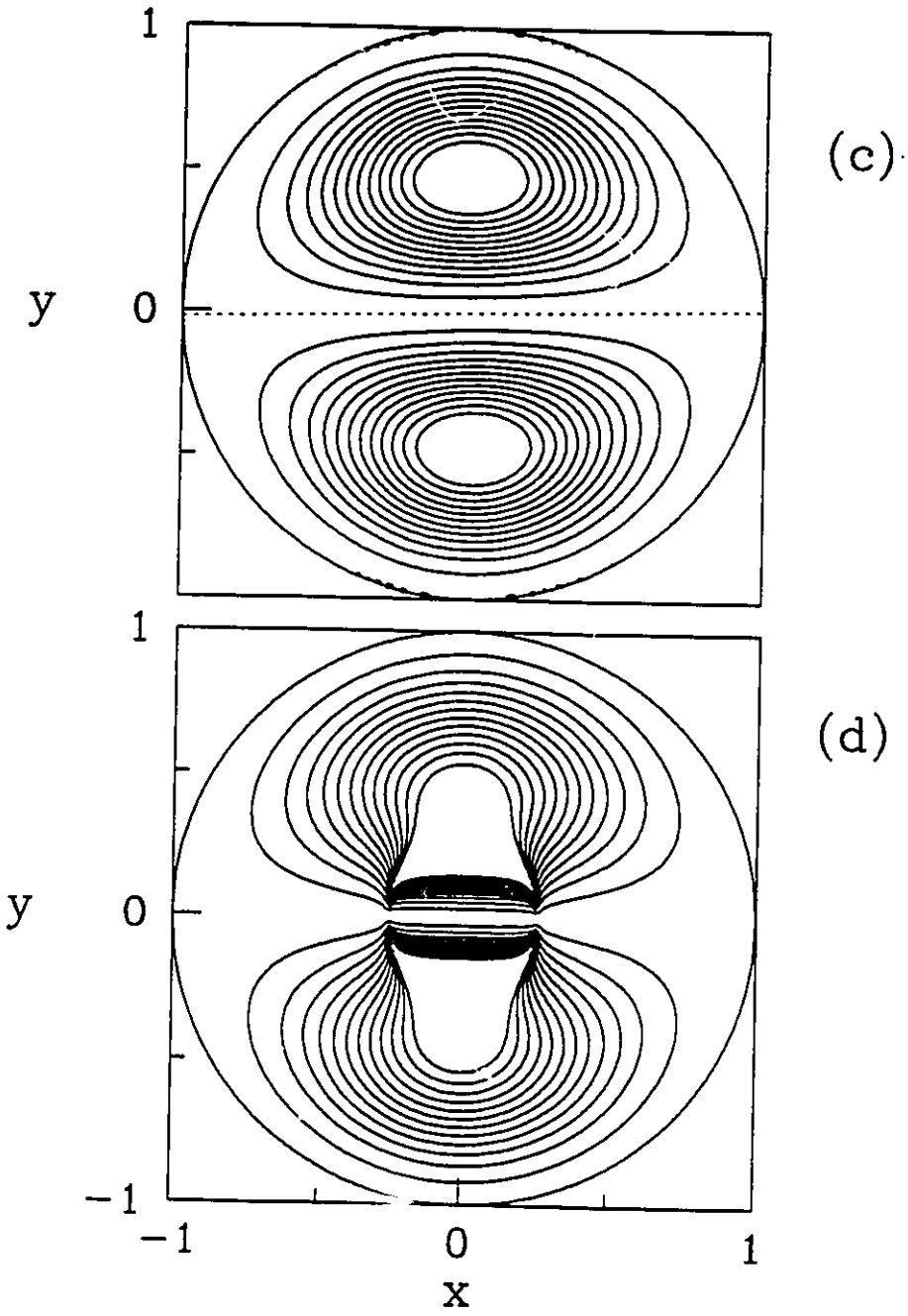

Figure 5.1: continued.

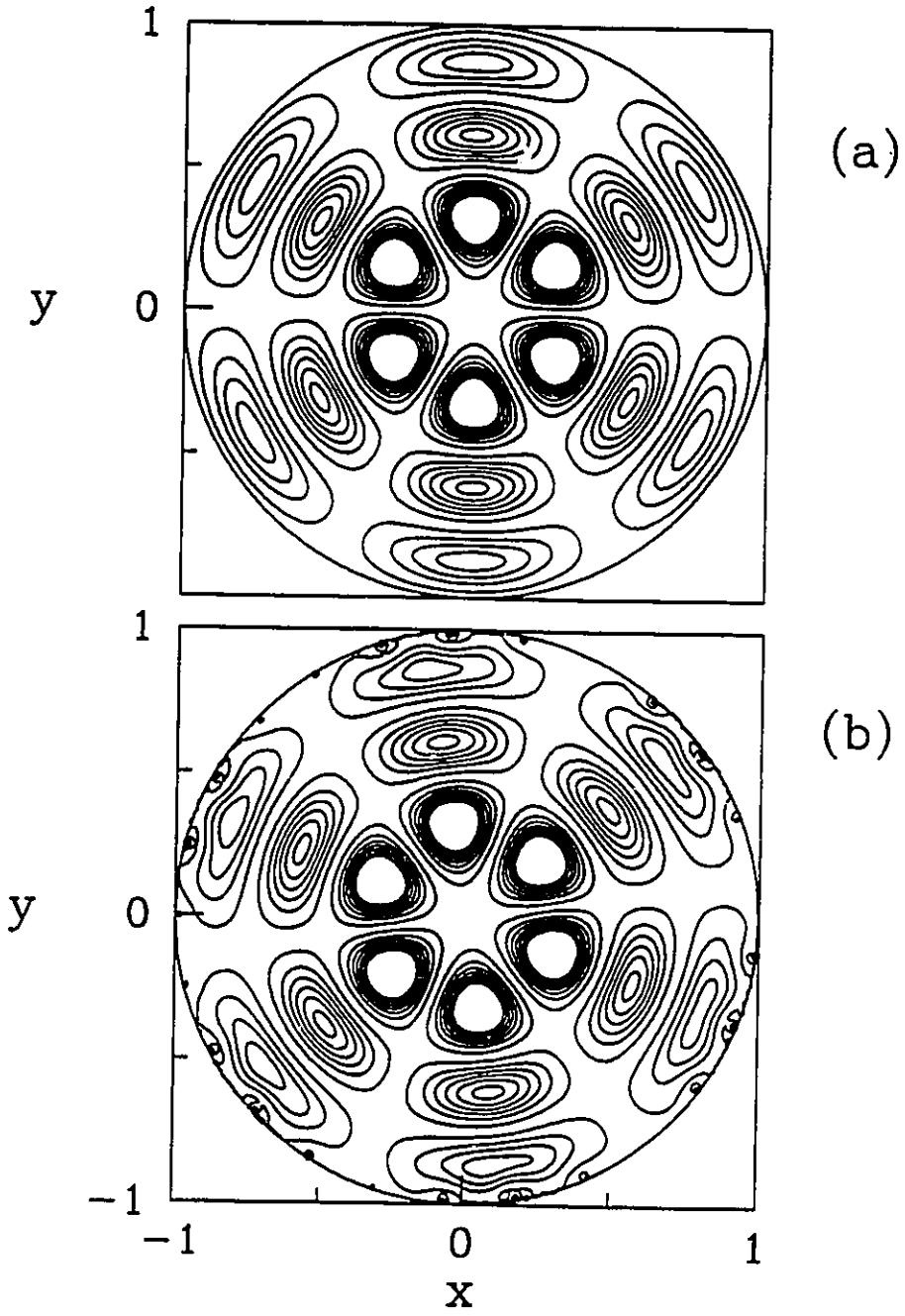

Figure 5.2: Comparison of energy eigenfunctions for the 19th excited state of the circle billiard constructed from: (a) the exact quantum solution; (b) Bogomolny's T-operator method with a 25 × 25 T-matrix; (c) Bogomolny's T-operator method with a 150 × 150 T-matrix; (d) the WKB approximation. The probability densities $|\Psi(r,\theta)|^2$ are shown with contour levels starting at 0.05 and incremented by 0.2 up to 1.25.

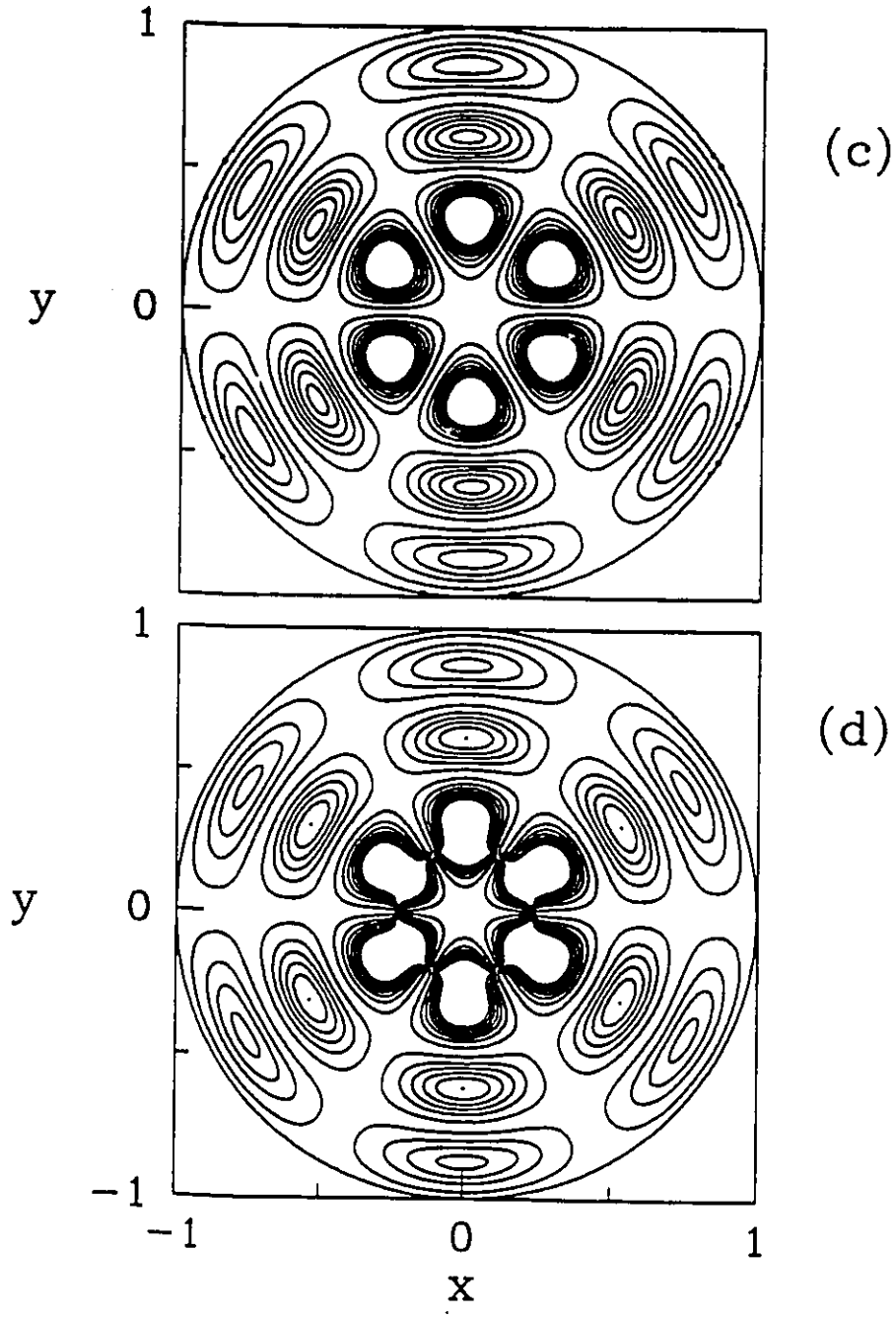

Figure 5.2: continued.

wavefunctions obtained from Bogomolny's T-operator method (Figs. 5.1(b) and (c), and 5.2 (b) and (c)) are excellent approximations to the exact solutions (Figs. 5.1(a) and 5.2(a)).

There are two obvious differences between the energy eigenfunctions from the T-operator and the exact solutions. First, the nodal lines, indicated by the dashed lines in Figs. 5.1(b) and (c), are rotated off the x-axis by a significant amount for $N = 25$ and to a lesser extent for $N = 150$. This is clearly an effect of the discretization of the boundary since the angle of rotation corresponds to θ_1, the angle of the first discrete point on the PSS. This effect would not have occurred had we chosen the centre of the first cell on the PSS to coincide with the x-axis.

The second difference is that near the billiard boundary, the contours are distorted by spurious spikes. The distortions are more pronounced for the energy eigenfunctions calculated with 25×25 T-matrices (shown in Figs. 5.1(b) and 5.2(b)) than for those obtained from T-matrices with dimension $N = 150$ (shown in Figs. 5.1(c) and 5.2(c)). Once again, the spikes, and consequently the distortions, result from the finite approximations. The spikes occur whenever the propagator $G(\vec{x}, \theta_n; E)$ calculated from Eq. (5.11) becomes infinite. It is evident from the expression for d that $G(\vec{x}, \theta_n; E) \to \infty$ as $r \to R$ and $\theta \to \theta_n$. Hence, one expects spikes to happen near the points (R, θ_n). However, since a point inside the billiard involves a contribution from every point on the boundary, the singularity is diminished. This explains why they are less pronounced in the cases with $N = 150$.

It can be seen from Figs. 5.1 and 5.2 that energy eigenfunctions from Bogomolny's T-operator method are better estimates of the exact solution than those of the WKB approximation.

5.3 The Wedge Billiard

The procedure for constructing the energy eigenfunctions of the wedge billiard is much like that of the circle billiard except that it involves more classical paths and phase indices come into play. For the wedge billiard, there are four classical paths joining a point q_n on the tilted wall (the PSS) to a point $\vec{x} = (x, y)$ inside the wedge. These paths are similar to those that connect two points on the PSS (Sec. 2.3 of Chap. 3). There are two paths, a 'high' and a 'low', that go directly from a point q_n on the PSS to a point $\vec{x}$ inside, and two paths, again a 'high' and a 'low', that collide with the vertical wall in transit from q_n to $\vec{x}$. The classical actions for these paths are derived in the same way as described in Sec. 2.3 of Chap. 3, using Eqs. (14), (15) and (16) of Chap. 3. However, in this case, (x'', y'') is no longer a point on the PSS but a point inside the billiard region. By differentiating Eq. (14) with repect to T and setting the result equal to $-E$, one obtains the following relation for the times T along the classical trajectories from q'_n to (x'', y''):

$$T_{\pm}^2 = (4E - 2(y'' + q'_n \cos\phi)) \left[1 \pm \left(1 - \frac{(x'' - q'_n \sin\phi)^2 + (y'' - q'_n \cos\phi)^2}{(2E - y'' - q'_n \cos\phi)^2} \right)^{\frac{1}{2}} \right] \quad (5.22)$$

where the plus or minus sign refers to the 'high' or 'low' paths, $(q'_n \sin\phi, q'_n \cos\phi)$ is a discrete point on the PSS and ϕ is the wedge angle. Setting x'' in Eq. (5.22) to a

positive value gives the times for the two direct paths whereas setting x'' to a negative value produces the times for the paths which involve a collision with the vertical wall (the mirror image property discussed in Sec. 2.3 of Chap. 3). The final expressions for the actions $S(\vec{x}, q_n; E)$ and second derivatives $\partial^2 S(\vec{x}, q_n; E)/\partial\eta\partial q_n$ were obtained by substituting Eq. (5.22) into Eqs. (14) and (15) of Chap. 3 and simplifying with the help of Maple, a computer language that specializes in symbolic manipulations.

The phase indices ν were calculated for each classical trajectory using a prescription similar to that described in Sec. 2.3 of Chap. 3. ν is an integer which is incremented by 2 for paths reflecting on the vertical wall, by 1 for each caustic along the trajectory, and by 1 whenever the total momentum becomes zero (at the turning point of a trajectory moving straight up along the y-direction). For the wedge billiard, the classical trajectories joining a point q_n to a point $\vec{x}$ will have at most one caustic. A caustic exists whenever the second derivative $\partial^2 S(\vec{x}, q_n; E)/\partial\eta\partial\eta_{q_n}$ changes sign (η and η_{q_n} are the normals to the trajectory at $\vec{x}$ and q_n respectively). Using this definition for detecting caustics involves calculating the x and y components of the momentum at the inital and final points and applying Eq. (D.6) twice for the normal derivative.

5.3.1 The Numerical Results

Figures 5.3 and 5.4 show contour plots of the probability densities for the

1st and 19th excited states (chosen arbitrarily) obtained from the exact quantum solutions (Appendix A), the T-matrices of dimension $N = 25$ and $N = 150$, and the WKB approximation (for the 45° wedge) (Appendix B). As for the circle billiard, the probability densities shown are unprocessed (no additional smoothing procedure was employed) and have been properly normalized (analytically for the exact solutions and numerically for the Bogomolny and WKB solutions). The agreement of the T-operator eigenfunctions (Figs. 5.3(b) and (c), and 5.4 (b) and (c)) with the exact solutions (Figs. 5.3(a) and 5.4(a)) is good, in the sense that the main features are reproduced. However, the contours of the the T-operator eigenfunctions are relatively jagged—spiked in some places and smeared near the top part of the wedge. These irregularities are more frequent in the upper region of the wedge and more pronounced in the case of the 25×25 T-matrix. The source of these deformities is the presence of caustics which, once again, plague the wedge billiard. Unfortunately, there does not seem to be an ingenious way to deal with these caustics (like the scaling technique used in Chap. 3), apart from perhaps using some standard gaussian smoothing algorithm to reduce their effect. So, we have to learn to live with them. On the other hand, since the detrimental effect of caustics is reduced with higher T-matrix dimensions (as shown from the results of the 150×150 T-matrix), the caustics are not as problematic as they initially seem to be.

The caustics occur whenever the second derivative of the action $\partial^2 S/\partial\eta\partial q_n$, appearing in the prefactor of Eq. (5.2), becomes infinite. As discussed in Chap.3,

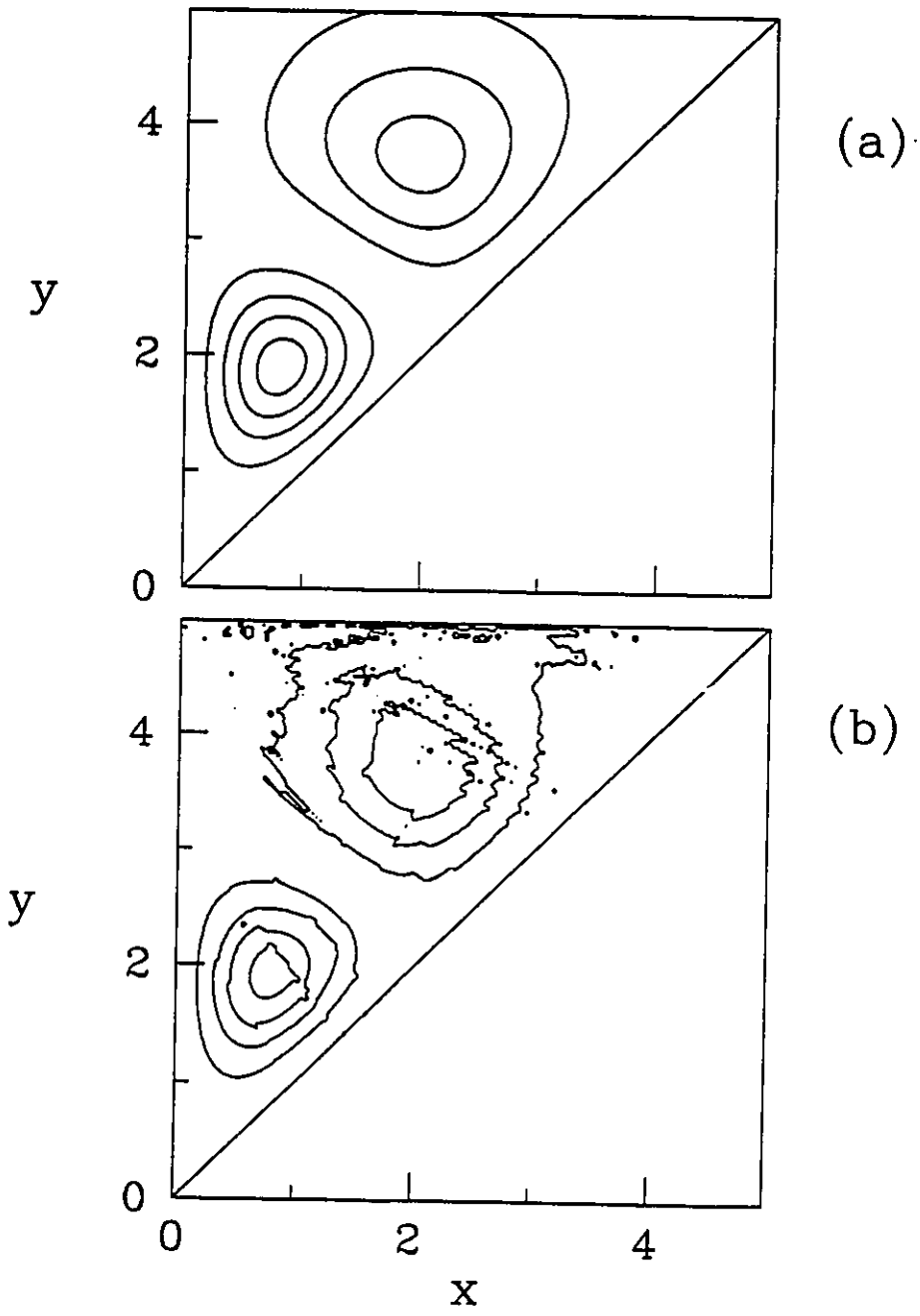

Figure 5.3: Comparison of energy eigenfunctions for the 1st excited state of the 45° wedge billiard constructed from: (a) the exact quantum solution: (b) Bogomolny's T-operator method with a 25 × 25 T-matrix: (c) Bogomolny's T-operator method with a 150 × 150 T-matrix: (d) the WKB approximation. The probability densities $|\Psi(r,\theta)|^2$ are shown with contour levels starting at 0.05 and incremented by 0.1 up to 0.95

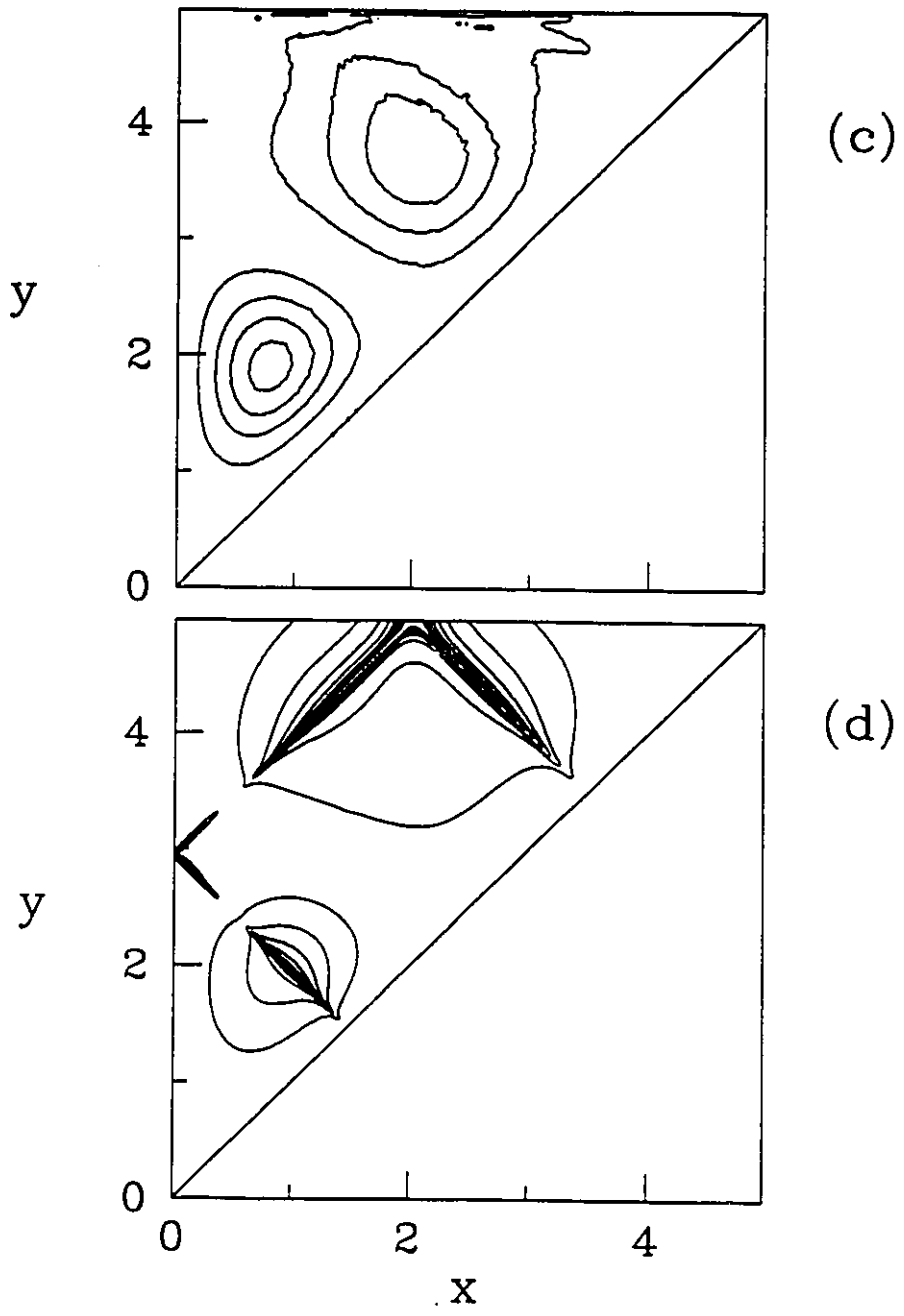

Figure 5.3: continued.

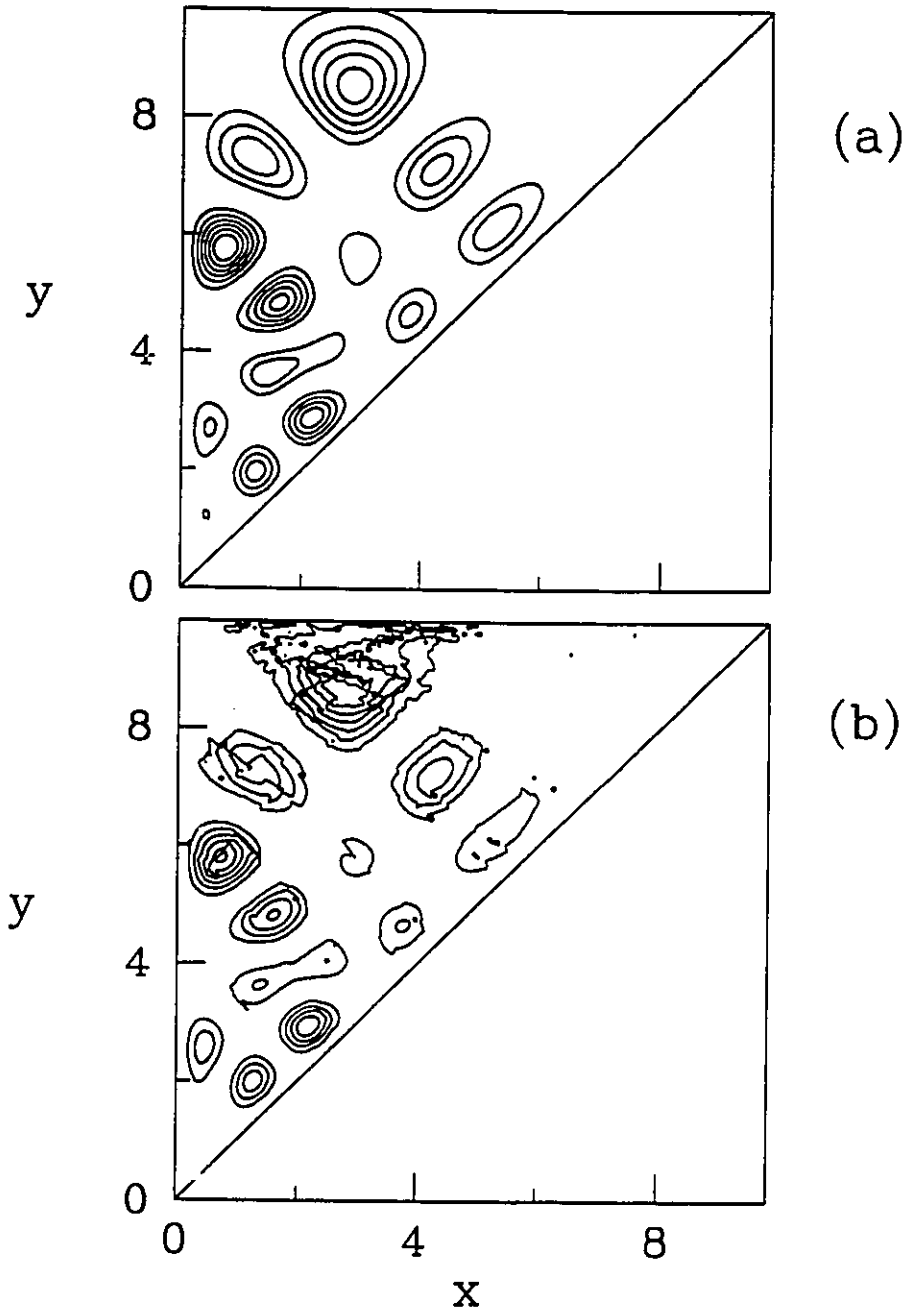

Figure 5.4: Comparison of energy eigenfunctions for the 19th excited state of the 45° wedge billiard constructed from: (a) the exact quantum solution: (b) Bogomolny's T-operator method with a 25 × 25 T-matrix: (c) Bogomolny's T-operator method with a 150 × 150 T-matrix: (d) the WKB approximation. The probability densities $|\Psi(r,\theta)|^2$ are shown with contour levels starting at 0.05 and incremented by 0.05 up to 0.25.

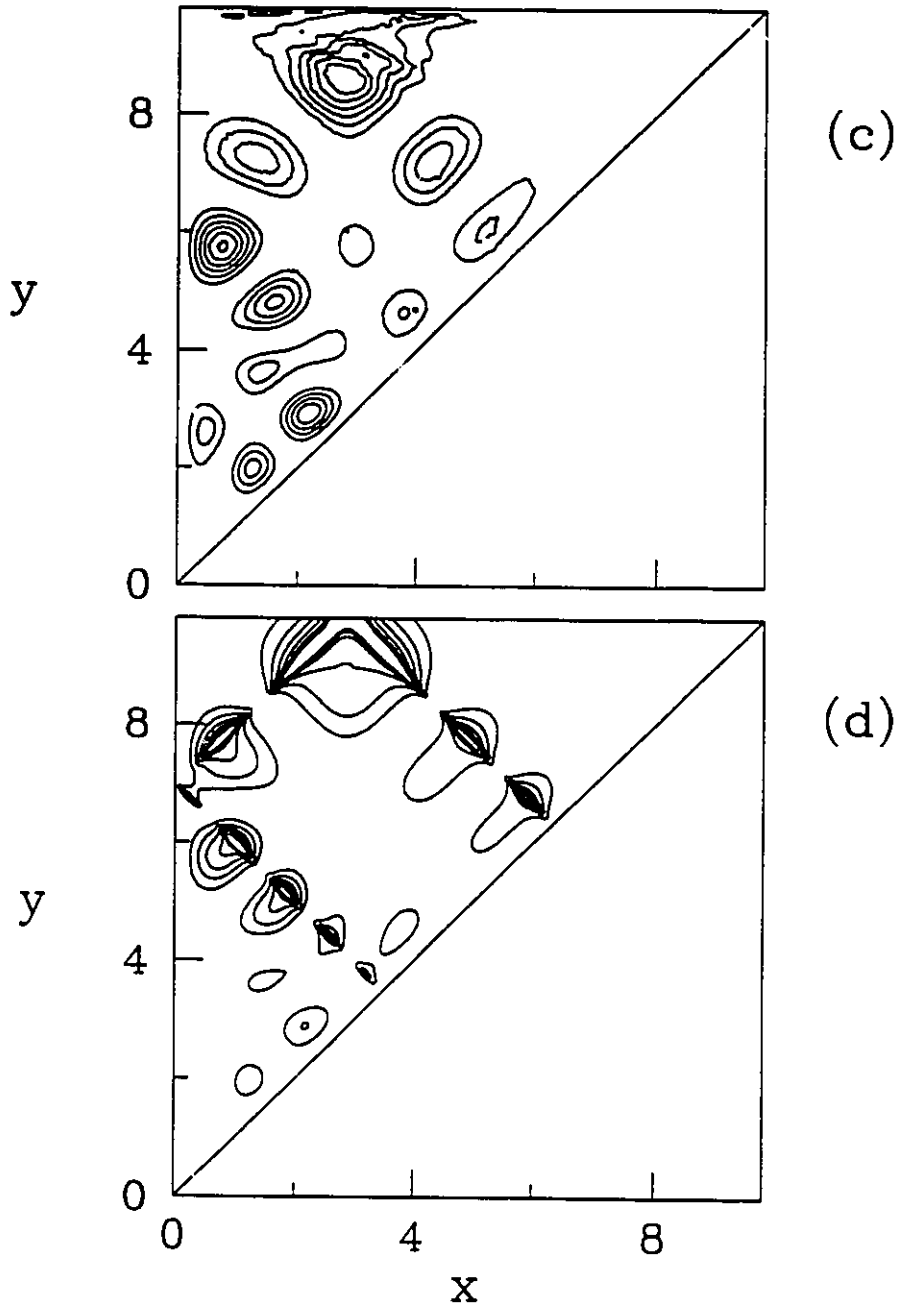

Figure 5.4: continued.

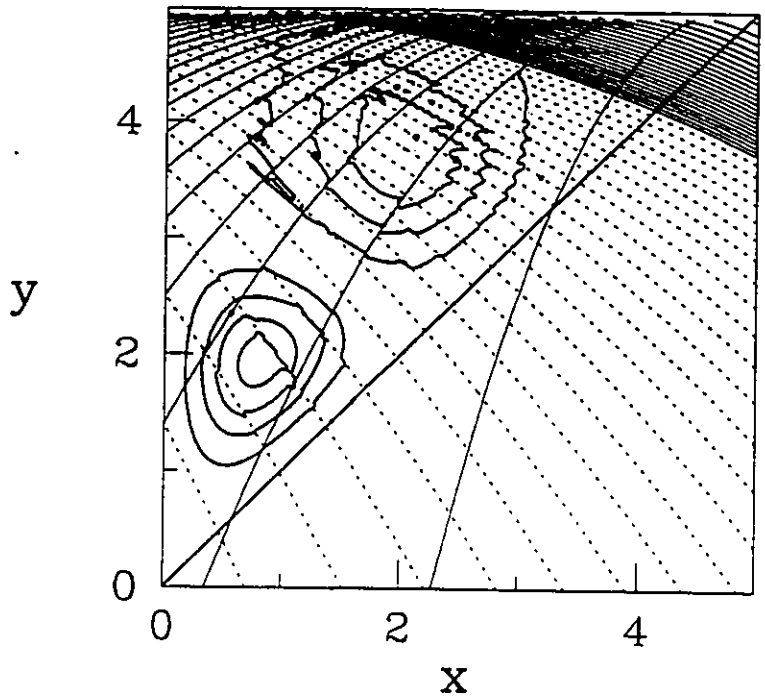

Figure 5.5: Caustic lines of the 45° wedge billiard. The probability density shown is for the 1st excited state (same as in fig. 5.3) calculated from a 25 × 25 T-matrix. Since in this case, there are 25 discrete points on the tilted wall, there are 50 caustic lines on this graph (two for every point on the PSS). The solid lines are the caustic curves arising from the merging of direct paths while the dotted lines come from the paths which hit the vertical wall.

this happens at points $\vec{x} = (x, y)$ such that the two direct paths or the two paths via the vertical wall merge. These points can be determined analytically by setting the discriminant in Eq. (5.22) equal to zero. This produces two curves (caustic lines) for every point q_n on the PSS. To illustrate their effect, the caustic lines from 25 points q_n were superimposed on the 1st excited state in Fig. 5.5. The 25 lines drawn for the direct paths (solid) and 25 lines for the paths that hit the vertical wall (dotted) align well with the fractures and spikes of the probability density. In addition, the fact that they are more concentrated in the upper region of the wedge explains why the

contours are more distorted in that part of the billiard domain. For higher T-matrix dimensions, the density of caustic lines increases and, hence, one might expect this to cause the results to deteriorate. However, the probability density at each point $\vec{x} = (x, y)$ inside the billiard domain involves a contribution from all the points q_n on the PSS. It appears that the sum of these contributions has the effect of reducing the influence of caustics. Hence, the results improve with higher T-matrix dimension although the number of caustic lines has increased.

Since the wavefunctions from the T-operator are constructed from classical paths, the probability densities do not extend beyond the region of allowed classical motion. However, because of the distortions, it is difficult to judge whether the contour lines of the T-operator eigenfunctions, if extrapolated smoothly, would extend to the classically forbidden region as in the case of the exact quantum solution. The T-operator eigenfunctions themselves are only defined up to some point q_{max}, the highest classically accessible point on the PSS. In his recent thesis, Haggerty [21] presents a picture gallery comprising a selection of T-operator eigenfunctions for the Nelson potential. He compared them to the exact values and noticed that the T-operator eigenfunctions are compressed into the classically accessible region on the PSS. The probability density decreases more rapidly near the edge of the classically accessible region as compared to the exact solutions. This effect is not consistently observed for the wedge billiard. Fig. 5.6 compares the T-operator eigenfunctions for the 1st and 19th excited states with the exact quantum solutions. The PSS eigenfunction for the

1st excited state appears to be compressed, whereas this effect is not observed for the PSS eigenfunction for the 19th excited state. Note that, technically, the PSS is an infinitesimal distance inside the billiard boundary, and consequently, the energy eigenfunctions along the PSS are not zero. The exact energy eigenfunctions plotted in Fig. 5.6 are defined on the surface at $r = R - \delta r$.

It would be interesting to see if one could calculate the probability density in the space that extends beyond the classically accessible region by including complex actions from fictitious paths in Bogomolny's expression. A classical path between the points $(q'_n \sin\phi, q'_n \cos\phi)$ and (x'', y'') exists whenever Eq. (5.22) is real. The fictitious paths would be those for which Eq. (5.22) is complex and consequently, would have complex actions. However, it isn't clear what one would assign to the values of the Morse indices for these paths.

It is evident that the energy eigenfunctions from Bogomolny's T-operator method are much better representations of the exact solution than those of the WKB approximation, especially at low energies. The problem with caustics is resolved with higher T-matrix dimensions, whereas the singularities are inherent to the WKB solution with no chance of removing them. The only drawback of the T-operator approach is that, for the wedge billiard, the energy eigenfunctions can only be constructed numerically, and using Bogomolny's expression in the present form, can only provide probability densities in the classically allowed region of motion.

A few energy eigenstates for the 60° wedge billiard are plotted in Fig. 5.7

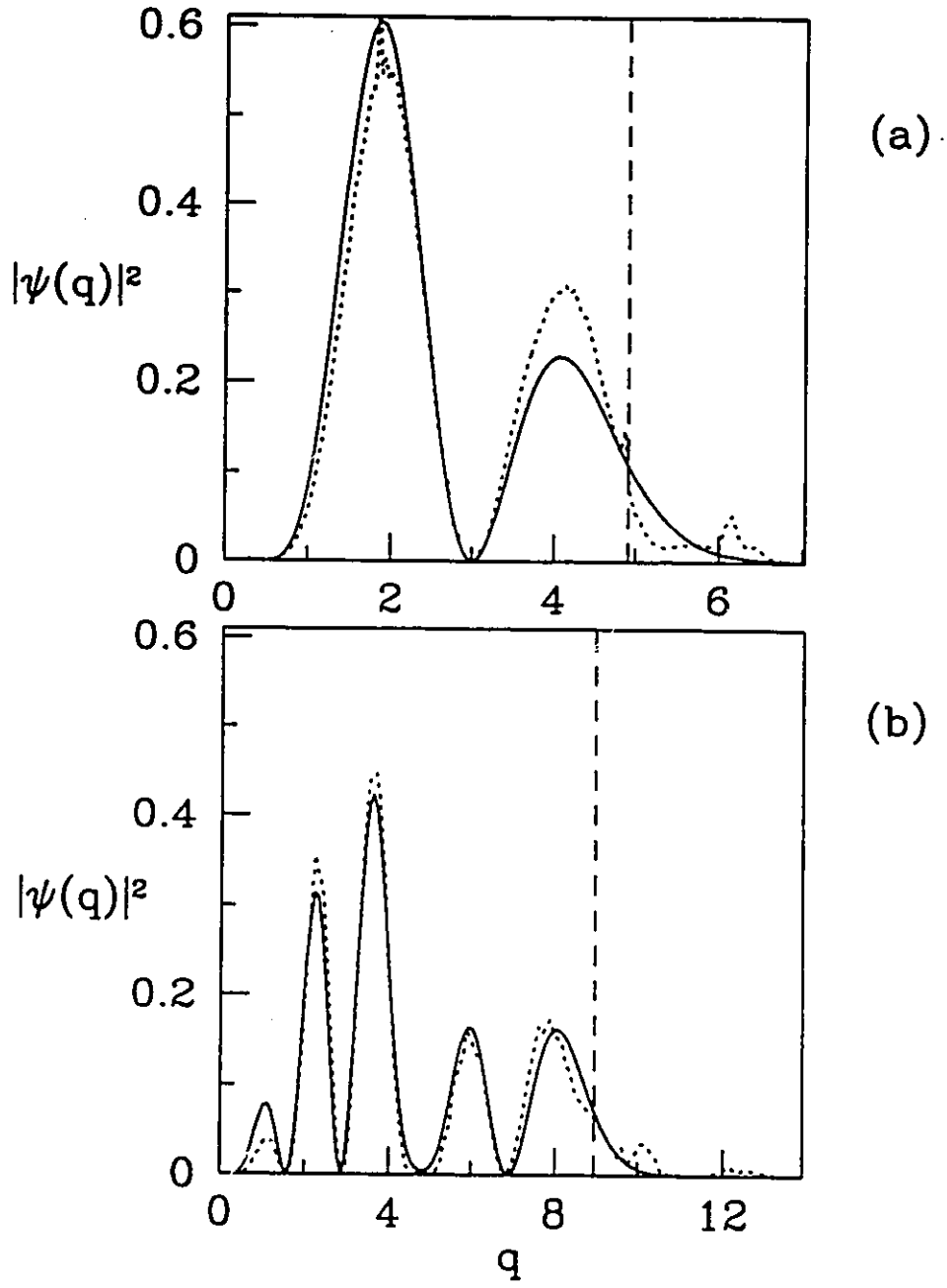

Figure 5.6: T-operator eigenfunction for the 1st and 19th excited state. The probability density along the PSS from the exact quantum solution (solid line), from a 25 × 25 T-matrix (dotted line), and from a 150 × 150 T-matrix (dashed line). The vertical line indicates the limit of the classically allowed region. In (a), it appears that the T-operator eigenfunctions are squeezed into the classically allowed region.

and are compared to the exact results (insets) calculated from the diagonalization of the Hamiltonian matrix (as described in Chap. 4). The fact that the energy eigenfunctions can be recovered from the T-operator eigenfunctions defined on the PSS suggests that the T-operator eigenfunctions contain the essential information about the energy eigenfunctions and that they are equally as good candidates as the $\Psi_n(\vec{x})$ for studying the manifestation of chaos in semiclassical wavefunctions. This is certainly advantageous since the T-operator eigenfunctions, being one dimension less then the true energy eigenfunctions, are much easier to deal with. It would be interesting to see if scarring also occurs with T-operator eigenfunctions. In this case, the scarring might correspond to peaks near the intersections of periodic orbits with the PSS.

A final point of interest concerns recovering the even energy eigenstates of the symmetric wedge billiard from the T-operator of the desymmetrized wedge billiard (which provides only the odd eigenstates of the symmetric wedge billiard). In principle, one should be able to recover the even eigenstates of the symmetric wedge billiard [47] by *effectively* removing the vertical wall from the wedge billiard problem. This is achieved simply by omitting the contribution of 2 to the phase index for classical paths that bounce against the vertical wall. To test this idea, we chose two energy eigenvalues calculated from the T-operator of the symmetric 90° wedge billiard (described in chap 4). The first energy eigenvalue, corresponding to $n_x = n_y = 1$, does not exist in the 45° wedge problem, while the second corresponds to a degen-

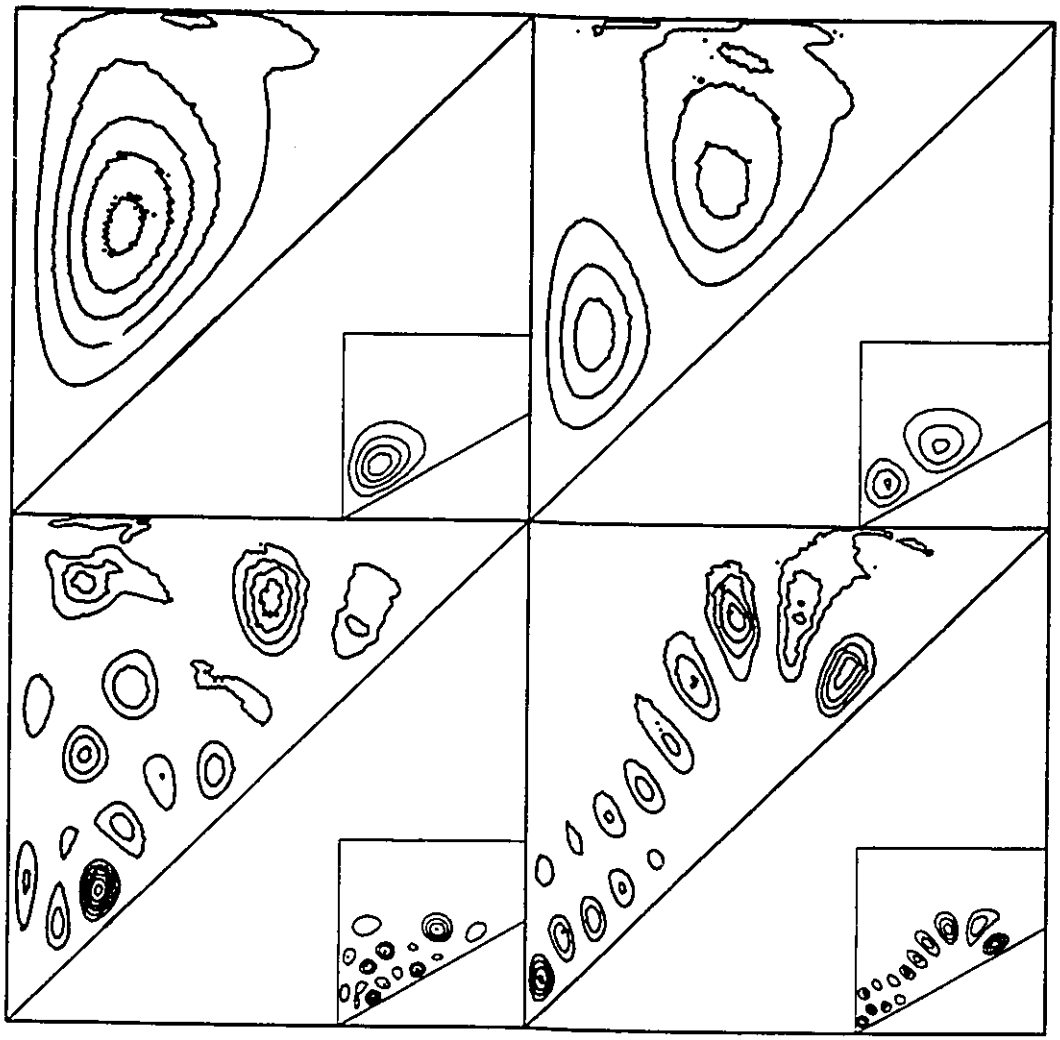

Figure 5.7: Energy eigenfunctions from the T-operator method for the 60° wedge billiard. All of the probability densities shown where obtained from a 150 × 150 T-matrix. (a) the ground state, (b) the 1st excited state, (c) the 19th excited state and (d) the 29th excited state. Insets are the exact quantum solutions.

erate eigenstate (the 14th excited state of the symmetric 90° wedge billiard); the odd eigenstate belongs to the 11th excited state of the 45° wedge billiard. Then, we simply calculated the T-operator for the 45° wedge using these energies and ignored the contribution to the phase index for paths which collide with the vertical wall. Using the resulting T-operator eigenfunctions, we constructed the energy eigenfunctions with the 45° wedge program, again ignoring the vertical wall. The results from these calculations using 75×75 T-matrices are shown in fig. 5.8. Based on the good agreement of these even energy eigenstates with the exact quantum solutions, I conclude that it is indeed possible to regain the even excited states of the symmetric wedge problem with the T-operator for the desymmetrized wedge billiard. Hence, one can simply work with a desymmetrized system knowing that the solutions to the full system can easily be recovered.

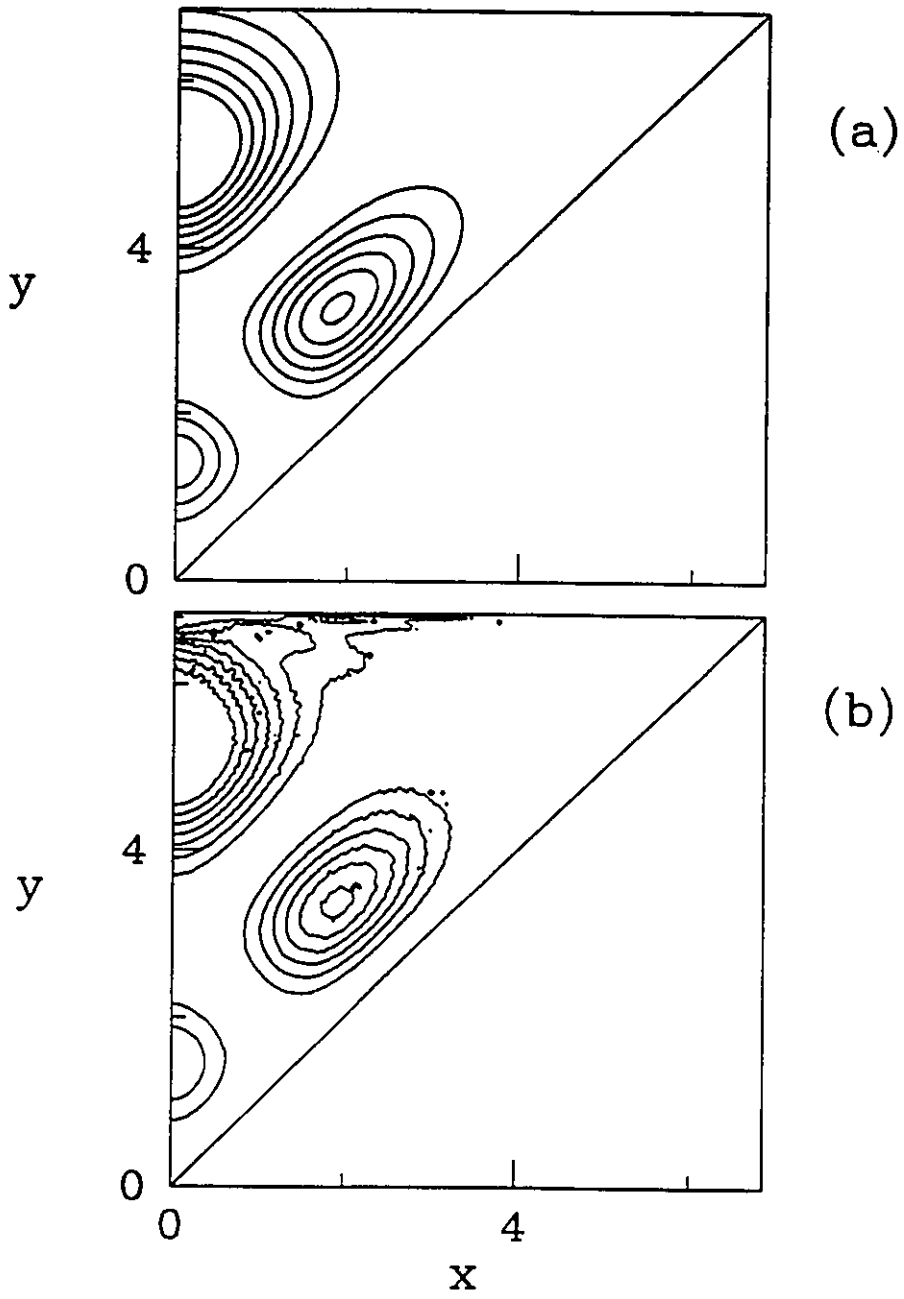

Figure 5.8: Energy eigenfunctions for the 3rd ($E = 5.15$) and 11th ($E = 8.41$) excited states of the symmetric 90° wedge. The energy eigenfunctions in (a) and (c) are the exact quantum solution. The energy eigenfunctions in (b) and (d) were calculated from a 75×75 T-matrix for the 45° wedge effectively ignoring the vertical wall by removing the contribution to the phase index of classical paths colliding with the vertical wall.

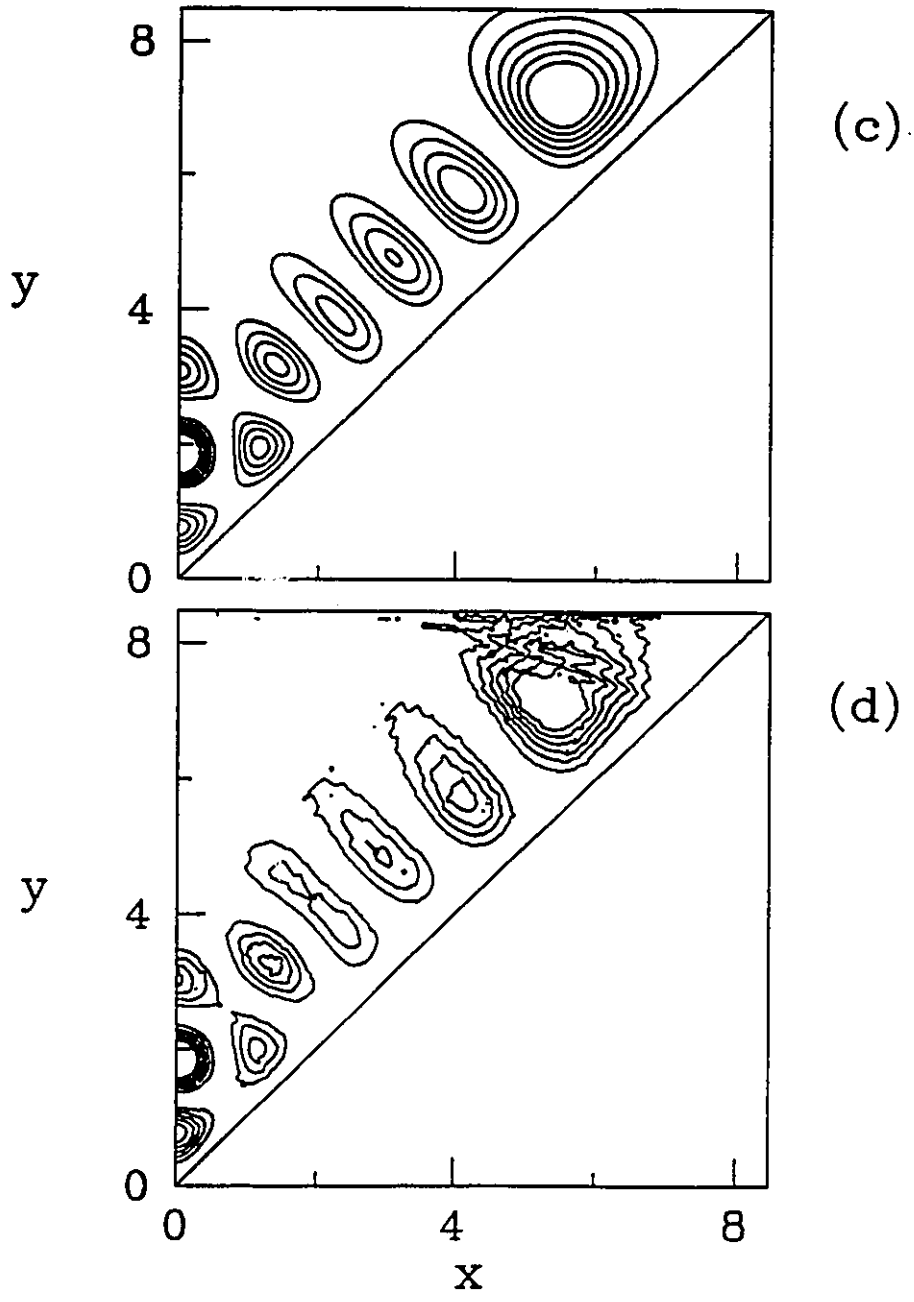

Figure 5.8: continued.

Chapter 6

Concluding Remarks

We have employed finite approximations to Bogomolny's T-operator in coordinate space to calculate semiclassical energy eigenvalues for a variety of integrable and nonintegrable systems. We have shown that, overall, this method gives excellent results for the integrable systems, the circle billiard and the 45° wedge billiard, as well as for the nonintegrable systems, the 49° and 60° wedge billiards (both showing hard chaos) and the 41° and 30° wedge billiards (both showing mixed behaviour). With Bogomolny's semiclassical quantization condition, one has better success estimating energy eigenvalues from the T-operator eigenvalue curves rather than looking for the minima of the determinant $|\det[1 - T(E)]|$. Results obtained from the finite approximation to Bogomolny's T-operator appear to be sensitive to the choice of the PSS and the partition in phase space. For the 49° wedge billiard, an alternate partition of phase space involving the symbolic sequences did not give good results for higher T-matrix dimensions.

As a technique for obtaining semiclassical energy eigenvalues, Bogomolny's

T-operator method is easier to use than the Gutzwiller trace formula and other quantization schemes based on periodic orbits. The difficult task of finding a large number of periodic orbits is no longer an issue. Instead, one only needs to find the classical trajectories from one point to another on the PSS. In addition, there appear to be no formal convergence problems in Bogomolny's method, in contrast to the Gutzwiller trace formula which is at best conditionally convergent. Yet, one can still recover information about the periodic orbits of the system from Bogomolny's T-operator method. As we have shown, the actions of the periodic orbits are obtained from Fourier transforms of traces of products of T-matrices.

One of the attractive features of Bogomolny's T-operator method is that, in addition to semiclassical energy eigenvalues, it is possible to calculate the semiclassical energy eigenfunctions in a relatively simple manner. The energy eigenfunctions of the system are constructed from the T-operator eigenfunctions defined on the PSS. In this way, the T-operator eigenfunctions reflect properties of the system and these may be used, intead of the complete energy eigenfunctions, for future studies of the manifestations of chaos in wavefunctions. In particular, it would be interesting to see if energy averaged T-operator eigenfunctions show signs of scars of periodic orbits that cross the PSS.

Bogomolny's T-operator provides a new perspective on the connection between classical and quantum mechanics: specifically, the T-operator eigenvalues play an important role. For separable Hamiltonian systems, it can be shown that, in

the semiclassical limit, the T-operator eigenvalue curves are related to the quantum numbers of the system (from Lauritzen's EBK form) and consequently, the phase space tori of the corresponding classical system. Each T-operator eigenvalue curve $\lambda_\alpha^{EBK}(E)$ for the circle billiard can be labelled by a quantum number $\alpha = \nu$ whereas for the 45° wedge billiard, they are labelled by the difference in quantum numbers $\alpha = n_1 - n_2$. For unknown reasons, there is a discrepancy between the T-operator eigenvalue curves from Bogomolny's T-matrix $\lambda_\alpha^B(E)$ and those from Lauritzen's EBK form $\lambda_\alpha^{EBK}(E)$ for the 45° wedge billiard. This discrepancy may disappear at high energies.

Since Bogomolny's T-operator is defined for any type of dynamical system, it may hold the key to the characterization of chaos in quantum systems. In addition, it opens a new door for the study of mixed systems. We have shown that, much like the expected nearest neighbour energy level statistics, the phase separations of T-operator eigenvalues for the 45° wedge billiard (a regular system) follow the Poisson distribution and that those for the 49° wedge billiard (a chaotic system) follow the Wigner distribution. For mixed systems, I conjecture that the distribution of T-operator eigenvalue phase separations will vary for different energy eigenvalues of the system. For the energy eigenvalues belonging to the regular part of the spectrum (associated with the regular behaviour of the classical system), the phase separations of the T-operator eigenvalues will tend towards a Poisson distribution, whereas for energy eigenvalues belonging to the chaotic part of the spectrum (associated with the

chaotic behaviour of the classical system), the phase separations of the T-operator eigenvalues will follow a Wigner distribution. To test this hypothesis, I would first need to classify the energy spectra of a wedge billiard displaying mixed behaviour with a numerical method such as the one presented by Bohigas *et al.* [14]. Then, I could study the distribution of the phase separations of the T-operator eigenvalues for 'regular' or 'chaotic' energy eigenvalues. However, to get reasonably good statistics for the distribution of phase separations at a particular energy, it would be necessary to study high energy values since the number of T-operator eigenvalues on the unit circle depends on energy. Consequently, this would require diagonalizing very large T-matrices, ideally with dimensions approximately $6\times$ the number of T-operator eigenvalues, to ensure accurate results.

This thesis has only begun to explore the possibilities of Bogomolny's T-operator method as a tool for semiclassical analysis. I hope that the results of this thesis will encourage others to pursue further studies employing this technique. The following paragraphs discuss two projects involving Bogomolny's T-operator method that are currently in progress but have not been mentioned so far in this thesis.

The first is a study of the effect of billiard boundary distortions on the classical periodic orbits of the system and on the spectra of their quantum analogues. Intuitively, one would expect that for a boundary distortion that is small compared to the de Broglie wavelength, the quantum energy eigenstates would essentially be unaffected, whereas many of the periodic orbits of the classical billiard would be de-

stroyed. If this is the case, how does the Gutzwiller trace formula relate a completely different set of classical periodic orbits to the same quantum energy eigenstates?

Bogomolny's T-operator is ideally suited for this study since it can easily be implemented for billiard systems with any boundary shape. Moreover, the actions of the periodic orbits, if they exist, can be recovered by taking the Fourier transform of the traces of Bogomolny's T-matrix. David Goodings and I have carried out calculations for a circle billiard whose boundary is distorted into sine waves of different wavelengths and amplitudes (since an irregularity on the boundary can be analyzed into Fourier components). Preliminary results of this study were presented at the Symposium on Classical and Quantum Billiards in Ascona, Switzerland, in July 1994. We have found discrepancies in the energy eigenvalue shifts calculated from Bogomolny's T-operator method and 1st order perturbation theory (given in Morse and Feshbach [31]). The Fourier transforms of traces of products of the T-matrix show that the shorter periodic orbits are not destroyed by the sinusoidal distortions on the billiard boundary. This project is being completed in collaboration with Nina Snaith. As a final note, in Ascona, we learned that the sinusoidally distorted circle billiard models collective surface modes in nuclear systems. Fendrik *et al.* [17] have shown, by numerically calculating the Lyapunov exponent and drawing the surface of section, that this billiard is chaotic for various amplitudes and frequencies of distortions.

Szeredi [42] has succeeded in providing a connection between unperturbed periodic orbits and first order quantal energy shifts for boundary perturbations of

billiards. His expression involves the first derivative of the actions $S_\gamma(E,\eta)$ of periodic orbits (labelled by γ) with respect to a perturbing parameter η. If a periodic orbit is destroyed by a small change $\delta\eta$, one would expect that $\partial S_\gamma(E,\eta)/\partial\eta$ would no longer be defined. In this way, Szeredi's expression may provide a way to learn about the classical periodic orbits that are destroyed by billiard boundary distortions.

This work on billiard boundary distortions could easily be extended to study the effect of boundary distortions on the conduction properties of *microstructures*, solid-state devices that confine electrons to two-dimensional areas a few hundreds of angstroms in size. Quantum conductance fluctuations have been simulated with semiclassical theory by Lin et al. [29], who assumed that imperfections will randomly scatter trajectories. Using the discrete form of Bogomolny's T-operator, one could easily put random discrete distortions around a boundary and calculate the transmission amplitudes connecting the incoming and outgoing channels to the microstructure. Using a formula developed by Jalabert *et al.* [24], one could calculate the conductance fluctuations and compare then with the results obtained by Lin et al.

The second project which is currently in progress, in collaboration with David Goodings and Nina Snaith, is to implement the effect of diffraction in Bogomolny's formalism. In its present form, the T-operator is constructed entirely from classical trajectories. Hence, Bogomolny's method cannot reproduce the effects caused by diffraction—a genuine quantum phenomena. To illustrate these effects, we are

studying a two-dimensional circle billiard with a small concentric disk. In the purely classical case, the disk is an obstruction which deflects trajectories, whereas in the quantum case, waves (creeping waves) can diffract into the shadowed classically forbidden region. Our goal is to introduce diffractive paths in Bogomolny's formalism by considering a special form for the Green's function representing the diffraction process [45].

Bibliography

[1] Arfken G *Mathematical Methods for Physicists* 3rd ed (Academic Press Inc San Diego 1985)

[2] Aurich R and Steiner F 1991 *Physica D* **48** 445

[3] Berry M V 1989 *Proc R Soc Lond A* **423** 219

[4] Berry M V and Ozorio de Almeida A M 1973 *J Phys A* **6** 1451

[5] Berry M V and Robnik M 1984 *J Phys A* **17** 2413

[6] Boasman P A 1992 Ph.D. thesis University of Bristol

[7] Boasman P A 1994 *Nonlinearity* **7** 485

[8] Bogomolny E B 1988 *Physica D* **31** 169

[9] Bogomolny E B and Carioli M 1993 *Physica D* **67** 88

[10] Bogomolny E B 1992 *Nonlinearity* **5** 805

[11] Bogomolny E B 1992 *CHAOS* **2** 5

[12] Bohigas O and Giannoni J M 1984 *Lecture notes in Physics* **209** 1

[13] Bohigas O Giannoni J M and Schmit C 1984 *Phys Rev Lett* **52** 1

[14] Bohigas O Tomsovic S and Ullmo D 1990 *Phys Rev Lett* **64** 1479

[15] Doron E and Smilansky U 1992 *Nonlinearity* **5** 1055

[16] Einstein A 1917 *Verh Dtsch Phys Ges* **19** 82

[17] Fendrik A J Vega J L Dorso C O and Bernath M 1991 *Nonlinear Phenomena in Fluids, Solids and Other Complex Systems* Cordero P and Nachtergaele B (editors) 447

[18] Goldstein H *Classical Mechanics* 2nd ed (Addison-Wesley Publishing Company Inc US 1981)

[19] Goodings D A and Szeredi T 1991 *Am J Phys* **59** 924

[20] Gutzwiller M C 1971 *J Math Phys* **12** 343: Gutzwiller M C *Chaos in Classical and Quantum Mechanics* (Springer-Verlag New York 1990)

[21] Haggerty M R 1994 Ph.D. thesis M.I.T.

[22] Haggerty preprint

[23] Heller E J *Phys Rev Lett* **53** 1515

[24] Jalabert R A Baranger H U and Stone A D 1990 *Phys Rev Lett* **65** 2442

[25] Kac M 1966 *Am Math* **73** 1

[26] Knudson S K and Noid D W 1989 *J Chem Edu* **66** 133

[27] Langer R E 1937 *Phys Rev* **51** 669

[28] Lauritzen B 1992 *CHAOS* **2** 409

[29] Lin W A and Delos J B 1993 *CHAOS* **3** 655

[30] Meredith D C 1992 *J Stat Phys* **68** 97

[31] Morse and Feshbach 1953 *Methods of Theoretical Physics* (McGraw-Hill New York 1953)

[32] Numerical Recipes 2nd ed (Cambridge University Press US 1992)

[33] Percival I C 1973 *J Phys B* **6** L229

[34] Prosen T 1994 *J Phys A* **27** L709

[35] Provost D and Brumer P *Phys Rev Lett* **74** 250

[36] Rouvinez C and Smilansky U 1995 *J Phys A* **28** 77

[37] Rouvinez C 1995 Ph.D. thesis École Polytechnique Fédérale de Lausanne

[38] Schiff L I *Quantum Mechanics* 2nd ed McGraw-Hill New York 1955

[39] Szeredi T 1993 Ph.D. thesis McMaster University

[40] Szeredi T and Goodings D A 1993 *Phys Rev E* **48** 3518

[41] Szeredi T and Goodings D A 1993 *Phys Rev E* **48** 3529

[42] Szeredi T 1995 preprint

[43] Tomsovic S and Heller E J 1993 *Phys Rev Lett* **70** 1405

[44] Van Vleck J H 1928 *Proc Nat Acad Sci* **14** 178

[45] Whelan N 1995 preprint

[46] Whelan N Goodings D A and Cannizzo J K 1990 *Phys Rev A* **42** 742

[47] Whelan N personal communication

Appendix A

The Exact Quantum Solution

A.1 The Circle Billiard

The circle billiard is a two-dimensional system consisting of a particle of mass m moving freely inside a circular region of radius $r = R$. The quantum mechanical description of this particle's motion is given by the time-independent Schrödinger equation, expressed in terms of cylindrical coordinates (r, ϕ),

$$-\frac{\hbar^2}{2m}\left(\frac{\partial^2}{\partial r^2}+\frac{1}{r}\frac{\partial}{\partial r}+\frac{1}{r^2}\frac{\partial^2}{\partial \phi^2}\right)\Psi(r,\phi)=E\Psi(r,\phi), \quad \text{for } 0 \le r < R, \tag{A.1}$$

along with the Dirichlet boundary condition $\Psi(R, \phi) = 0$. By setting $\Psi(r, \phi) = R(r)\Phi(\phi)$, Eq. (A.1) separates into two differential equations,

$$\frac{d^2\Phi(\phi)}{d\phi^2}+\nu^2\Phi(\phi)=0 \tag{A.2}$$

for the angular dependence, and

$$r^2\frac{d^2R(r)}{dr^2}+r\frac{dR(r)}{dr}+\left(\frac{2mE}{\hbar^2}r^2-\nu^2\right)R(r)=0 \tag{A.3}$$

for the radial direction. In Eqs. (A.2) and (A.3), ν is the constant of separation.

The normalized solutions of Eq. (A.2) are the oscillatory functions,

$$\Phi_\nu(\phi) = \frac{1}{\sqrt{2\pi}} e^{\pm i\nu\phi}. \tag{A.4}$$

Since $\Phi_\nu(\phi)$ of Eq. (A.4) must be single valued, ν is restricted to integer values. The solutions to Eq. (A.3) which are regular at $r = 0$ are,

$$R_\nu(r) = A\, J_\nu\left(\frac{\sqrt{2mE}}{\hbar} r\right) \tag{A.5}$$

where J_ν is the Bessel function and A is a normalization constant. The Dirichlet boundary condition implies that the radial function $R_\nu(r)$ of Eq. (A.5) must vanish at the circle boundary $r = R$ and this provides the quantization condition,

$$J_\nu\left(\frac{\sqrt{2mE}}{\hbar} R\right) = 0. \tag{A.6}$$

From Eq. (A.6), the exact energy eigenvalues for the circle billiard are,

$$E_{n,\nu} = \frac{\hbar^2}{2m}\left(\frac{\alpha_n^\nu}{R}\right)^2 \tag{A.7}$$

where α_n^ν is the n^{th} zero of the Bessel function J_ν. An analytic expression for the normalization constant A of Eq. (A.5) can be obtained for energies $E = E_{n,\nu}$ and is given by ([1] p.593)

$$A_{n,\nu} = \left(\frac{2}{R^2 J_{\nu+1}^2(\alpha_n^\nu)}\right)^{\frac{1}{2}}. \tag{A.8}$$

Hence, combining Eqs. (A.4), (A.5), and (A.7), the normalized exact energy eigenfunctions for the circle billiard are

$$\psi_{n,\nu}(r,\phi) = \frac{A_{n,\nu}}{\sqrt{2\pi}} J_\nu\left(\alpha_n^\nu \frac{r}{R}\right) e^{\pm i\nu\phi} \tag{A.9}$$

A.2 The 45° Wedge Billiard

The 45° wedge billiard is a two-dimensional system consisting of a particle of mass m subject to a constant force mg and confined to a wedge of half angle ϕ. In quantum mechanics, the motion of this particle is described by the time-independent Schrödinger equation

$$-\frac{\hbar^2}{2m}\left(\frac{\partial^2}{\partial x^2} + \frac{\partial^2}{\partial y^2}\right)\Psi(x,y) + mgy\Psi(x,y) = E\Psi(x,y), \tag{A.10}$$

for $x > 0$ and $y \geq x\cot(\phi)$. The Dirichlet boundary conditions are $\Psi(0,y) = 0$ and $\Psi(x, x\cot(\phi)) = 0$. To obtain the quantum solution to Eq. (A.10), one considers the 90° symmetric wedge described by the same Hamiltonian but with the boundary conditions $\Psi(\pm|x|, |x|\cot(\phi)) = 0$. Introducing the coordinate transformations,

$$X = \frac{x+y}{\sqrt{2}} \qquad \text{and} \qquad Y = \frac{-x+y}{\sqrt{2}}, \tag{A.11}$$

to variables X and Y running parallel to the walls of the 90° symmetric wedge, Eq. (A.10) becomes:

$$-\frac{\hbar^2}{2m}\left(\frac{\partial^2}{\partial X^2}+\frac{\partial^2}{\partial Y^2}\right)\Psi(X,Y)+\frac{mg}{\sqrt{2}}(X+Y)\,\Psi(X,Y)=E\Psi(X,Y), \quad \text{(A.12)}$$

for $X>0$ and $Y>0$. Equation (A.12) separates into two identical one-dimensional equations of the form,

$$\frac{\partial^2}{\partial z^2}\Psi(z)+\frac{2m^2g}{\sqrt{2}\hbar^2}\left(\frac{\sqrt{2}E}{mg}-z\right)\Psi(z)=0, \qquad \text{for } z\geq 0. \quad \text{(A.13)}$$

Changing to the dimensionless variable

$$z'=\left(\frac{2m^2g}{\sqrt{2}\hbar^2}\right)^{\frac{1}{3}}\left(z-\frac{\sqrt{2}E}{mg}\right). \quad \text{(A.14)}$$

Eq. (A.13) becomes:

$$\frac{\partial^2}{\partial z'^2}\Psi(z')-z'\Psi(z')=0. \quad \text{(A.15)}$$

The solution to Eq. (A.15) which does not increase exponentially with z' is the Airy function $Ai(z')$. Therefore,

$$\Psi(z)=C\,Ai\left[\left(\frac{2m^2g}{\sqrt{2}\hbar^2}\right)^{\frac{1}{3}}\left(z-\frac{\sqrt{2}E}{mg}\right)\right]. \quad \text{(A.16)}$$

where C is a normalization constant. The Dirichlet boundary condition implies that the function $\Psi(z)$ of Eq. (A.16) must vanish at the boundary $z=0$ and this provides the quantization condition,

$$Ai\left[\left(\frac{2m^2g}{\sqrt{2}\hbar^2}\right)^{\frac{1}{3}}\left(-\frac{\sqrt{2}E}{mg}\right)\right]=0. \quad \text{(A.17)}$$

From Eq. (A.17), the exact energy eigenvalues are

$$E_{n_1} = -\frac{mga_{n_1}}{\sqrt{2}}\left(\frac{\sqrt{2}\hbar^2}{2m^2g}\right)^{\frac{1}{3}}, \qquad \text{with } n_1 \geq 0, \tag{A.18}$$

where a_{n_1} is the n_1^{th} zero of the Airy function $Ai(z)$. The normalization constant C of Eq. (A.16) for energies $E = E_{n_1}$ is given by [37]

$$C_{n_1} = \left(\frac{2m^2g}{\sqrt{2}\hbar^2}\right)^{\frac{1}{6}} \frac{1}{Ai'(a_{n_1})}. \tag{A.19}$$

The energy eigenvalues for the 90° wedge billiard are given by the sum of the energy eigenvalues for the X and Y equations:

$$E_{n_1,n_2} = E_{n_1} + E_{n_2} = -\frac{(a_{n_1} + a_{n_2})}{\sqrt{2}}\left(\frac{\sqrt{2}\hbar^2}{2m^2g}\right)^{\frac{1}{3}}, \qquad \text{for } n_1, n_2 \geq 0. \tag{A.20}$$

The normalized energy eigenfunctions are given by the symmetric and antisymmetric linear combinations of the primitive wavefunctions:

$$\psi_{n_1,n_2}(X,Y) = \frac{C_{n_1}C_{n_2}}{\sqrt{2}}\left[Ai_{n_1}(X)Ai_{n_2}(Y) \pm Ai_{n_2}(X)Ai_{n_1}(Y)\right]. \tag{A.21}$$

For the 45° wedge billiard, the wavefunction must vanish along the line $X = Y$. Hence, the exact energy eigenfunctions for the 45° wedge billiard are given by the antisymmetric linear combination of Eq. (A.21). Furthermore, from Eq. (A.21), one sees that $\psi_{n_1,n_2}(X,Y)$ is zero when $n_1 = n_2$. The exact energy eigenvalues for the 45° wedge billiard are the same as those of the 90° symmetric wedge billiard with the restriction $n_1 \neq n_2$.

Appendix B

The WKB Approximation

The WBK (Wentzel-Kramers-Brillouin) approximation is a semiclassical me -thod which applies to multidimensional separable Hamiltonian systems. It is an efficient method for calculating approximate solutions to the Schrödinger equation in the limit $\hbar \to 0$ or, equivalently, for highly excited states. In addition, and perhaps more importantly, it establishes a connection between classical and quantum mechanics. In this appendix, the WKB solutions to the circle and 45° wedge billiards are provided. Details of the development of the WKB approximation are not presented here since they can be found in many textbooks on quantum mechanics (Schiff [38]) and in journal articles (Knudson and Noid [26]).

B.1 The general solution

Consider one-dimensional Schrödinger equations of the general form

$$\frac{d^2u(x)}{dx^2} + k^2(x)u(x) = 0, \qquad \text{with } k^2(x) > 0,$$

$$\frac{d^2u(x)}{dx^2} - \kappa^2(x)u(x) = 0, \qquad \text{with } \kappa^2(x) > 0, \tag{B.1}$$

and with,

$$\begin{aligned} k(x) &= +\frac{1}{\hbar}[2m(E - V(x))]^{\frac{1}{2}} \qquad \text{when } V(x) < E, \\ \kappa(x) &= +\frac{1}{\hbar}[2m(V(x) - E)]^{\frac{1}{2}} \qquad \text{when } V(x) > E. \end{aligned} \tag{B.2}$$

The first expression in Eq. (B.2) pertains to the classically allowed region $V(x) < E$ whereas the second formula refers to the classically forbidden region $V(x) > E$. For the cases where Eq. (B.1) cannot be solved explicitly and $V(x)$ is a slowly varying function of the position x, it is possible to obtain approximate solutions, to the order of $\hbar$, given by

$$\begin{aligned} u^{WKB}(x) &= Ak(x)^{-\frac{1}{2}} \exp\left(\pm i \int_{x_o}^{x} k(x)\,dx\right), \qquad \text{when } V(x) < E \\ u^{WKB}(x) &= A\kappa(x)^{-\frac{1}{2}} \exp\left(\pm \int_{x_o}^{x} \kappa(x)\,dx\right), \qquad \text{when } V(x) > E \end{aligned} \tag{B.3}$$

where A is a normalization constant and x_o is usually chosen to be a zero of $k(x)$ or $\kappa(x)$.

The conditions for which the WKB approximation is valid can be determined by substituting Eq. (B.3) into Eq. (B.1) and writing the result as (only shown for the case $V(x) < E$ since the following analysis also applies to the case when $V(x) > E$),

$$\frac{d^2u(x)}{dx^2} + (k^2(x) - w(x))u(x) = 0, \qquad \text{when } V(x) < E \tag{B.4}$$

where

$$w(x) = \frac{3(k'(x))^2}{4k^2(x)} - \frac{k''(x)}{2k(x)}. \tag{B.5}$$

The WKB solutions, Eq. (B.3), are good approximations to the exact solutions $u(x)$ if one of the following conditions is satisfied [4]:

(a) $k^2(x)$ is bounded and nonzero, $w(x)$ is bounded.

(b) $k^2(x)$ diverges, $\hbar^2 w(x)/2mk^2(x)$ is negligible.

(c) $k^2(x)$ is zero (a classical turning point), $w(x) = 0$.

The bound states are obtained by matching the solutions of Eq. (B.3) at the classical turning points, where $E = V(x)$. However, since the WKB approximation breaks down in the vicinity of classical turning points, one must use *connection formulae*. Consider the case when the WKB solution in the classically forbidden region decays as x tends away from x_o (The other possibility, an exponential increase, will not be discussed since it is not required for the derivations presented in this Appendix). At a left-hand barrier, when $V(x) > E$ for $x < x_1$ and $V(x) < E$ for $x > x_1$, the connection formula can be expressed as

$$\kappa(x)^{-\frac{1}{2}} \exp\left[\frac{1}{\hbar}\int_{x_1}^{x} \kappa(x)\,dx\right] \rightarrow 2[k(x)]^{-\frac{1}{2}} \cos\left[\frac{1}{\hbar}\int_{x_1}^{x} k(x)\,dx - \frac{\pi}{4}\right] \tag{B.6}$$

For the right-hand barrier, when $V(x) < E$ for $x < x_2$ and $V(x) > E$ for $x > x_2$, the

connection formula is given by

$$2[k(x)]^{-\frac{1}{2}} \cos\left[-\frac{1}{\hbar}\int_{x_2}^{x} k(x)\,dx - \frac{\pi}{4}\right] \leftarrow \kappa(x)^{-\frac{1}{2}} \exp\left[\frac{1}{\hbar}\int_{x_2}^{x} \kappa(x)\,dx\right]. \tag{B.7}$$

The arrows in Eqs. (B.6) and (B.7) indicate the direction in which the connection can safely be made. Hence, knowing that the WKB solution is exponentially decreasing on the left side of the turning point x_1, the WKB solution sufficiently far to the right of x_1 is a cosine as shown in Eq. (B.6). Similarly, the WKB solution sufficiently far to the left of x_2 is a cosine as shown in Eq. (B.7). By requiring that the solutions inside the classically allowed region must be equal, we obtain the condition

$$2[k(x)]^{-\frac{1}{2}} \cos\left[\frac{1}{\hbar}\int_{x_1}^{x} k(x)\,dx - \frac{\pi}{4}\right] = \pm 2[k(x)]^{-\frac{1}{2}} \cos\left[-\frac{1}{\hbar}\int_{x_2}^{x} k(x)\,dx - \frac{\pi}{4}\right], \tag{B.8}$$

which leads to the Bohr-Sommerfeld quantization condition

$$2\int_{x_1}^{x_2} k(x)\,dx = 2\pi\hbar\left(n + \frac{1}{2}\right), \quad n = 0, 1, 2, \ldots \tag{B.9}$$

Finally, the WKB solution at a rigid wall, $V(x_o) = \infty$, has the asymptotic solution of the form

$$[k(x)]^{-\frac{1}{2}} \sin\left[\frac{1}{\hbar}\int_{x_o}^{x} k(x)\,dx\right]. \tag{B.10}$$

in the classically accessible region.

B.2 The Circle Billiard

The WBK solution for the circle billiard presented here is based on a paper by Berry and Ozorio de Almeida [4] detailing the WKB treatment to two-dimensional Schrödinger equations in cylindrical coordinates. If one wants to solve the Schrödinger equation for a particle in a circle (with constant potential) by the WKB approximation, on first separates variables and has solutions of the form $\psi_\nu(r,\phi) = R_\nu(r)\exp(\pm i\nu\phi)$ for $\nu = 0, 1, 2, \ldots$. The angular part is exact. The WKB approximation is concerned only with the radial part.

By setting $R_\nu(r) = r^{-\frac{1}{2}}u_\nu(r)$ in Eq. (A.3), the radial equation takes one of the forms

$$\begin{aligned} \frac{d^2u_\nu(r)}{dr^2} + k_o^2(r)u_\nu(r) &= 0, \qquad \text{with } k_o^2(r) > 0 \\ \frac{d^2u_\nu(r)}{dr^2} - \kappa_o^2(r)u_\nu(r) &= 0, \qquad \text{with } \kappa_o^2(r) > 0 \end{aligned} \tag{B.11}$$

and with

$$\begin{aligned} k_o^2(r) &= \frac{2mE}{\hbar^2}\left[1 - \frac{\hbar^2\left(\nu^2 - \frac{1}{4}\right)}{2mEr^2}\right], \\ \kappa_o^2(r) &= \frac{2mE}{\hbar^2}\left[\frac{\hbar^2\left(\nu^2 - \frac{1}{4}\right)}{2mEr^2} - 1\right]. \end{aligned} \tag{B.12}$$

For a particular energy E, the first formula in Eq. (B.11) applies when $r^2 > \frac{\hbar^2(\nu^2-1/4)}{2mE}$ and, the second formula pertains to values $r^2 < \frac{\hbar^2(\nu^2-1/4)}{2mE}$.

Since both $k_\nu^2(r)$ and $\kappa_\nu^2(r)$ diverge at the origin $r = 0$, one must consider condition (b) to determine the validity of the WKB approximation at the origin. In this case,

$$\lim_{r\to 0}\frac{w_\nu(r)}{k_\nu^2(r)} = \lim_{r\to 0}\frac{1}{k_\nu^2(r)}\left(\frac{3(k_\nu'(r))^2}{4k_\nu^2(r)} - \frac{k_\nu''(r)}{2k_\nu(r)}\right) \sim \frac{1}{4\nu^2-1}. \tag{B.13}$$

Clearly, from Eq. (B.13), $w_\nu(r)/k_\nu^2(r)$ is not negligible for small values of ν, and consequently the WKB approximation fails at the origin for small values of ν. This result also applies for $\kappa_\nu^2(r)$. This difficulty at the origin can be removed by making a Langer transformation [27] setting $r = e^x$ and $u_\nu(r) = e^{x/2}\psi_\nu(x)$. In this case, Eq. (B.11) becomes

$$\begin{aligned}\frac{d^2\psi_\nu(x)}{dx^2} + q^2(x)\psi_\nu(x) &= 0, \text{ with } q^2(x) > 0\\ \frac{d^2\psi_\nu(x)}{dx^2} - Q^2(x)\psi_\nu(x) &= 0, \text{ with } Q^2(x) > 0\end{aligned} \tag{B.14}$$

where

$$\begin{aligned}q^2(x) &= \frac{2mE}{\hbar^2}\left[e^{2x} - \frac{\hbar^2\nu^2}{2mE}\right]\\ Q^2(x) &= \frac{2mE}{\hbar^2}\left[\frac{\hbar^2\nu^2}{2mE} - e^{2x}\right]\end{aligned} \tag{B.15}$$

The only turning point occurs when $q(x) = 0$ (or $Q(x) = 0$), which happens when $r_o = e^{x_o} = \frac{\hbar\nu}{\sqrt{2mE}}$. The first form in Eq. (B.14) refers to values of $r > r_o$ and the second form is valid for values $r < r_o$. At the origin $r = 0$ (or equivalently $x = -\infty$),

$Q^2(x) = \nu^2$ (and $q^2(x) = -\nu^2$). When $\nu \neq 0$, $Q(x)$ is bounded and not zero. According to condition (a), since

$$\lim_{x\to-\infty} W(x) = \lim_{x\to-\infty} \frac{3(Q'(x))^2}{4Q^2(x)} - \frac{Q''(x)}{2Q(x)} = 0, \tag{B.16}$$

the WKB approximation is suitable at the origin. However, when $\nu = 0$, $Q^2(x) = 0$ and, since $\lim_{x\to-\infty} W(x) = \infty$, the Langer WKB form fails (condition (c)). The failure of the WKB approximation at the origin for $\nu = 0$ is only important when calculating the bound states for $\nu = 0$ and additional measures must be used to deal with this case. However, Berry and Ozorio de Almeida [4] have shown by a careful analysis that, in the end, the quantization condition presented below also applies for the case $\nu = 0$. The Langer form of the WKB approximation (Eqs. (B.14) and (B.15)) is valid for all cases. The WKB solutions for the classically allowed region, based on Eq. (B.3), are given by,

$$\begin{aligned} u_\nu^{WKB}(r) &= Ae^{x/2} v_\nu^{Langer WKB}(x) \\ &= A\frac{e^{x/2}}{(q(x))^{1/2}} \exp\left(\pm i \int^x q(x)\,dx\right) \\ &= A[k_1(r)]^{-\frac{1}{2}} \exp\left(\pm i \int_R^r k_1(r')\,dr'\right), \qquad \text{for } r_o < r < R \end{aligned} \tag{B.17}$$

where A is a constant, R is the radius of the circle,

$$k_1^2(r) = \frac{2mE}{\hbar^2}\left[1 - \frac{\hbar^2\nu^2}{2mEr^2}\right] \tag{B.18}$$

and,

$$\int_R^r k_1(r')\,dr' = \frac{\sqrt{2mE}}{\hbar}\left[\sqrt{r^2-\frac{\hbar^2\nu^2}{2mE}}-\frac{\hbar\nu}{\sqrt{2mE}}\cos^{-1}\left(\frac{\hbar\nu}{\sqrt{2mE}r}\right)\right.$$
$$\left.-\left(\sqrt{R^2-\frac{\hbar^2\nu^2}{2mE}}-\frac{\hbar\nu}{\sqrt{2mE}}\cos^{-1}\left(\frac{\hbar\nu}{\sqrt{2mE}R}\right)\right)\right]. \qquad \text{(B.19)}$$

Since the WKB eigenfunctions for the circle billiard must vanish at the circle boundary $r = R$, the eigenfunctions are constructed from the linear combination of the solutions (B.17) which produces the sine solution of Eq. (B.17),

$$u_\nu^{WKB}(r) = A[k_1(r)]^{-\frac{1}{2}}\sin\left(\int_R^r k_1(r')\,dr'\right) \qquad \text{(B.20)}$$

with the integral given by Eq. (B.19). This is actually the "Langer-type WKB approximation". Similarly, the WKB solutions for the classically forbidden region, based on Eq. (B.3), are

$$u_\nu^{WKB}(r) = [\kappa_1(r)]^{-\frac{1}{2}}\exp\left(\pm\int_{r_o}^r \kappa_1(r)\,dr\right) \qquad \text{for } 0 < r < r_o \qquad \text{(B.21)}$$

where

$$\kappa_1^2(r) = \frac{2mE}{\hbar^2}\left[\frac{\hbar^2\nu^2}{2mEr^2}-1\right] \qquad \text{(B.22)}$$

and,

$$\int_{r_o}^r \kappa_1(r')\,dr' = \frac{\sqrt{2mE}}{\hbar}\left[\sqrt{\frac{\hbar^2\nu^2}{2mE}-r^2}-\frac{\hbar\nu}{\sqrt{2mE}}\ln\left(\frac{\frac{\hbar\nu}{\sqrt{2mE}}+\sqrt{\frac{\hbar^2\nu^2}{2mE}+r^2}}{r}\right)\right]. \qquad \text{(B.23)}$$

In the classically forbidden region, we want the solution to the WBK energy eigenfunctions (Eq. (B.21)) that decays as $r \to 0$. This corresponds to the positive sign in Eq. (B.21).

The WKB bound states for $\nu \neq 0$ are obtained from the connection formulas joining the asymptotic WKB solutions at the turning points. The special treatment required to deal with the case $\nu = 0$ will not be presented here since it is given in detail in the paper by Berry and Ozorio de Almeida [4], and the bound states for $\nu = 0$ have the same form as those for $\nu \neq 0$. At $r_o = \frac{l\omega}{\sqrt{2mE}}$, the appropriate connection formula is

$$k(r)^{-\frac{1}{2}} \cos\left(\int_{r_o}^{r} k(r')\,dr' - \frac{\pi}{4}\right) \tag{B.24}$$

in the classically allowed region. At the hard wall collision at $r = R$, the connection formula has the form

$$k(r)^{-\frac{1}{2}} \sin\left(\int_{R}^{r} k(r')\,dr'\right) \tag{B.25}$$

in the classically allowed region. Since Eqs. (B.24) and (B.25) both describe asymptotic forms in the classically allowed region of motion, they must be equal, and this leads to the quantization condition

$$2\int_{r_o}^{R} k(r)\,dr = 2\pi\left(n + \frac{3}{4}\right) \tag{B.26}$$

The energies $E = E_n^{EBK}$ which satisfy Eq. (B.26) are the approximate energy eigen-

values for the circle billiard. Equation (B.26) applies for all values of ν.

B.3 The 45° Wedge Billiard

The WKB solutions to the 45° wedge billiard derived in this section are also given in Goodings and Szeredi [19], Szeredi [39], and Rouvinez [37]. Similarly to the exact quantum solution (Appendix A), the WKB solution to the 45° wedge billiard is obtained from the solution to the 90° symmetric wedge billiard. As discussed in Appendix A, the Schrödinger equation for the 90° symmetric wedge can be written in terms of the XY-coordinates running parallel to the walls. In this case, it separates into two identical one-dimensional equations (Eq. (A.13)) which takes one of the forms

$$\begin{aligned} \frac{d^2u(x)}{dx^2} + k^2(x)u(x) &= 0, \qquad \text{with } k^2(x) > 0 \\ \frac{d^2u(x)}{dx^2} - \kappa^2(x)u(x) &= 0, \qquad \text{with } \kappa^2(x) > 0 \end{aligned} \tag{B.27}$$

and with

$$\begin{aligned} k^2(x) &= \frac{1}{\hbar}\left[2m\left(E - \frac{mgx}{\sqrt{2}}\right)\right]^{\frac{1}{2}}. \\ \kappa^2(x) &= \frac{1}{\hbar}\left[2m\left(\frac{mgx}{\sqrt{2}} - E\right)\right]^{\frac{1}{2}}. \end{aligned} \tag{B.28}$$

For a particular energy E, the first formula in Eq. (B.27) applies when $x < \frac{\sqrt{2}E}{mg}$ and the second formula pertains to values $x > \frac{\sqrt{2}E}{mg}$. In fact, $x_0 = \frac{\sqrt{2}E}{mg}$ is the only turning

point for this system.

Both $k(x)$ and $\kappa(x)$ are finite and nonzero, and satisfy condition (a) (see Sec. B.1). Hence the WKB solutions for the classically allowed and forbidden regions, based on Eq. (B.3), are given by,

$$\begin{aligned} u^{WKB}(x) &= A[k(x)]^{-\frac{1}{2}} \exp\left(\pm i \int_0^x k(x')\,dx'\right), \qquad \text{for } 0 < x < x_0 \\ u^{WKB}(x) &= A[\kappa(x)]^{-\frac{1}{2}} \exp\left(\pm \int_{x_0}^x \kappa(x')\,dx'\right), \qquad \text{for } x_0 < x < \infty \end{aligned} \tag{B.29}$$

where A is a constant, and

$$\begin{aligned} \int_0^x k(x')\,dx' &= \frac{4}{3m^{1/2}g\hbar}\left[E^{3/2} - \left(E - \frac{mgx}{\sqrt{2}}\right)^{3/2}\right] \\ \int_{x_0}^x \kappa(x')\,dx' &= \frac{4}{3m^{1/2}g\hbar}\left[\left(\frac{mgx}{\sqrt{2}} - E\right)^{3/2}\right] \end{aligned} \tag{B.30}$$

Since, in the classically allowed region, the WKB eigenfunctions must vanish at $x = 0$, the eigenfunctions are constructed from the linear combination of the solutions (B.29) which produces the sine solution of Eq. (B.29),

$$u^{WKB}(x) = A[k(x)]^{-\frac{1}{2}} \sin\left(\int_0^x k(x')\,dx'\right) \tag{B.31}$$

with the integral given by Eq. (B.30). In the classically forbidden region, the WKB eigenfunctions must vanish at $x = \infty$ and therefore, are given by the solution of Eq. (B.29) involving the exponential decay.

The WKB bound states are obtained from the connection formulas joining

the asymptotic WKB solutions at the turning points. At $x_0 = \frac{\sqrt{2}E}{mg}$, the appropriate connection formula is

$$k(x)^{-\frac{1}{2}} \cos\left(\int_{x_0}^{x} k(x')\,dx' - \frac{\pi}{4}\right) \tag{B.32}$$

in the classically allowed region. At the hard wall collision at $x = 0$, the connection formula has the form

$$k(x)^{-\frac{1}{2}} \sin\left(\int_{0}^{x} k(x')\,dx'\right) \tag{B.33}$$

in the classically allowed region. Since Eqs. (B.32) and (B.33) both describe asymptotic forms in the classically allowed region of motion, they must be equal, and this leads to the quantization condition

$$2\int_{0}^{x_0} k(x')\,dx' = 2\pi\left(n + \frac{3}{4}\right). \tag{B.34}$$

Using Eq. (B.30), the WKB energy eigenvalues E_n^{EBK} which satisfy Eq. (B.34) are

$$E_n^{WKB} = \left[\frac{3m^{1/2}g\pi\hbar}{4}(n + 3/4)\right]^{2/3}, \qquad \text{with } n \geq 0. \tag{B.35}$$

As discussed in Appendix A, the energy eigenvalues for the 45° symmetric wedge are given by the sum of the energy eigenvalues for the X and Y equations:

$$E_{n_1,n_2}^{EBK} = E_{n_1}^{EBK} + E_{n_2}^{EBK} = \left[\frac{3m^{1/2}g\pi\hbar}{4}(n_1 + 3/4)\right]^{\frac{2}{3}} + \left[\frac{3m^{1/2}g\pi\hbar}{4}(n_2 + 3/4)\right]^{\frac{2}{3}} \tag{B.36}$$

with the restriction $n_1 \neq n_2$. The energy eigenfunctions are given by the antisymmetric linear combination of the primitive eigenfunctions given by Eqs. (B.29) and

(B.30):

$$\psi^{EBK}_{n_1,n_2}(X,Y) = C[u^{WKB}_{n_1}(X)u^{WKB}_{n_2}(Y) - u^{WKB}_{n_2}(X)u^{WKB}_{n_1}(Y)]. \tag{B.37}$$

Appendix C

Classical Actions and Related Phase Indices

C.1 The Circle Billiard

The classical Hamiltonian for the circle billiard (described in Appendix A) is most conveniently written in terms of cylindrical coordinates as

$$H = \frac{p_r^2}{2m} + \frac{p_\theta^2}{2mr^2} = E. \tag{C.1}$$

Since this Hamiltonian is cyclic in the angular coordinate θ, the angular momentum p_θ is a constant of motion. Thus, the classical action in the angular direction is also a constant of motion given by

$$I_\theta = \oint p_\theta \, \mathrm{d}\theta = 2\pi p_\theta. \tag{C.2}$$

Since there are no turning points, hard-wall collisions or caustics for a trajectory along the angular direction, the Maslov index for I_θ is $\nu_\theta = 0$.

The radial momentum p_r can be written in terms of its canonical variable r

by solving for p_r in Eq. (C.1). The result is

$$\begin{aligned} p_r &= \pm p_r(E,r) \\ &= \pm\sqrt{2mE - \frac{p_\theta^2}{r^2}}. \end{aligned} \tag{C.3}$$

Consider a classical trajectory which starts at a point r_0 with a negative radial momentum $-p_r(E,r_0)$. In this case, the particle is moving away from the inner circular region and heading towards the circle boundary at $r = R$. The particle then makes a hard-wall collision with the circle boundary and is directed back towards the inner circular region. At the minimum distance from the origin r_{min}, the radial momentum is $p_r(E,r_{min}) = 0$. By setting $p_r = 0$ in Eq. (C.1), $r_{min} = \frac{p_\theta}{\sqrt{2mE}}$. A complete cycle ends when the particle returns to r_0 with momentum $-p_r(E,r_0)$. The radial classical action becomes

$$\begin{aligned} I_r &= \oint p_r\,\mathrm{d}r \\ &= \int_{r_0}^{R} p_r(E,r)\,\mathrm{d}r + \int_{R}^{r_{min}} -p_r(E,r)\,\mathrm{d}r + \int_{r_{min}}^{r_0} p_r(E,r)\,\mathrm{d}r \\ &= 2\sqrt{2mE}\left[\sqrt{R^2 - \frac{p_\theta^2}{2mE}} - \frac{p_\theta}{\sqrt{2mE}}\cos^{-1}\left(\frac{p_\theta}{\sqrt{2mE}R}\right)\right]. \end{aligned} \tag{C.4}$$

For one cycle of the radial component, the related phase index is $\nu_r = 3$, obtained by counting 2 for the momentum reversing collision at $r = R$ plus 1 for the turning point at $r = r_{min}$.

C.2 The 90° Symmetric Wedge Billiard

The classical Hamiltonian for the 90° symmetric wedge (decribed in Appendix A) expressed in terms of the canonical variables parallel to the sides of the wedge is given by

$$H = \frac{p_X^2}{2m} + \frac{mgX}{\sqrt{2}} + \frac{p_{Y'}^2}{2m} + \frac{mgY'}{\sqrt{2}} = E \tag{C.5}$$

where $X \geq 0$ and $Y' \geq 0$. This Hamiltonian separates into two identical one-dimensional Hamiltonian systems,

$$\begin{aligned} H_X &= \frac{p_X^2}{2m} + \frac{mgX}{\sqrt{2}} = E_X \\ H_{Y'} &= \frac{p_{Y'}^2}{2m} + \frac{mgY'}{\sqrt{2}} = E_{Y'} \end{aligned} \tag{C.6}$$

with $E = E_X + E_{Y'}$. Hence, the following results obtained for the variable Y' apply to the variable X.

Solving for $p_{Y'}$ in Eq. (C.6) leads to expression,

$$\begin{aligned} p_{Y'} &= \pm p_{Y'}(E_{Y'}, Y') \\ &= \pm\sqrt{2m\left(E_{Y'} - \frac{mgY'}{\sqrt{2}}\right)}. \end{aligned} \tag{C.7}$$

With an arbitrary starting point Y_0' and an initial momentum $+p_{Y'}(E_{Y'}, Y_0')$, the particle moves away from the origin and reaches a maximum height $Y_{max}' = \sqrt{2}E_{Y'}/(mg)$ at the turning point when $p_{Y'} = 0$. The momentum then changes sign and the particle

falls back to towards the origin where it makes a hard-wall collision with the billiard boundary. Finally, the particle returns to its initial state $(Y_o, +p_Y(E_Y, Y_o))$. The classical action for the motion along the Y- direction becomes

$$\begin{aligned} I_Y &= \oint p_Y \mathrm{d}Y \\ &= \int_{Y_o}^{Y_{max}} p_Y(E_Y, Y)\mathrm{d}Y + \int_{Y_{max}}^{0} -p_Y(E_Y, Y)\mathrm{d}Y + \int_{0}^{Y_o} p_Y(E_Y, Y)\mathrm{d}Y \\ &= \frac{8}{3m^{\frac{1}{2}}g} E_Y^{3/2} \end{aligned} \tag{C.8}$$

The Maslov index for this circuit is $\nu_Y = 3$ which includes the contribution of 2 for the hard-wall collision at $Y = 0$ and 1 for the turning point at $Y_{max} = \sqrt{2}E_Y/(mg)$.

Appendix D

The Normal Derivative in Two Dimensions

Our goal is to derive a general expression for a partial derivative with respect to the coordinate perpendicular to a classical trajectory in a two-dimensional cartesian plane. We begin by considering an arbitrary trajectory described by cartesian coordinates (x, y) as shown in Fig. D.1. A second coordinate system has been drawn with its origin at the point $\vec{x}_1 = (x_1, y_1)$ along the trajectory such that the x'' and y'' coordinates are perpendicular and parallel to the trajectory, respectively. The momentum vector $\vec{p}(\vec{x}_1)$, which is tangent to the trajectory, is directed along the positive y''-axis.

The $x''y''$-coordinates are related to the xy-coordinates by simple coordinate transformations. First, the origin of the xy-coordinate system is translated to the point $\vec{x}_1 = (x_1, y_1)$ and consequently, is described by the new coordinates

$$x' = x - x_1 \qquad \text{and} \qquad y' = y - y_1. \tag{D.1}$$

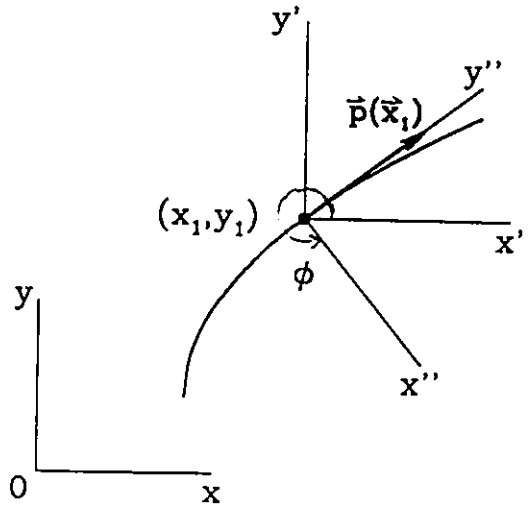

Figure D.1: Orientations of the coordinate systems with respect to an arbitrary trajectory.

Then, the $x'y'$-axes are rotated counterclockwise, by the angle ϕ, until they coincide with the $x''y''$-axes. This rotation is described by

$$\begin{aligned} x'' &= x' \cos\phi + y' \sin\phi \\ y'' &= -x' \sin\phi + y' \cos\phi \end{aligned} \tag{D.2}$$

Solving for x' and y', Eq. (D.2) becomes:

$$\begin{aligned} x' &= x'' \cos\phi - y'' \sin\phi \\ y' &= x'' \sin\phi + y'' \cos\phi \end{aligned} \tag{D.3}$$

Substituting for x' and y' in Eq. (D.3) using Eq. (D.1), one obtains the desired relations

$$x = x'' \cos\phi - y'' \sin\phi + x_1 \qquad \text{and} \qquad y = x'' \sin\phi + y'' \cos\phi + y_1 \tag{D.4}$$

The partial derivative with respect to the x''-coordinate (perpendicular to the trajectory) is related to the partial derivatives with respect to the original coordinates x and y using the standard product rule for partial differentiation. The result is

$$\begin{aligned} \frac{\partial}{\partial x''} &= \frac{\partial x}{\partial x''}\frac{\partial}{\partial x} + \frac{\partial y}{\partial x''}\frac{\partial}{\partial y} \\ &= \cos\phi \frac{\partial}{\partial x} + \sin\phi \frac{\partial}{\partial y} \end{aligned} \tag{D.5}$$

It is often more convenient to express Eq. (D.5) in terms of the direction angle α of the momentum vector $\vec{p}(\vec{x}_1)$ with respect to the x-axis. Since the momentum $\vec{p}(\vec{x}_1)$ has been aligned with the positive y''-axis (Fig. D.1), $\alpha = \phi + \pi/2$. Hence, Eq. (D.5) becomes

$$\begin{aligned} \frac{\partial}{\partial x''} &= \sin\alpha \frac{\partial}{\partial x} - \cos\alpha \frac{\partial}{\partial y} \\ &= \frac{1}{|\vec{p}(\vec{x}_1)|}\left(p_{y_1}\frac{\partial}{\partial x} - p_{x_1}\frac{\partial}{\partial y}\right). \end{aligned} \tag{D.6}$$

Eqs. (D.5) and (D.6) are two forms for the partial derivative with respect to the coordinate perpendicular to the classical trajectory at the point $\vec{x}_1 = (x_1, y_1)$.